TRƯỜNG ĐẠI HỌC QUY NHƠN
QUY NHON UNIVERSITY

TẠP CHÍ KHOA HỌC
TRƯỜNG ĐẠI HỌC QUY NHƠN

QUY NHON UNIVERSITY
JOURNAL OF SCIENCE

CHUYÊN SAN KHOA HỌC TỰ NHIÊN VÀ KỸ THUẬT
ISSUE: NATURAL SCIENCES AND ENGINEERING

16 (5)
2022

OCTOBER 2022

QUY NHON UNIVERSITY
JOURNAL OF SCIENCE VOLUME 16, NUMBER 5, OCTOBER 2022
ISSN : 1859-0357

CONTENTS

https://doi.org/10.52111/qnjs.2022.16501

TẠP CHÍ KHOA HỌC
TRƯỜNG ĐẠI HỌC QUY NHƠN

Quá trình điện cực bằng dòng một chiều (DC) cao áp với plasma điện hóa và các ứng dụng công nghệ

Nguyễn Đức Hùng[1,2,*]

[1]Viện Công nghệ Môi trường, Viện Hàn lâm Khoa học và Công nghệ Việt Nam, Việt Nam
[2]Viện Công nghệ Đổi mới và Đào tạo Quốc tế, Việt Nam

Ngày nhận bài: 20/01/2022; Ngày nhận đăng: 12/04/2022; Ngày xuất bản: 28/10/2022

TÓM TẮT

Với điện áp cao một chiều, các phản ứng điện hóa vẫn có thể được thực hiện ngay cả trong nước cất có độ dẫn điện rất thấp. Ion kim loại từ phản ứng hòa tan ở anot có thể phản ứng với khí hiđro được tạo thành từ catot trong môi trường nước để tạo thành kim loại; rồi nguyên tử kim loại tương tác tiếp tục bằng lực Van der Walls để tạo nên các hạt nano kim loại. Các quá trình phản ứng trên các điện cực để chế tạo dung dịch nano kim loại được kiểm soát bằng điện áp cao một chiều, khoảng cách giữa các điện cực anot với catot và độ dẫn của môi trường. Các đặc tính của dung dịch nano bạc kim loại như phổ UV-Vis, hình dạng hạt TEM, phân bố kích thước hạt, thế zeta cũng như khả năng diệt khuẩn đã được xác định và chứng minh. Sản phẩm thu được có độ tinh khiết cao do dung dịch nano không chứa các ion Na^+, NO_3^- cũng như các sản phẩm phản ứng và chất ổn định khác nên có thể ứng dụng cho nhiều đối tượng mà không ảnh hưởng đến sức khỏe con người. Ngoài bạc, các kim loại khác như Au, Cu, Fe,... cũng có thể được chế tạo ở dạng nano bằng công nghệ DC cao áp.

Môi trường khí được tạo ra trên điện cực bằng phản ứng điện hóa cao áp một chiều với điện trường lớn và hiệu điện thế cao cũng như tác dụng đốt nóng của môi chất sẽ là điều kiện thích hợp để chuyển từ trạng thái khí sang trạng thái plasma. Dấu hiệu cho thấy sự hiện diện của plasma điện hóa là sự phát sáng trên điện cực cũng như cường độ dòng điện tăng đột biến theo thời gian. Cũng có thể điều khiển thời gian xuất hiện plasma điện hóa khi thay đổi các thông số công nghệ phản ứng điện hóa cao áp. Trạng thái plasma điện hóa sẽ tạo ra H_2O_2 và các gốc tự do như OH• có khả năng phản ứng mạnh. Điều đó được sử dụng để xử lý các chất gây ô nhiễm nước như 2,4-D hoặc 2,4,5-T thành sản phẩm cuối cùng là CO_2 rất hiệu quả, đặc biệt trên điện cực Fe thêm phản ứng Fenton. Tương tự, nước thải dệt nhuộm có xanh metylen cũng như nước thải sinh hóa bệnh viện có nồng độ cao cũng có thể được xử lý cho kết quả tốt bằng DC cao áp với plasma điện hóa.

Từ khóa: *Dòng điện một chiều DC cao áp, nano kim loại, plasma điện hóa, gốc tự do, xử lý ô nhiễm.*

*****Tác giả liên hệ chính.*
Email: nguyenduchung1946@gmail.com

QUY NHON UNIVERSITY
JOURNAL OF SCIENCE

Electrode processes by DC high-voltage - electrochemical plasma and technological applications

Nguyen Duc Hung[1,2,*]

[1]*Institute of Environmental Technology, Vietnam Academy of Science and Technology, Vietnam*
[2]*Institute of Innovation Technology and International Training, Vietnam*

Received: 20/01/2022; Accepted: 12/04/2022; Published: 28/10/2022

ABSTRACT

With high DC voltage, electrochemical reactions can still be carried out even in distilled water with very low conductivity. Metal ions from the dissolution reaction at the anode can react with formed hydrogen gas from the cathode in aqueous medium to form metal and then interact for metal nanoparticles. The reaction processes on the electrodes to make metal nanoparticle solutions are controlled by high DC voltage, distance between anode and cathode electrodes and conductivity of the medium. The properties of metallic silver nanosolutions such as UV-Vis spectrum, TEM particle shape, particle size distribution, zeta potential as well as bactericidal ability have been determined and demonstrated. The obtained product has high purity because the nano solution does not contain Na^+, NO_3^- ions as well as other reaction products and stabilizers, so it can be applied to many objects without affecting human health. In addition to silver, other metals such as Au, Cu, Fe, Al, etc. can also be fabricated in nano form by DC high-voltage technology.

The gaseous environment created on the electrode by a DC high-voltage electrochemical reaction with a large electric field and high potential difference as well as the heating effect of the medium will be the right conditions to switch from the gaseous state to the plasma state. Indications of the presence of electrochemical plasma are the glow on the electrode as well as the amperage that spikes with time. It is also possible to control the electrochemical plasma appearance time when changing the DC high-voltage electrochemical reaction technology parameters. The electrochemical plasma state will generate H_2O_2 and free radicals such as $OH^{\bullet}$ which are highly reactive. That is used to treat water contaminants like 2,4-D or 2,4,5-T into the final product CO_2 very efficiently, especially on Fe electrode adding Fenton reaction. Similarly, methylene blue textile dyeing wastewater as well as high concentration hospital biochemical wastewater can also be treated with good results by high pressure DC with electrochemical plasma.

Keywords: *DC high voltage, metallic nanoparticle, electrochemical plasma, free radicals, water pollution treatment.*

1. INTRODUCTION

Unlike normal electrochemical reactions that occur in electrolyte with low DC voltage, electrodic processes by DC high voltage can also occur in media that are not considered electrolytes like double distilled water.[1-3] For non-conductive media, high voltage is used to heat the medium as a resistor but also potential enough to carry out electrochemical processes on the contact surface between the electrode and the aqueous medium.[4,5] At the positive electrode, the anodic reaction will be the process of dissolving

**Corresponding author.*
Email: nguyenduchung1946@gmail.com

https://doi.org/10.52111/qnjs.2022.16501

the metal of the electrode into ions, but with the inert electrode, oxygen will be released from the water and dispersed into the environment. At the same time, on the negative electrode, the cathode reaction of the water electrolysis process will form hydrogen gas and disperse into the water environment.[6-8] These electrochemical processes also obey Faraday's law. Ions formed from electrochemical processes such as Me^{n+}, H^+, or OH^- will increase the conductivity of the aqueous medium.[1,9] However, because the amount of ions formed is not much, the conductivity increases only slightly with the reaction time. Moreover, in the aqueous environment, substances formed by electrode processes can meet and occur neutralization reactions or redox reactions such as $H^+ + OH^- \rightarrow H_2O$ (1) and $Me^{n+} + n/2H_2 \rightarrow Me^0 + nH^+$ (2). The redox reaction between the metal ion generated from the anode process and the nascent hydrogen gas released from the cathode to form a metal with no valence is the basis for the fabrication of metal nano-sized particles: $nMe^0 \rightarrow$ MeNPs (3).[10-13]

On the other hand, gases are formed on the electrodes by an electrochemical reaction according to Faraday's law under conditions of continued energy supply due to high voltage, strong electric field and gradually increasing solution temperature according to Joul-Lenz's law will facilitate the appearance of a fourth state, the plasma state.[14,15] With the appearance of plasma state on the electrodes the water dissociation to produce H_2 and O_2 gas on the anode: $4H_2O \rightarrow 3H_2+O_2+H_2O_2$ (4) and on the catode: $2H_2O \rightarrow 2H_2 + O_2$ (5) that will become intense and the amount of gas produced will no longer be calculated according to Faraday's law.[16,17] In the plasma state, the following ionization processes will also occur at the electrodes: $H_2O + e^- \rightarrow H^\bullet + OH^\bullet + e^-$ (6); $OH + OH^\bullet \rightarrow H_2O_2$ (7); $2H_2O \rightarrow H_2O_2 + H_2$ (8); $H_2O_2 + h\nu \rightarrow 2OH^\bullet$ (9); $H_2O \rightarrow H + OH^\bullet$ (10).[18-21] Compounds and ions formed from plasma reactions will dissolve and disperse into the aqueous medium, increasing the redox reaction ability for the environment. This is used to treat contaminants present in the aquatic environment. The method of treating water pollution by plasma technology has many advantages such as not using chemicals, only using electricity, thus not causing secondary pollution, low cost, simple equipment and high efficiency because plasma generates very reactive radicals to be able to completely mineralize pollutants.

2. EXPERIMENTAL METHODS

The equipment required to carry out the high-voltage electrochemical reaction as well as the electrochemical plasma generation is a high-voltage DC power source.[22,23] Voltage values are steplessly controlled from 0 to 20 kV with voltage stabilizer and 15 kVA capacity (Figure 1a,b). Values of voltage (kV), current (mA), charge (mAh) and reaction time are shown at control box (1b). The electrochemical reaction vessel is made of heat-resistant glass in the form of a 2-layer tube, the inner tube contains the reaction medium and the outer layer contains cooling water (Figures 1c2, c3). The anode is mounted at the top end (c4) and the cathode (c5) is watertight with the bottom end of the reactor upright. The gas generated from the reaction is collected through valve (c6) and the liquid product is collected through valve (c7).

The evolution of the electrochemical reactions on the electrodes and in the solution such as the formation of bubbles of gas or glow of plasma and color change of liquid were recorded by video. The gaseous high-pressure electrochemical reaction products were collected through valve c6 and determined for volume or qualitatively or quantitatively analyzed using the respective apparatus.

The products of the high-voltage electrochemical reaction dispersed in solution will be characterized or analyzed qualitatively and quantitatively by the respective methods. The loss of anode mass (Δm) due to dissolution by a high voltage direct current electrochemical reaction can be calculated by the gravimetric

method according to the formula: $c_{\Delta m} = \Delta m/V$ (mg/L) or by Faraday's law when determination of the charge (*It*) the reaction can be determined according to the formula: $c_{Far.} = kIt/V$ (mg/L). The conductivity and pH variation of the solution were determined using a Conductivity meter HI 8733 and pH meter HI 8314 from Hanna Instrument.

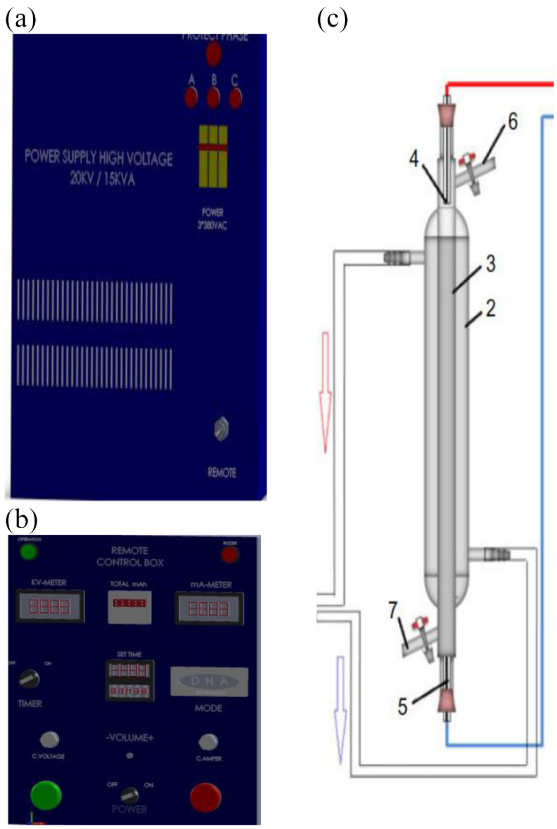

Figure 1. (a) High-voltage rectifiers, (b) Control box, (c) Double layer glass electrochemical reaction vessel. 1. Power supply, 2. Cooling water layer, 3. Reaction medium, 4. Anode, 5 Cathode, 6. Gas escape valve, 7. Reaction product recovery valve.

For products dispersed in solution as nanoparticles, it is possible to characterize UV-Vis spectra on the Hitachi UH-5300 device, the particle size distribution as well as the zeta potential on the SZ-100 device, Horiba, Japan.

For chemical compounds dispersed in solution, gas chromatography-mass spectrometry methods are usually used on the Agilent GC-MS 6890-5975 instrument or atomic mass spectrometry on the ICP-MS 7800/7850 Agilent instrument.

With free radicals such as $OH^{\bullet}$ or H_2O_2 formed from the plasma reaction and dispersed into the solution, it is determined through the corresponding color complexes with salicylic acid according to the reaction such as: (acid salycylic) $(HO)C_6H_4COOH + OH^{\bullet} \rightarrow (HO)_2C_6H_3COOH + H^+$ (11) (acid 2,3-dihydroxybenzoic or 2,5-dihydroxybenzoic) and with titanyl according to the following reaction: $Ti^{4+} + H_2O_2 + 2H_2O \rightarrow TiO_2H_2O_2 + 4H^+$ (12) through a suitable UV-Vis spectrum with corresponding quantification curves.

When using high-voltage electrochemical reactions as well as electrochemical plasma to treat environmental pollutants, chemical oxygen demand (COD) methods according to SMEWW 5220C:2017 and determine total organic carbon (TOC) according to TCVN 6634:2000.

Technological factors affecting electrode response as well as electrochemical plasma formation were investigated such as: distance between anode and cathode electrodes, high voltage, conductivity and initial temperature of the medium, the nature of the electrode metals as well as the concentration and nature of the substances dissolved in the aqueous medium. The metals used as electrodes can be Ag, Cu, Fe depending on the purpose of use to prepare metal nano-solutions or to treat contaminated water chemical pollution.

3. ELECTRODE PROCESSES AT DC HIGH VOLTAGE AND APPLICATION FOR METAL NANOFABRICATION

The anodic electrochemical reaction to dissolve the metal of the electrode material has created oxidizing substances in the aqueous medium in the form of metal ions: $Me \rightarrow Me^{n+} + ne^-$ (13).

The metals that have been tested for anodic dissolution by DC high voltage are Ag, Cu, and Fe. Figure 2 shows that the Ag and Cu anots are dissolved after the reaction (Figure 2a) and the gas is released simultaneously on the cathode (Figure 2b).

https://doi.org/10.52111/qnjs.2022.16501

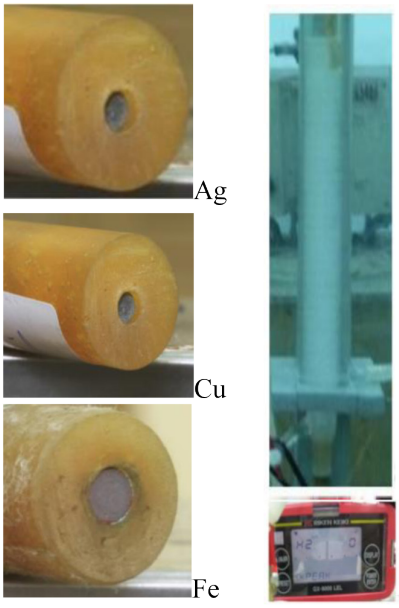

(a) (b)

Figure 2. (a) The anodes of Ag, Cu, Fe are dissolved due to the DC high voltage electrochemical reaction and (b) The H_2 gas released on the cathode simultaneously with the metal dissolution at the anode is determined by the instrument corresponding.

Table 1 presents the concentrations calculated by determining the weight loss of the dissolved anode during the electrochemical reaction in distilled water at different voltage conditions and distances of the cathode and anode.[6,9,10]

Table 1. Metal concentration values calculated by gravimetric method of Ag, Cu, Fe anode materials at electrochemical reaction conditions such as high voltage, electrode distance and reaction time different.

Anode	UDC, kV	DAC, mm	cMe, mg/L
Ag	16	350	700
	15	650	194
	14	1000	104
Cu	16	425	1.82
	16	470	1.90
	16	550	3.21
Fe	16	605	4.87
	15	515	4.50
	14	425	3.96

From Table 1, it can be seen that the amount of metal dissolved by the anode depends not only on the high voltage and time, but also on the distance between the anode and the cathode. When voltage (U_{DC}) is applied to an electrochemical system consisting of two electrodes and an electrolyte medium, the value of electrical energy is distributed to the electrode reactions (E_A, E_C) and ion transport in the medium ($IR_{Elec.}$) according to the equation: $U_{DC} = E_A + IR_{Elec.} + E_C$. Thus, at the value of voltage (U_{DC}), electrochemical reactions occur in time (t) and with current (I), as well as the temperature change (ΔT) of the reaction medium and the cooling water is determined, it will be calculated energy distribution for electrode reaction processes with DC high voltage according to the formula: $H_{DC} = H_E + H_W + H_V$, where $H_{DC} = UIt$ (Wh) is the energy supplied from the power source; H_E is the energy to carry out the electrode reaction; $H_W = mC.\Delta T$ (Wh) is the heating energy of the reaction medium and cooling water and $H_V = m_V\lambda$ is the water evaporation energy which is assumed to be zero at temperatures lower than 100°C.

Table 2 presents the results of determining the energy distribution for the DC high-voltage electrochemical reaction of silver electrodes in distilled water at different electrode distances (D_{A-C}), times (t) and temperatures (T).

Table 2. Value and ratio of energy distribution for high voltage DC electrochemical reaction of silver electrode in distilled water at different electrode distances, time and temperature.

		H_{DC}	H_W		H_E	
		Wh	Wh	%	Wh	%
D_{A-C}	500 mm	615.4	608.9	98.94	6.5	1.06
	750 mm	761.3	688.2	87.67	96.8	12.33
	1000 mm	1044.7	860.6	82.38	184.1	17.62
t	15 min	424.1	350.7	82.69	73.4	17,31
	50 min	718.0	693.9	96.64	24.1	3.36
	80 min	866.8	823.4	94.99	43.4	5.01
T	288 K (15°C)	408.2	350.8	85.94	57.4	14.06
	318 K (20°C)	348.7	332.6	95.38	16.1	4.62
	328 K (55°C)	336.4	332.6	98.87	3.8	1.13

https://doi.org/10.52111/qnjs.2022.16501

From the results of Table 2, it can be seen that the proportion of electrical energy distributed to the electrochemical reaction at the electrodes is smaller than the energy converted to heat.[4] The highest percentage accounts for nearly a quarter of the total energy supplied and fluctuates depending on reaction conditions such as voltage, electrode distance, ambient temperature as well as reaction time. However, it indicates the possiblity of controlling the rate of electrochemical reactions at high voltage by reaction technology parameters. Thus, the electrochemical reactions on the anode dissolve the metal into ions and generate hydrogen gas on the cathode to form a reducing agent that is dispersed into the aqueous medium. In the heart of the aqueous environment, an oxidation-reduction reaction between metal ions and hydrogen gas will occur to form metal atoms and at the same time create metal nanoparticles through the Van de Wall interaction according to the equations: $Me^{n+} + nH_2 \rightarrow Me^0 + 2nH^+$ (14); $xMe^0 \rightarrow MeNPs$ (15).[29]

Figure 3 shows a video image of the color change process of the solution over time from colorless (Figures 3a, b) to (Figures 3c, d) brown and dark brown (Figure 3e) due to the reaction to form metal nanoparticles.

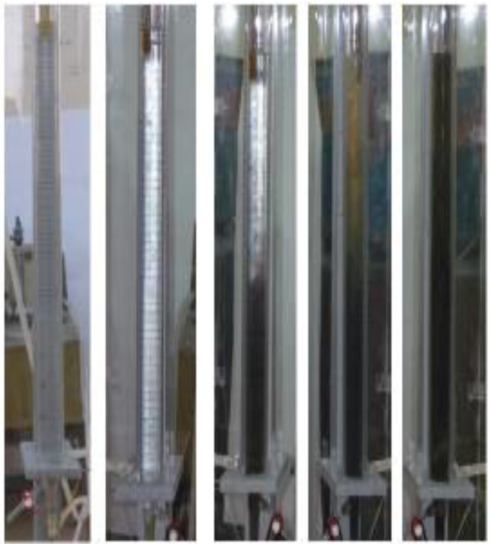

(a) (b) (c) (d) (e)

Figure 3. Color change of aqueous medium at high voltage electrochemical reaction times of Ag electrode from (a) 0 min to (b) 5 min, (c) 10 min, (d) 20 min and (e) 30 min.

The process of forming metal nanoparticle occurs from the cathode region and spreads upward to the anode region. The process occurs not only for metallic silver but also for other metals such as copper, iron, gold and aluminum. Of course, the color of the solution depends on the concentration and nature of the metal in which the high-voltage electrochemical reaction is performed.

The basic properties of metallic silver nanoparticles prepared by high-voltage electrochemical methods similar to other methods such as chemical, physical or biological reduction are the UV-Vis spectral region (Figure 4a), shape (Figure 4b) and particle size distribution (Figure 4c) as well as the ability to kill various bacteria (Figure 4d, e, f).[12] Because the reaction to create silver nanoparticles by H_2 gas generated on the cathode dispersed into the solution meets silver ions due to the dissolved anode, the higher the water temperature increases, the faster the gas escapes from the solution, so the concentration of silver nanoparticles is obtained smaller, and the lower the UV-Vis spectral peak (Figure 4a).

The distinctive feature of metal nanoparticles prepared by DC high-voltage electrochemical method and other methods of $AgNO_3$ salt reduction is that only AgNPS products are obtained without other ions such as Na^+, NO_3, products of reducing agents as well as stabilizers. Therefore, the conductivity of the metal nanoparticle solution prepared by DC high-voltage electrochemical method is very small compared to that of the product prepared by the method from $AgNO_3$ salt.[5,13,15]

https://doi.org/10.52111/qnjs.2022.16501

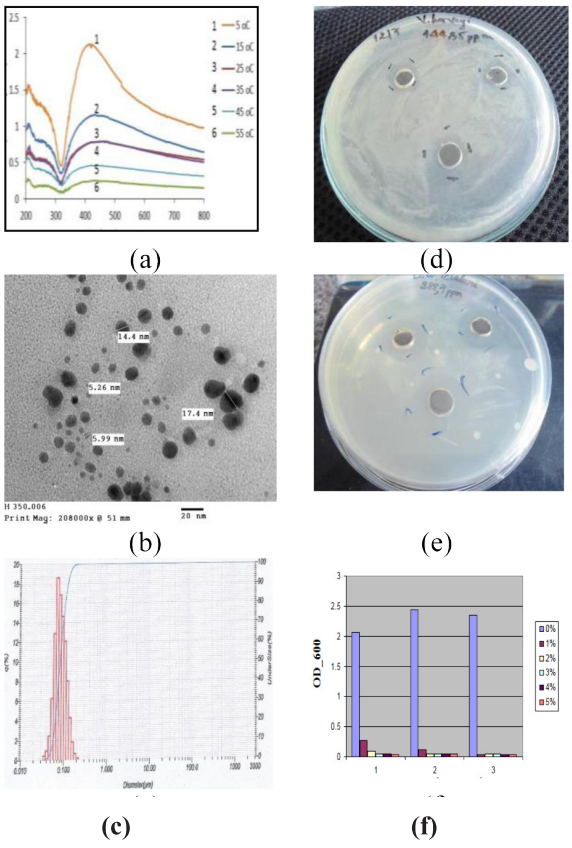

Figure 4. Basic properties of nanosilver solution prepared by DC high voltage method; (a) UV-Vis spectrum, (b) Nanoparticle shape, (c) Nanoparticle size distribution, (d) Antibacterial ring of *Vibrio harveyi*, (e) Antibacterial ring of *Edwardsiella ictaluri*, (f) Bactericidal performance of *E. Coli*.

Another feature of the metal nano-solutions prepared by DC high-voltage is that no stabilizer is needed, but the determined zeta potential value is still greater than 40 mV and has a different sign from the nano-solutions prepared from the reduction process of salt (Figure 5).

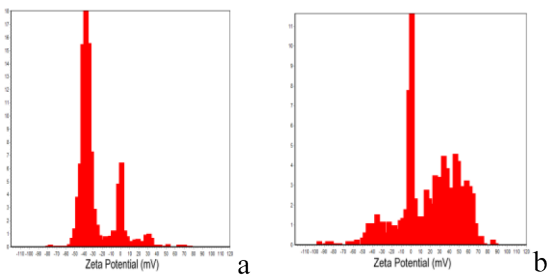

Figure 5. Comparison of zeta potential distribution of colloidal silver solution prepared by DC high-voltage electrochemical method (5a) with chemical reduction method from $AgNO_3$ salt.

From Figure 5, it can be seen that the colloidal solution of nano silver solution prepared by chemical method is a colloidal system with many distributions because in the solution there are many ions such as Na^+, NO_3^-, products of reducing agents and stabilizers determined. Therefore, the outstanding advantage of metallic silver nano-solutions prepared by DC high-voltage method is the purity of only metal nanoparticles without other ions as well as stabilizers. That could eliminate the effect of foreign substances in the solution, such as NO_3^- when applied specifically to areas related to human health.[30-32]

Similar to silver nano, nano-metals of other metals such as copper, iron, gold, aluminum, etc. have also been prepared by high-voltage DC current, but have not been tested as much as AgNPs.[3,6,8,10,33]

4. ELECTROCHEMICAL PLASMA FORMATION AND APPLICATION TO ENVIRONMENTAL POLLUTION TREAMENT OF WASTE WATER

As mentioned above, the electrochemical reaction by high voltage DC current still occurs in non-conductive distilled water and produces hydrogen gas on the cathode and dissolved metal or oxygen on the anode. The gaseous state on the electrodes with high voltage, strong electric field and suitable increase in ambient temperature due to the conversion of electrical energy into heat will convert to the plasma state.[14,28,34,35] A sign of the transition to the plasma state at the electrodes is the observed appearance of glow on the electrodes (Figure 6a). A sign of the simultaneous appearance of the plasma state is the electrochemical reaction rate represented by a rapidly increasing current (Figure 6b).

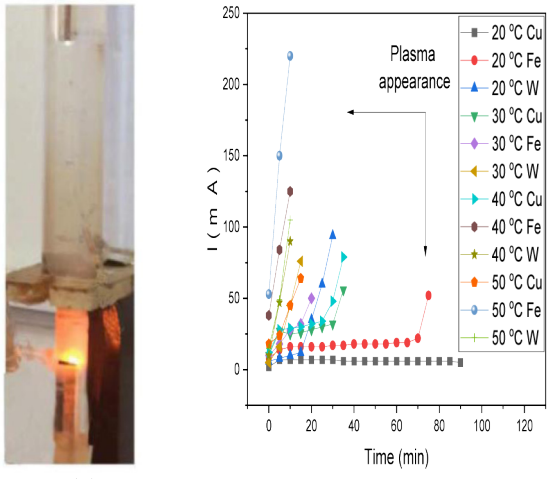

(a) (b)

Figure 6. (a) The appearance of electrochemical plasma on the electrodes, (b) The time-dependent electrochemical reaction rate when plasma appears on the W, Cu, Fe electrodes at different initial temperatures of the aqueous medium. The reaction was carried out at high voltage of 15 kV, pH 7, cathode-anode distance 200 mm and water conductivity 1.4 µS/cm.

From Figure 6a it can be seen that the plasma on the cathode with hydrogen gas is yellow-orange and larger than the plasma on the anode with oxygen gas which is blue due to less gas. In Figure 6b, it can also be seen that the plasma current spikes at different times with the metals W, Cu, Fe and the initial temperature of the different aqueous medium. At the initial temperature of the water environment at 20°C with a potential of 15 kV, the electrochemical plasma appeared on the W electrode at 30 minutes, on the Fe electrode at 70 minutes and on the Cu electrode until 90 minutes, there was still no plasma. As the initial temperature of the aqueous medium increases, the time electrochemical plasma appears gradually accelerates, in which the fastest on the W electrode and the slowest on the Cu electrode. That has to do with the rate and amount of gas escaping on the electrode from DC high voltage DC electrochemical reactions.

The results from Figure 6 show that it is possible to control the electrochemical plasma appearance time by changing the conditions of the high-voltage electrochemical reaction such as: voltage (U_{DC}), distance between anode-cathode (D_{A-C}), initial temperature of aqueous medium (T), pH, electrical conductivity (λ) of the medium as well as the nature (Cu, Fe, W,…) and size ($\varnothing$) of the electrodes.

Table 3. Effect of factors with DC high voltage electrochemical reaction on plasma appearance time on Cu, Fe, W electrodes.

U_{DC}, kV	T, °C	D_{A-C}, mm	pH	$\varnothing$, mm	λ, µS/cm	t_{pl}, min		
						Cu	Fe	W
5	30	200	7	3	1,4	No	No	No
10	30	200	7	3	1,4	60	35	20
15	30	200	7	3	1,4	30	20	5
15	30	220	7	3	1,4	No	35	10
15	30	230	7	3	1,4	No	40	12
15	30	300	7	3	1,4	No	No	15
15	30	200	7	3	20	No	No	9
15	30	200	7	3	50	No	3	2
15	30	200	7	3	100	2	1	< 1
15	30	200	7	3	150	< 1	< 1	< 1
15	30	200	7	3	200	< 1	< 1	< 1
15	20	200	7	3	1,4	No	70	14
15	40	200	7	3	1,4	25	5	4,5
15	50	200	7	3	1,4	5	< 1	< 1
15	30	200	4	3	120	1	< 1	< 1
15	30	200	5	3	69	4	2	1
15	30	200	6	3	52	No	3	2
15	30	200	8	3	40	No	8	7
15	30	200	9	3	60	4	2	1,5
15	30	200	10	3	110	1	< 1	< 1
15	30	200	11	3	150	< 1	< 1	< 1
15	30	200	7	6	1,4	22	15	2

The results presented in Table 3 show that the electrochemical plasma appearance time (t_{pl}) on the electrode has different values, from less than 1 minute to more than 70 minutes or no plasma depending on the conditions of the DC high-voltage electrochemical reaction such

https://doi.org/10.52111/qnjs.2022.16501

as high-voltage, distance between electrodes, temperature, pH and conductivity of the aqueous medium as well as metal nature and size of the electrodes. That allows to master the process using electrochemical plasma. The ionized state has many advantages for different application purposes.

The first advantage is that the amount of gas generated when electrolysis of water by plasma reaction will be more than that of electrochemical reaction calculated according to Faraday's law. Table 4 presents the value of total gas volume (V_{Ex}) performed with DC high-pressure current with plasma at different reaction conditions compared with the value calculated (V_F) according to Faraday's law.

Table 4. Gases volume of the high DC voltage electrochemical process in comparison with the calculation from Faraday law.

Ø, mm	D_{A-C}, mm	t, min	I, mA	V_F, mL	V_{Ex}, mL	V_{Ex}/V_F
3	500	15	93.6	14.7	63	4.3
4	500	25	83.5	21.9	75	3.4
4	500	20	88	18.4	80	4.3
5	500	25	91.2	23.9	110	4.6
5	500	20	87.7	18.4	73	4.0
7	500	25	80.9	21.2	80	3.8
7	500	20	87.5	18.3	61	3.3
4	850	30	115.7	36.4	150	4.1
4	850	18	119.3	22.5	80	3.6
4	850	35	106.7	39.1	250	6.4
4	700	15	112.1	17.6	110	6.3

The results from Table 4 show that the amount of gas contributing to plasma electrolysis is 3.3 to 6.4 times higher depending on the reaction conditions compared to the electrochemical process alone.

The more important advantage of plasma reactions is the generation of active substances such as H_2O_2 and especially $OH^{\bullet}$ radicals (according to Equations 6 to 10).

Figure 7 presents the formation of H_2O_2 with time having electrochemical plasma on the Cu, W, Fe electrodes (Figure 7a) as well as the OH radical on the Fe electrode (Figure 7b).

From Figure 7 it can be seen that both the concentration of H_2O_2 and the free radical $OH^{\bullet}$ increase rapidly during the first 30 minutes, but they then increase slowly because these very active agents are both unstable. Especially with the Fe electrode in an aqueous environment with H_2O_2 will also form a Fenton system (H_2O_2/Fe^{2+}) which also contributes to the formation of $OH^{\bullet}$ free radicals according to the following reaction: $Fe^0 + H_2O_2 + 2H^+ \rightarrow Fe^{2+} + 2H_2O$ (16) and $Fe^{2+} + H_2O_2 \rightarrow Fe^{3+} + OH^{\bullet} + OH^-$ (17).[36-38] Therefore, when using Fe electrode to perform DC high-voltage electrochemical reaction to form plasma, it will be very practical to handle pollutants in water environment because Fe is cheap and can combine advantages of the electrochemical plasma with the Fenton reaction.

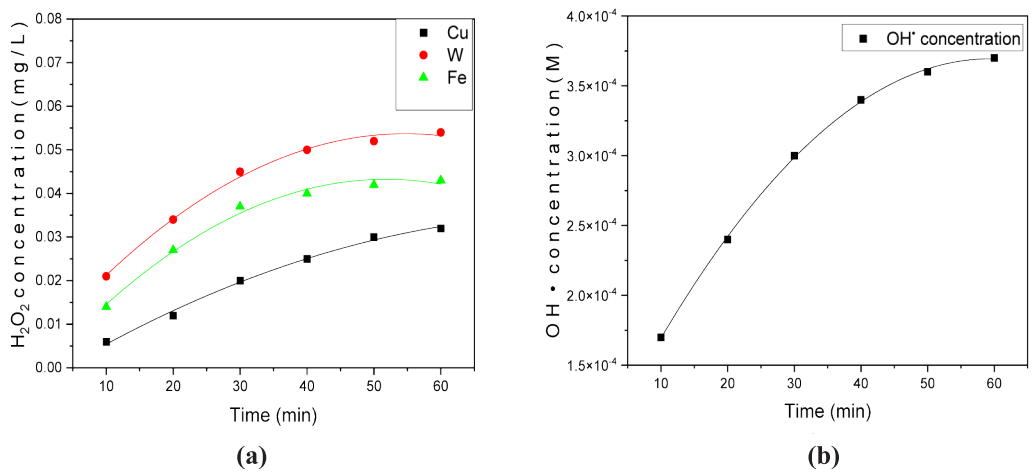

Figure 7. The dependence of the electrochemical plasma lifetime of the H_2O_2 concentration formed at 15 kV, 30°C, D_{A-C} 200 mm on the W, Cu, Fe (a) electrodes as well as the $OH^{\bullet}$ free radical concentration on the Fe electrode (b).

Table 5. Variation with reaction time of chemical oxygen demand (COD) and total organic carbon (TOC) of 2,4-D and 2,4,5-T polluted treatment by DC high voltage and electrochemical plasma at Fe electrode, with U_{DC}: 5 kV, $D_{A\text{-}C}$: 300 mm, T: 30°C, λ: 38,8 µS/cm.

t, min	COD				TOC			
	2,4-D		2,4,5-T		2,4-D		2,4,5-T	
	mg/L	Eff., %	mg/L	Eff., %	mg/L	Eff., %	mg/L	Eff., %
0	106	0	57	0	6.1	0	4.6	0
30	40	62	30.2	47	4.7	22.9	3.7	19.5
60	15.9	85	12.4	78.2	3.7	39.3	2.9	36.9
90	6.8	93.6	8.9	84.3	2.8	54.1	2.4	47.8
120	2.1	98	4.1	92.8	2.1	65.6	1.8	60.6

Table 5 presents the results of treatment of polluted water by 2,4-dichlorophenoxyacetic acid (2,4-D) and 2,4,5-trichlorophenoxyacetic (2,4,5-T) which are aromatic cyclic compounds by electrochemical technique of DC high voltage with plasma on Fe electrode at 5 kV and electrode distance 300 mm.

Very high COD as well as TOC efficiency values show that 2,4-D and 2,4,5-T are well and thoroughly treated to CO_2 and H_2O. Table 6 presents parameters of water polluted by 2,4-D and 2,4,5-T after high voltage DC electrochemical treatment with plasma compared with national standard QCVN 40:2011 and shows that the treated water is grade A and can be discharged directly into the environment.

Table 6. Values of water parameters polluted by 2,4-D and 2,4,5-T treated with high voltage DC and electrochemical plasma on Fe electrode at UDC; 5 kV, DA-C: 300 mm, T: 30°C, λ: 38,8 µS/cm and national standard QCVN 40:2011.

No.	Parameter	Value after pollution treatment		National standard QCVN 40:2011	
		2,4-D	2,4,5-T	A	B
1	$c_{Polu.}$, mg/L	< 0,005	< 0,05	0,05	0,1
2	pH	5,7	5,5	6÷9	5,5÷9
3	COD, mg/L	6,8	8,9	75	150
4	c_{Fe}, mg/L	3,1	4,5	1	5
5	c_{Cl}-, mg/L	7,6	10,7	500	1000
6	TDS, mg/L	14,2	15,8	50	100

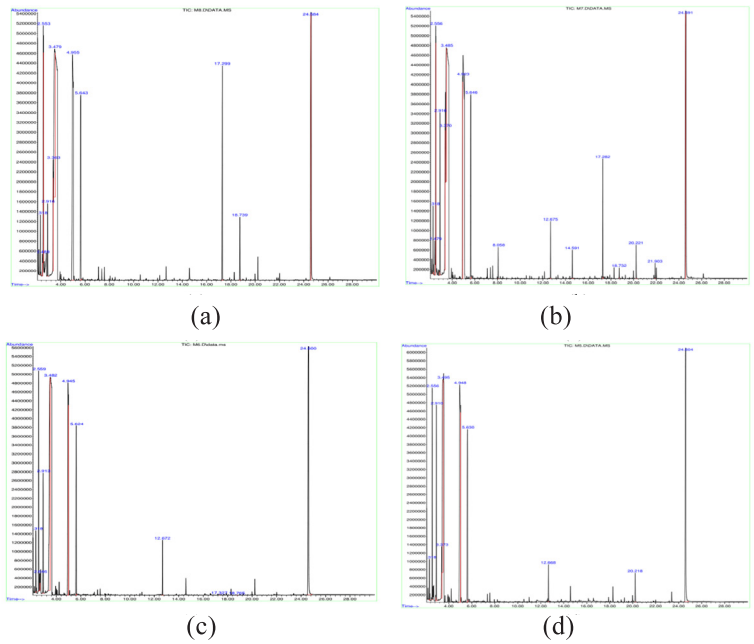

(a) (b) (c) (d)

Figure 8. GC-MS spectrum of 2,4-D degradation products after 30 min (b), 90 min (c) and 120 min (d) of reaction with DC high voltage and electrochemical plasma on Fe electrode at U_{DC}: 5 kV, $D_{A\text{-}C}$: 300 mm, T: 30°C and λ: 38,8 µS/cm.

https://doi.org/10.52111/qnjs.2022.16501

Figure 8 presents the GC-MS spectrum of intermediate products formed by the reaction of 2,4-D or 2,4,5-T pollutants with agents formed from high pressure DC reaction and electrochemical plasma on the Fe electrode at U_{DC}: 5 kV, D_{A-C}: 300 mm, T: 30°C and λ: 38,8 µS/cm.

From the results of GC-MS analysis, it can be seen that the aromatic ring of 2,4-D or 2,4,5-T is oxidized to phenol compounds and then continued to form a straight-chain acid and finally to CO_2 and H_2O, which is represented as a schematic diagram in Figure 9.

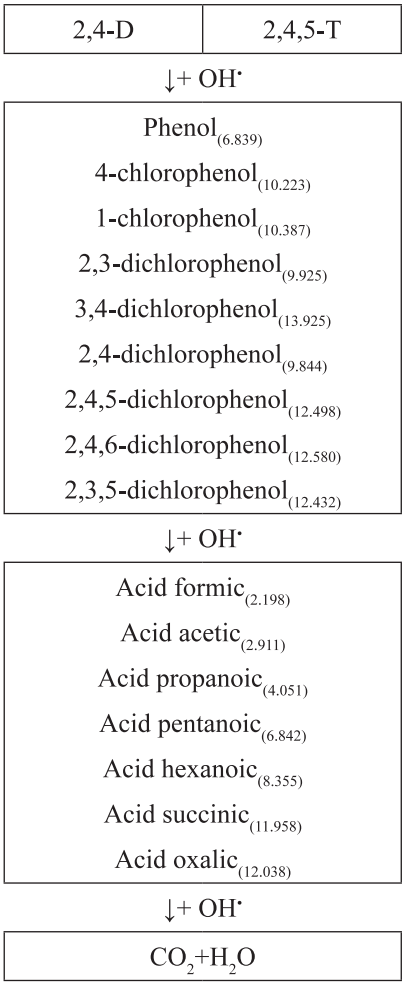

Figure 9. Model of 2,4-D or 2,4,5-T decomposition by DC high voltage with electrochemical plasma

Results of treatment of water contaminated with 300 mg/L methylene blue dye ($C_{16}H_{18}ClN_3S$) by DC high pressure with electrochemical plasma on Fe electrode at U_{DC} 2.5 kV, D_{A-C}: 300 mm, pH: 6.06 and λ: 156 µS/cm presented in Table 7.

Table 7. Time variation of TOC value and treatment efficiency of methylene blue polluted water by DC high pressure with plasma on Fe electrode at U_{DC}: 2.5 kV, D_{A-C}: 300 mm, pH: 6.06 and λ: 156 µS/cm

t, min	0	2	5	10	15
TOC, mg/L	68	40	35	25	12
Eff., %	0	40.2	52.3	88.4	99.6

From the results of Table 7, it can be seen that the treatment efficiency of water contaminated with methylene blue dye is also very high, and the mineralization capacity is determined to 81.9%. This proves that the reaction of the radicals generated by the electrochemical plasma oxidizes methylene blue to CO_2 and water.[39]

By using of DC high-voltage with plasma, it can also be applied to treat liquid waste from hospital biochemical tests with very high concentrations and unknown composition. Figure 10 presents the treatment of wastewater from a hospital biochemical test by DC high-voltage with plasma on iron electrodes with different anode area ratios.

a b c d

Figure 10. The color change of treated wastewater from the hospital's biochemical analytical process by DC high voltage reaction with plasma on iron electrode: (a) S_A/S_C = 1; (b,c,d) S_A/S_C = 4; (a) the pink color of initial solution; (c) turning dark brown color; (b,d) turning blue-black color.

From Figure 10 it can be seen that the color of the solution with biochemical test waste changes color very quickly when treated with a high-pressure DC current with plasma from orange to blue-black. This color change is related to the formation of compounds with iron

ions dissolved from the anode to coagulate and separate from the system.

Table 8. Variation of concentrations of NH_4^+, NO_2^-, NO_3^- as well as COD and TDS at different treatment times with DC high-voltage with plasma on Fe electrode.

t, min	0	78	270
NH_4^+, mg/L	1600	650	490
NO_2^-, mg/L	0.30	3.50	0.25
NO_3^-, mg/L	0	520	250
COD, mg/L	19000	8500	1020
TDS, mg/L	-	4050	3220

Table 8 presents the variation of important values of wastewater such as NH_4^+, NO_2^-, NO_3, COD and TDS depending on the time of wastewater treatment from biochemical tests by DC high-voltage plasma technology. From the results of Table 8, it can be seen that the COD decreases very strongly, demonstrating high treatment efficiency. Interestingly, ammonium is also treated, so its concentration decreases with time while the evolution of NO_2^- and NO_3^- concentrations increases initially and then decreases.[40] That proves that ammonium is oxidized to form NO_2^- and then further into NO_3^-.

5. CONCLUSION

When using high voltage DC, electrochemical reactions can still be performed even in low conductivity water with the anodic dissolution of the metal electrode and the release of hydrogen on the cathode. The rate of electrical energy distribution for electrochemical processes is usually smaller than for the heating of the medium. However, it is possible to control this ratio by reaction parameters such as voltage, distance between the two electrodes, pH and conductivity as well as the temperature of the medium. The products of electrode processes such as metal ions from the anode and hydrogen gas from the cathode disperse into the environment and carry out an oxidation-reduction reaction to form metal and then metal nanoparticle. The nanofabrication process by this method does not use silver salts and reducing agents, so the resulting product is different from other methods in that it has high purity that can be applied to health-related fields because there is no influence of ions such as NO_3^- as well as stabilizers. In addition to metallic silver nano, other metal nanoparticles such as gold, copper, iron, aluminum, tungsten,... can also be prepared by high voltage DC.

With the gaseous environment created on the electrodes in a strong magnetic and electric field as well as an appropriate increase in ambient temperature, a cold plasma state will appear at the electrodes, an ionized state. The hallmark of the electrochemical plasma is the electrode glow and the characteristic amperage of the electrochemical reaction rate that spikes with time. The time of appearance of the electrochemical plasma state can be controlled by electrochemical reaction parameters such as: high voltage DC, distance between electrodes, conductivity or initial temperature of the aqueous medium and the nature of the electrode metals. In the electrochemical plasma state, besides the process of forming metal nanoparticles, it also forms substances with proven strong activators such as H_2O_2 and especially $OH^•$ radicals. The strong reactants of the electrochemical plasma state on the iron electrode with the formation of H_2O_2, the stability of the $OH^•$ radical is supported by the Fenton reaction. The treatment of environmental pollutants with difficult-to-handle aromatic rings such as 2,4-D or 2,4,5-T by high voltage DC with electrochemical plasma on the iron electrode will achieve efficiencies as high as 98% and 92.8% and form the final products CO_2 and H_2O with mineralization up to 65,6% and 60,6%. Similarly, blue methylene dyes are also treated with high yield 99,6% and mineralization 81,9%. Waste from hospital biochemistry tests with very high concentrations of pollutants can also be treated by DC high-voltage with plasma on iron electrodes with high efficiency, especially for contaminant as ammonium NH_4^+.

https://doi.org/10.52111/qnjs.2022.16501

Acknowledgements. *The author would like to thank its doctoral and master students from Institute for Chemistry and Materials, Quy Nhon University and Da Nang University of Science and Education for accompanying this research direction.*

REFERENCES

1. Nguyen Duc Hung. Electrochemical technology and metal protection, *Vietnam Journal of Science and Technology*, **2012**, *50*(6), 767-793.
2. Nguyen Duc Hung, Nguyen Tien Dung. Fabrication of metallic silver nano-solutions using electrochemical method, *Journal of Military Science and Technology*, **2009**, *02*(08), 67-71.
3. Nguyen Duc Hung, Nguyen Minh Thuy, Do Thanh Tuan. Nano aluminum solution prepared by high voltage anodic dissolution process, *Journal of Military Science and Technology*, **2011**, *08*(14), 97 -101.
4. Nguyen Duc Hung, Mai Van Phuoc, Nguyen Minh Thuy. Energy balance in the process of creating silver nanoparticles by high voltage electrochemical technology, *Vietnam Journal of Chemistry*, **2014**, *2*(6B), 326-333.
5. Nguyen Minh Thuy. *Research on dissolution reaction of anode (anodic) to create silver nano solution by high voltage*, Doctoral thesis in Chemistry, Academy of Military Science and Technology - Ministry of National Defense, 2015.
6. Nguyen Duc Hung, Nguyen Minh Thuy, Do Thanh Tuan. *Nano copper solution formed by anodic disoved process under high voltage*, International Workshop on Nanotechnology and Application – IWNA, Vung Tau, 2011.
7. Nguyen Minh Thuy, Nguyen Duc Hung, Nguyen Tien Dung, Mai Van Phuoc. Preparation of metallic silver nano-solutions by ultra-high voltage electrochemical technology to kill bacteria, *Journal of Technique and Equipment*, **2012**, *05*, 43-46.
8. Vo Thanh Vinh, Nguyen Duc Hung, Nguyen Thanh Hai. Formation process of copper nanoparticles from high voltage electrode reaction, *Vietnam Journal of Chemistry*, **2014**, *52*(6B), 1-6.
9. Nguyen Duc Hung, Mai Van Phuoc, Nguyen Minh Thuy. Conductivity of silver nano-solutions, *Journal of Military Science and Technology*, **2012**, *17*, 96-101.
10. Nguyen Duc Hung, Do Thanh Tuan. Preparation of nano iron solution by high voltage anode dissolving process, *Vietnam Journal of Chemistry*, **2012**, *50*(04), 425-428.
11. Nguyen Duc Hung, Nguyen Minh Thuy, Mai Van Phuoc, Nguyen Nhị Tru. Preparation of nanosilver colloidal solution by anodic disolution under high DC voltage, *Electrochemistry*, **2013**, *81*(6), 453-459.
12. Nguyen Minh Thuy, Nguyen Duc Hung, Nguyen Thi Ngoc Tinh, Nguyen Nhi Tru. Silver nano solution prepared by high-voltage electrochemical method: bactericidal ability and application in medicine, *Vietnam Journal of Chemistry*, **2012**, *50*(5A), 134-138.
13. Nguyen Nhi Tru, Nguyen Minh Thuy, Nguyen Duc Hung, Mai Van Phuoc. Characterization of particles size distribution for nano silver solution prepared by high DC voltage electrochemical technique, *Vietnam Journal of Chemistry*, **2012**, *52*(05), 543-547.
14. Nguyen Duc Hung. Electrochemical reaction at high voltage with electrode plasma, *Vietnam Journal of Chemistry*, **2012**, *50*(DB), 103-111.
15. Nguyen Minh Thuy, Nguyen Duc Hung, Nguyen Nhi Tru. The contribution of electrode plasma to nano silver formation in aqueous solution by DC high voltage electrolysis, *Vietnam Journal of Chemistry*, **2015**, *53*(5E1), 119-123.
16. A. K. Susanta, K. Sengupta, R. Singh. A study on the origin of nonfaradaic behavior of anodic contact glow discharge electrolysis – The relationship between power dissipated in glow discharges and nofaradaiic yields, *Journal of the Electrochemical Society*, **1998**, *145*(7), 2209-2213.

17. T. Mizuno, T. Akimoto, K. Azumi, T. Ohmori, Y. Aoki and A. Takahashi. Hydrogen evolution by plasma electrolysis in aqueous solution, *Japanese Journal of Applied Physics*, **2005**, *44*(1A), 396-401.

18. C. Chiuderi, M. Velli. *Basics of plasma astrophysics*, Milano: Springer Milan, 2015.

19. B. Jiang, J. Zheng, S. Qui, M. Wu, Q. Zhang, Z. Yan, Q. Xue. Review on electrical discharge plasma technology for wasterwater remediation, *Chemical Engineering Journal*, **2014**, *236*, 348-368.

20. P. K. Chu, X. P. Lu. *Low temperature plasma technology: Methods and applications*, CRC Press-Taylor & Francis Group, 2013.

21. J. Szalatkiewicz. Metals recovery from artificial ore in case of printed circuit boards, using plasmatron plasma reactor, *Materials (Basel)*, **2016**, *9*(8), 683.

22. Nguyen Duc Hung. The method of manufactoring of nano-silver solution and the equipment to implement this method, the Vietnam patents, VN 1-0012229, 2013.

23. Y. Cui, J. Cheng, Q. Chen, Z. Yin. The types of plasma reactors in wastewater treatment, *Earth and Environmental Science*, **2018**, *208*, 012002.

24. Nguyen Duc Hung, Nguyen Minh Thuy, Nguyen Nhi Tru. Characteristics and electrochemical mechanisms of a nanosilver solution formed by anodic dissolution with high DC voltage, *Journal of Applied Physics*, **2013**, *63*, 20402.

25. Nguyễn Đức Hùng, Vũ Năng Nam, Trần Thị Nhàn, Trần Thị Ngọc Dung. Quantitative concentration determination of silver nanoparticles prepared by DC high voltage electrochemical methothod, *Vietnam Journal of Chemistry*, **2018**, *56*(5), 553-558.

26. Nguyen Duc Hung, Luu Viet Hung, Nguyen Minh Thuy. UV-Vis application to research silver nanosolutions prepared by super high voltage anode dissolving method, *Journal of Military Science and Technology*, **2012**, *19*(06), 94–99.

27. Nguyen Duc Hung, Mai Van Phuoc, Nguyen Minh Thuy. Effect of electrode-electrode spacing on the process of creating silver nanoparticles by super-high voltage anodic dissolution method, *Journal of Science and Technique, University of Military Technique*, **2012**, *149*, 109 –117.

28. Tran Van Cong, Nguyen Duc Hung, Lai Xuan Bach, Tran Van Hung, Nam Nguyen Dang. Factors efecting the formation of plasma on Fe, Cu and W electrodes using an electrochemical reaction in an aqueous environment with high-voltage DC, *Journal of Materials Research and Technology*, **2021**, *10*, 1462-1470.

29. Nguyen Duc Hung, Mai Van Phuoc, Nguyen Minh Thuy. Manufactoring of nano silver solution using electrochemical technology, *Vietnam Jounal of Chemistry*, **2012**, *50*(2), 261–263.

30. Nguyen Duc Hung, Tran Bao Loc, Tran Thi Ngoc Dung. Manufactoring of electrochemical and chemical silver nano solution for prevention and treatment of diarrhea in piglets, *Quy Nhon University Journal of Science*, **2018**, *12*(1), 55-62.

31. Nguyen Duc Hung, Nguyen Thi Thanh Ha, Tran Thi Ngoc Dung. Fabrication of porous ceramic carried silver nano of antibacterials for water treatment from Thi Nai swamp - Binh Dinh, *Quy Nhon University Journal of Science*, **2016**, *10*(4), 139-145.

32. Nguyen Duc Hung, Nguyen Thuy Linh, Tran Thi Ngoc Dung. Research on creating antibacterial nano silver films on glass and porcelain surfaces, *VNU Journal of Science - Natural Sciences and Technology*, **2016**, *32*(4), 53-57.

33. Nguyen Duc Hung, Tran Van Cong, Hoang Nhu Trang. Synthesis of bimetallic Cu-Ag nanoparticles prepared by DC high voltage electrochemical method, *Vietnam Journal of Chemistry*, **2019**, *57*(5), 609-614.

34. Nguyen Duc Hung, Nguyen Minh Thuy, Nguyen Thanh Hai, Phan Thi Trang. Plasma electrolysis effects by the preparation of silver nanoparticles with DC high voltage, *Vietnam Journal of Chemistry*, **2014**, *52*(3), 326–333.

35. Nguyen Duc Hung, Vu Nang Nam, Le Van Trung, Tran Thi Ngoc Dung. Electrochemical

preparation of nano silver by combining high DC voltage with anodic plasma, *Vietnam Journal of Science and Technology,* **2019**, *57*(2), 186-198.

36. Nguyen Van Hoang, Tran Van Cong, Tran Thi Ngoc Dung, Nguyen Duc Hung. Research on the influence of electrode materials on the ability to form plasma and decompose 2,4 dichlorophenynoxy acetic acid in water environment, *Journal of Military science and technology*, **2021**, *72* (04), 53-59.

37. Tran Van Cong, Nguyen Duc Hung, Ngoc Dung Tran Thi, Nguyen Van Hoang. Surya Veerendra Prabhakar Vattikuti, Nam Nguyen Dang. Electrochemical Plasma for Treating 2,4,5-Trichlorophenoxyacetic Acid in Water Environment Using Iron Electrodes, *ACS OMEGA*, **2016**, *6*, 26329-26337.

38. Tran Van Cong, Nguyen Van Hoang, Tran Thi Ngoc Dung, Nguyen Duc Hung. Decomposition of 2,4-D Dichlorophenoxyacetic acid in water environment by the DC high voltage electrochemical reaction with the plasma appearance on iron electrode, *Vietnam Journal of Chemistry*, **2020**, *58*(5E12), 302-308.

39. Nguyen Duc Hung, Pham Hoang Long, Tran Van Cong. Electrochemical plasma application on iron electrodes for wastewater treatment from hospital biochemistry assays, *Journal of Tropical Science and Technology*, **2019**, *18*(07), 46-51.

40. Nguyen Duc Hung, Vu Nang Nam, Tran Thi Ngoc Dung. Applicability of high-voltage electrochemical methods to treat environmental pollution, *Journal of Military Science & Technology*, **2019**, *60*(4), 126-131.

TẠP CHÍ KHOA HỌC
TRƯỜNG ĐẠI HỌC QUY NHƠN

Đánh giá về việc sử dụng các tính toán hóa học lượng tử trong phát triển các cảm biến huỳnh quang

Nguyễn Khoa Hiền[1], Phan Thị Diễm Trân[1,2], Mai Văn Bảy[3], Phạm Cẩm Nam[4], và Dương Tuấn Quang[2,*]

[1]Viện Nghiên cứu Khoa học Miền Trung, Bảo tàng Thiên nhiên Việt Nam, Viện Hàn lâm Khoa học và Công nghệ Việt Nam,Việt Nam
[2]Trường Đại học Sư phạm, Đại học Huế, Việt Nam
[3]Trường Đại học Sư phạm, Đại học Đà Nẵng, Việt Nam
[4]Trường Đại học Bách Khoa, Đại học Đà Nẵng, Việt Nam

Ngày nhận bài: 18/02/2022; Ngày nhận đăng: 28/10/2022; Ngày xuất bản: 28/10/2022

TÓM TẮT

Trong bài đánh giá này, các ứng dụng tính toán hóa học lượng tử được công bố gần đây trong việc phát triển cảm biến huỳnh quang đã được giới thiệu, bao gồm các tính toán trong quá trình phát triển cảm biến huỳnh quang mới dựa trên sự chuyển electron do cảm ứng ánh sáng (PET); nghiên cứu cấu trúc, tính chất và bản chất của các tương tác trong các hợp chất, đặc điểm hấp thụ và huỳnh quang của các hợp chất dựa trên các tính toán của trạng thái cơ bản và trạng thái kích thích, và phân tích obitan liên kết thích hợp (NBO). Các ứng dụng này có thể không toàn diện, nhưng chúng nhằm mục đích làm nổi bật, hướng dẫn và thúc đẩy việc sử dụng các tính toán hóa học lượng tử cho quá trình phát triển các cảm biến huỳnh quang.

Từ khóa: *Tính toán hóa học lượng tử, cảm biến huỳnh quang, PET, trạng thái cơ bản, trạng thái kích thích.*

**Tác giả liên hệ chính.*
Email: dtquang@hueuni.edu.vn

QUY NHON UNIVERSITY
JOURNAL OF SCIENCE

On the use of quantum chemical calculations in the development of fluorescent sensors

Nguyen Khoa Hien[1], Phan Thi Diem Tran[1,2], Mai Van Bay[3], Pham Cam Nam[4], and Duong Tuan Quang[2,*]

[1]Mientrung Institute for Scientific Research, Vietnam National Museum of Nature, Vietnam Academy of Science and Technology, Hue, Vietnam
[2]Department of Chemistry, University of Education, Hue University, Vietnam
[3]The University of Danang, University of Science and Education, Vietnam
[4]The University of Danang, University of Science and Technology, Vietnam

Received: 18/02/2022; Accepted: 28/10/2022; Published: 28/10/2022

ABSTRACT

In this review, recently published quantum chemical computing applications in the development of fluorescent sensors were introduced, including the calculations in the development of the photoinduced electron transfer (PET) - based new fluorescent sensors; the study of structure, property, and nature of interactions, absorption, and fluorescence characteristics of compounds based on calculations of the ground state and excited state, and the natural bond orbital (NBO) analysis. These applications may not be comprehensive, but they aim to highlight, guide and promote the use of quantum chemical computation in the development of fluorescent sensors.

Keywords: *Quantum chemical calculations, fluorescent sensors, PET, ground state, excited state.*

1. INTRODUCTION

Today, along with the development of computer science, from hardware to software, simulation methods and theoretical computation are strongly developed and becoming effective tools in many fields, especially in chemistry,[1] physics,[2] biology,[3,4] medicine,[5,6] and environmental issues[7].

The Nobel Prize in Chemistry 2013 was awarded to the work "the development of multiscale models for complex chemical systems" by Martin Karplus (Université de Strasbourg, France and Harvard University, Cambridge, MA, USA), Michael Levitt (Stanford University School of Medicine, Stanford, CA, USA), and Arieh Warshel (University of Southern California, Los Angeles, CA, USA), implemented since 1970. Before those studies, the Nobel Prize in Chemistry 1995 was awarded to three computational chemists, Paul J. Crutzen, Mario J. Molina, and F. Sherwood Rowland for their work in atmospheric chemistry, particularly concerning the formation and decomposition of ozone. The Nobel Prize in Chemistry 1998 was divided equally between Walter Kohn for his development of the density-functional theory and John A. Pople for his development of computational methods in quantum chemistry. These are considered as a vivid evidence, honoring the effective contributions of computational chemistry.

*Corresponding author.
Email: dtquang@hueuni.edu.vn

https://doi.org/10.52111/qnjs.2022.16502

Up to now, computational chemistry has been successfully applied in various fields. In particular, computational chemistry is widely used in studying the structural characteristics, the nature of bonds and the properties of compounds;[8,9] the ability to participate in reactions, pathways, mechanisms and products of chemical reactions.[10,11] On that basis, computational chemistry has been flexibly applied in many different fields.

In materials research, computational chemistry is used to study the structure,[12] material properties such as ionization energy, binding energy, HOMO and LUMO energy gap,[12] UV-Vis spectra, the catalytic role of metal clusters,[13] the relationship between structure with inhibition of metal corrosion, and metal corrosion remedies.[14,15]

In drug research, computer-aided drug design (CADD) is a computational chemical method that effectively assists in screening and evaluating the biological activity of active ingredients such as inhibitory activity on cancer cells,[16] inhibitory activity on virus and enzymes,[17-19] antioxidant properties, free radicals scavenging activities.[20] This method helps to screen, evaluate and quickly detect active ingredients with desired activity in tens of thousands of research compounds.[21] This helps to reduce significantly the volume of experimental research, shorten the research time, as well as clarify the nature and mechanism of the processes.[22] Therefore, there are many publications on Covid-19 treatment drugs using this method.[23,24]

The main content of this review focuses on introducing recently published quantum chemical computing applications in the development of new fluorescent sensors. These applications may not be comprehensive, but they aim to highlight, guide and promote the use of quantum chemical computation to the development of fluorescent sensors.

2. RESULTS AND DISCUSSION

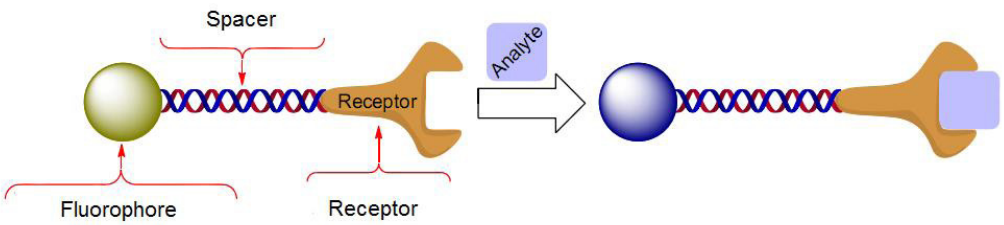

Figure 1. Basic compositions of a fluorescent sensor.[25]

The fluorescent sensors are molecular sensors based on the change of fluorescence signal resulting from the interaction of the analytes with sensors. The fluorescent sensor is typically composed of three main parts: "fluorophore–spacer–receptor" (Figure 1).[25] Figure 2 shows an illustration of a fluorescent sensor with three main parts for detection of HClO in cancer cells.[26]

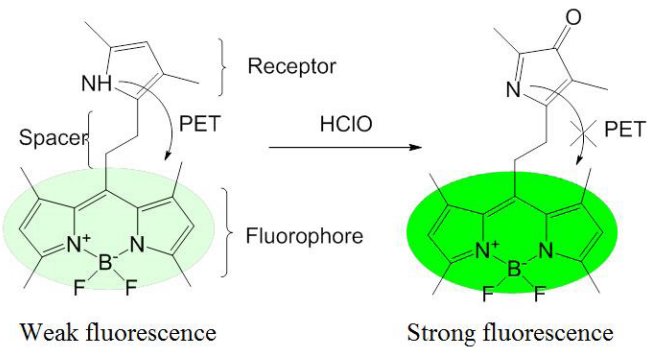

Figure 2. An illustration of fluorescent sensor with three main parts "fluorophore-spacer-receptor".[26]

The first fluorescent sensor is a chemodosimeter based on spirolactam ring-opening process of rhodamine B derivative for the detection of Cu(II) ions, published in 1992 by A. W. Czarnik.[26] Nowadays, the number of published new fluorescent sensors has been rapidly increased. New fluorescent sensors have been reported almost every week in the world.[27] This is because the fluorescent sensors are often sensitive to the analytes, easy to carry out, and less expensive.[28] In particular, fluorescent sensors can be used for detection of some items in living cells like Fe(III) in Hepatic cells,[29] Cu(II) in HepG2 cells,[30] Hg(II) in PC3 cells[31]…

Following the successes of computational chemistry, new computer-aided-developed fluorescent sensors have been published more and more regularly. This is because these processes have made the development of new fluorescent sensors more efficient. In which, quantum chemistry calculations have been orienting experimental research, helping to reduce the volume of experimental studies, increase the probability of success, as well as clarify the nature and mechanism of processes, create a scientific basis for further research.

a) Quantum chemistry calculations in the development of PET (Photoinduced Electron Transfer) - based fluorescent sensors

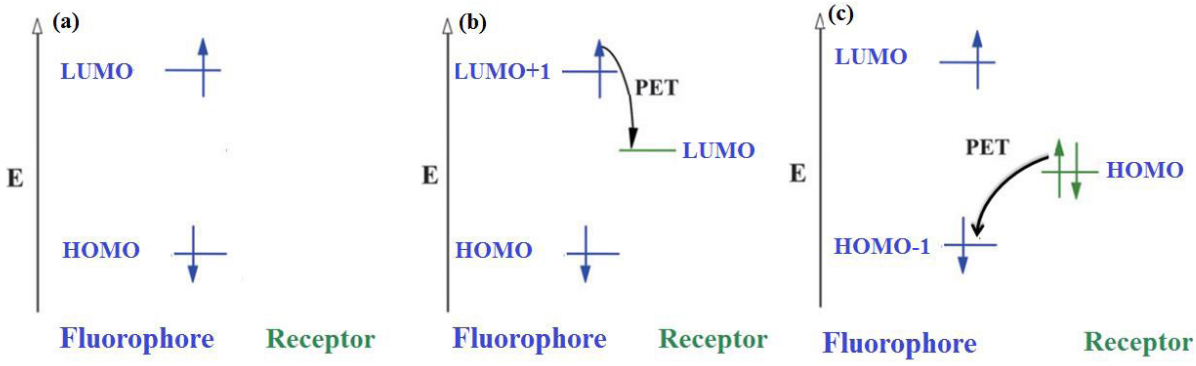

Figure 3. Electron transition process in excited state of fluorescent sensor without PET process (a), with PET process (b), (c).[32,33]

Computational chemistry has been used to study fluorescent sensors which operate based on PET mechanism, mainly the calculations for selection of the appropriate fluorophores and receptors, or for explaination of fluorescent signal changes.[32,33] For fluorescent sensor without PET process, the transition of electron from ground state to excited state takes place in two consecutive MOs (of the fluorophore), LUMO and HOMO (Figure 3a).[32,33] In this case, the de-excitation process is the transition of electron from LUMO to HOMO, and is accompanied by fluorescence emission. Meanwhile, for fluorescent sensor with PET process, the transition of electron from ground to excited state takes place in two non-consecutive MOs (of the flurophore). There is an empty orbital (Figure 3b) or a filled orbital (Figure3c) (of receptor) whose energy level lies between the two orbitals of the transition of electron from ground state to excited state. In this case, the de-excitation process occurs the PET process, which is the transition of electron from LUMO+1 to LUMO (Figure 3b), or from HOMO to HOMO-1 (Figure 3c). This leads to the de-excitation process without fluorescence emission. The reaction between PET sensors and the analytes induces either the presence or the absence of orbital whose energy level lies between the two orbitals in the main transition of the fluorophore, resulting in fluorescence quenching or enhancement, respectively.[32,33]

https://doi.org/10.52111/qnjs.2022.16502

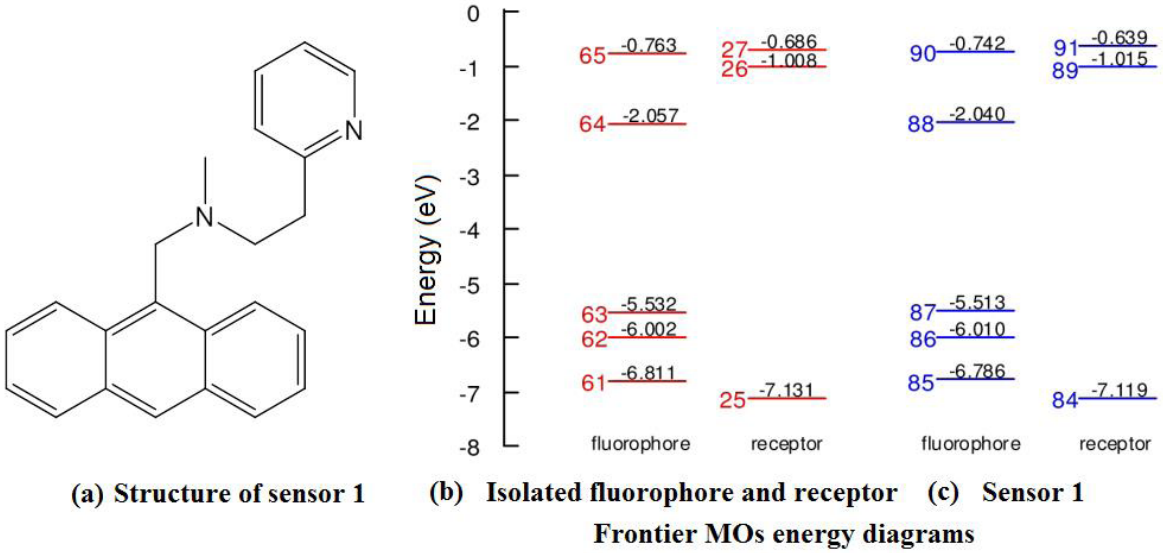

Figure 4. Structure of sensor (a), Frontier MOs energy diagrams of isolated fluorophore and receptor (b), and of sensor **1** (c)[34]

When designing sensor **1** for detection of Zn(II) ion based on anthracene derivative as a fluorophore and pyridine derivative as a receptor, George A. Hudson and co-authors used the density functional theory (DFT)/B3LYP and time-dependent (TD)-DFT/B3LYP methods, with the basis set 6-31G(d,p), 6-31+G(d,p), 6-311G(d,p), and 6-311+G(d,p) to calculate the relative energy levels of the frontier MOs of compounds. The calculation results showed that the relative energy levels of the frontier MOs of compounds were not nearly unchanged when using the above six basis sets. This indicated that any of the above six basis sets can be used in calculating the relative energy levels of the frontier MOs.

The calculation results also showed that the relative energy levels of the frontier MOs of the independent fluorophore and receptor were not nearly altered when they were linked together in sensors (Figure 4). Therefore, it was possible to select fluorophores and receptors for the design of sensors based on the calculation results of the frontier MOs energy levels in the isolated parts. These are promising outcomes for the computational design of sensors.[34]

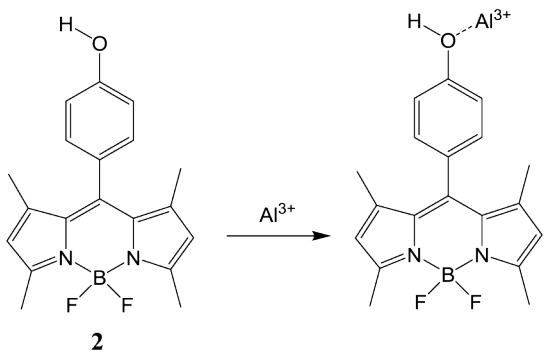

2

Figure 5. Fluorescent sensor **2** for detection of Al(III) based on BODIPY derivative.[35]

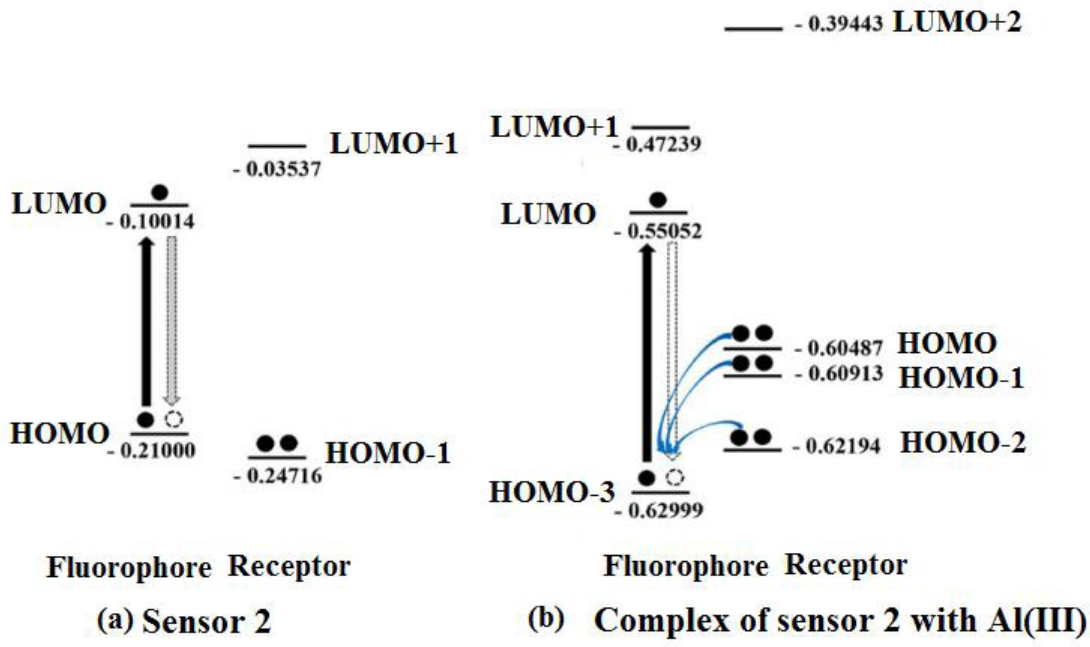

Figure 6. Frontier MOs energy diagrams of sensor **2** (a), complex of sensor **2** with Al(III) (b).[35]

Fluorescent sensor **2** for detection of Al(III) based on BODIPY (boron-dipyrromethene) derivative was published by Tasawan Keawwangchai and co-authors (Figure 5). In this work, the authors used TD-DFT method to explain the experimental results of the change in fluorescent signal before and after the sensor **2** reacted and formed complex with Al(III). In the free state of sensor **2**, the singlet electron transition from the ground state to the excited state was mainly contributed by the HOMO→ LUMO transition. Therefore, the PET process does not occur in sensor **2** and it is a fluorescent compound (Figure 6a). Meanwhile, in the complex of sensor **2** with Al(III), the singlet electron transition from the ground state to the excited state was mainly contributed by the HOMO-3→ LUMO transition (Figure 6b). This leads to the occurrence of PET process and the complex does not emit fluorescence.[35]

In general, on the basis of the operating mechanism of the PET fluorescent sensor, the theoretical calculations have been successfully used in determining the relative energy levels of the frontier MOs of the fluorophore and receptor to design sensors, investigating on the electron transition in excited state to predict or explain the fluorescence properties of compounds.[34-39] The calculated results predicting the fluorescence properties of the compounds were in good agreement with the experimental results.[36-38,39-40] However, this approach may face some limitations. It is only possible to confirm that a compound does not fluoresce when the PET process is determined.[39] In contrast, although the PET process was not found in a compound, it could not be confirmed that it was a fluorescent compound. It is due to many other reasons, for example, the HOMO and LUMO energy gap is too small,[41] the lack of overlapping between HOMO and LUMO.[41,43] In these cases, further study to excited states is essential.

b) Study of the structure, absorption and fluorescence characteristics of compounds based on the calculations of the ground state (GS) and excited states (ESs)

As another application, computational chemistry has been used to study the structure, absorption and fluorescence characteristics of fluorescent sensors and compounds, by using calculations of the GS and Ess.[44-57]

https://doi.org/10.52111/qnjs.2022.16502

Shigehiro Sumiya and co-authors introduced fluorescent sensor **3** for detection of Hg(II) (Figure 7). In this work, the absorption and fluorescence properties of compounds were studied by using DFT and TD-DFT method to calculate the excitation processes based on their optimized geometries at the (GS). The calculation results in Table 1 show that in sensor **3**, the $S_0 \rightarrow S_2$ transition is the most dominant of the singlet electronic transitions from GS to ESs, with an oscillator strength (*f*) of 0.290, much stronger than that of the other transitions. The $S_0 \rightarrow S_2$ transition is mainly contributed by HOMO→LUMO transition, with a largest contribution of 72.27%. The corresponding excitation energy is 2.91 eV (427 nm).[44]

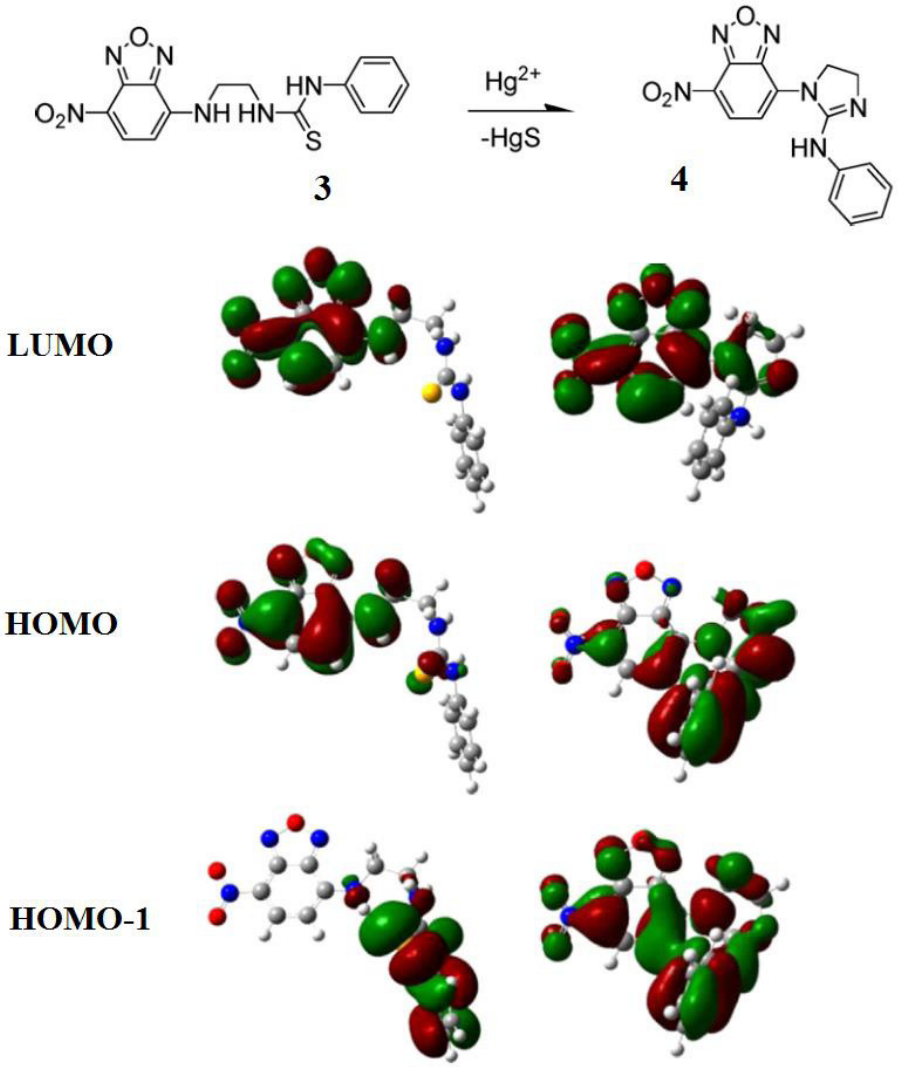

Figure 7. Sensor **3** and frontier MOs of sensor **3** and compound **4.**[44]

For compound **4**, the $S_0 \rightarrow S_2$ transition is also the most dominant of the singlet electronic transitions from GS to ESs, with a greatest oscillator strength (*f*) of 0.333. This transition is mainly contributed by HOMO-1→LUMO transition, with a largest contribution of 75.04%. The corresponding excitation energy is 2.80 eV (443 nm).[44] This calculation results are found be in good agreement with the experimental maximum absorption wavelengths of **3** and **4**, 468 nm and 462 nm, respectively.[44] In sensor **3**, the singlet electron transition from GS to ES takes place in two consecutive MOs (HOMO → LUMO), resulting in no PET process. Meanwhile, in compound **4**, the singlet electron transition from GS to ES takes place in two non-consecutive

MOs (HOMO-1 → LUMO), resulting in PET process.[44] The calculation results of frontier MOs of compounds (Figure 7) also show that, in sensor **3**, the electron density in HOMO and LUMO is predominantly distributed on the NBD moiety. Meanwhile, the electron density in HOMO-1 is predominantly distributed on aniline moiety. Therefore, the PET process from aniline to NBD subunits in the excited state does not occur and sensor **3** is a fluorescent compound. In compound **4**, the electron density in HOMO-1 and LUMO is predominantly distributed on the NBD moiety, the electron density in HOMO is predominantly distributed on aniline moiety. Therefore, the PET process from aniline to NBD subunits in the excited state occurs, and **4** is not a fluorescent compound.[44]

Table 1. Calculated excitation energy (E), wavelength (λ), and oscillator strength (f) for low-laying singlet state of sensor **3** and compound **4**.[44]

Compound	Main transitions		*E*(eV)	*λ*(nm)	*f*	Percentage contribution (%)
3	$S_0 \rightarrow S_1$	HOMO-2→LUMO	2.86	433.2	0.0059	8.64
		HOMO-1→LUMO				88.31
	$S_0 \rightarrow S_2$	HOMO-1→LUMO	2.91	426.7	0.2906	3.19
		HOMO→LUMO				72.27
		HOMO→LUMO+1				5.09
4	$S_0 \rightarrow S_1$	HOMO-1→LUMO	2.34	530.4	0.0397	10.13
		HOMO→LUMO				86.37
	$S_0 \rightarrow S_2$	HOMO-1→LUMO	2.80	442.8	0.3337	75.04
		HOMO→LUMO				5.35

The research results showed that there was a good agreement between the experimental and calculated absorption spectra.[39-44,58] However, it is necessary to select methods, functions and basis sets for the research objects to obtain good results.

For example, there were different methods used to calculate excited states such as TD-DFT, BSE@GW, CIS, CIS(D), ADC(2), CC2, ADC(3), EOM-CCSD, CC3, EOM-CCSDT, SCI, FCI, EOMCCSDTQ, and CASPT2/NEVPT2 methods. Denis Jacquemin and co-authors performed a comparative evaluation of these methods.[59] Each method had its own advantages and limitations. Currently, the TD-DFT method is most commonly used because it is simple, suitable for large molecules,[60] contains many functions, so it can be improved by editing, or adding or subtracting functions.[61]

Duong Tuan Quang and co-authors used the PBE, BP86, PBE0, B3LYP, M06, M06-2X, CAM-B3LYP, LC-wPBE, APDF, wB97XD and PW6B9D3 functions to calculate the maximum absorption wavelength of 21 coumarin derivatives. The results showed that M06-2X functional gave the best predictive performance, with the smallest value of the mean absolute error (MAEfix = 7 nm).[62]

In summary, each method, function or basis set has its own advantages and limitations. They are usually only suitable for specific research purposes and objects. Therefore, it is necessary to evaluate when using, or verifying based on experimental data.

Theoretical investigations on the excitation processes based on optimized ground state geometry (GS) are mainly used to investigate singlet electron transitions from GS to excited

https://doi.org/10.52111/qnjs.2022.16502

states (ESs), thereby predicting or explaining the absorption and fluorescence properties based on excitation process. This method does not directly study the singlet electron transitions from ES to GS. Therefore, the nature of the fluorescence emission process is not clarified, the fluorescence emission wavelength cannot be determined exactly. This is only solved when calculations on optimized geometries of excited states (ESs) are used to directly study the singlet electron transitions from ESs to GS.[48]

Figure 8 shows the Jablonski diagram for calculation of excitation energy and fluorescence emission energy in a simple case. Accordingly, the vertical absorption energy ($E^{vert\text{-}abso}$) from GS to ES is the difference between the energy of ES and GS at the ground state optimized geometry (R^{GS}). The vertical fluorescence energy ($E^{vert\text{-}flu}$) from ES to GS is the difference between the energy of ES and GS at the excited state optimized geometry (R^{ES}).[49,50]

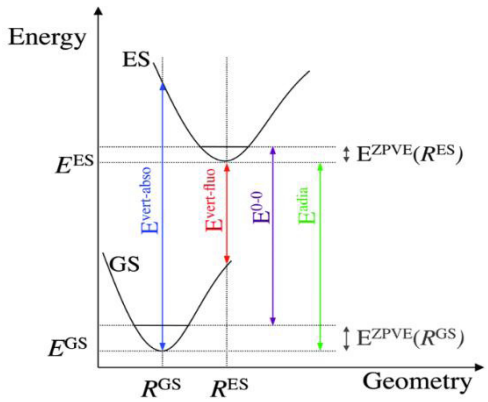

Figure 8. Jablonski diagram for calculation of excitation energy and fluorescence emission energy.[49,50]

Nguyen Khoa Hien and co-authors introduced fluorescent sensor **5** for detection of biothiols (Figure 9). The results of the theoretical investigations on the electron excited states by TD-DFT method show that the fluorescence of the product of the addition reaction between sensor **5** and biothiols is not in accordance with Kasha's rule. This is an exception from the Kasha's rule. Fluorescence emission occurs from the higher lying singlet electron excited state (S_2) instead of the lowest lying singlet electron excited state (S_1). This is because the electron transition from S_1 to S_0 is forbidden since the lack of overlapping between MOs in transition, and the small energy gap between S_2 and S_1 excited states. The fluorescence from the higher-lying singlet electron excited states leads to markable fluorescence enhancement at long wavelength in the products of addition reaction between biothiols and sensor **5**.[43]

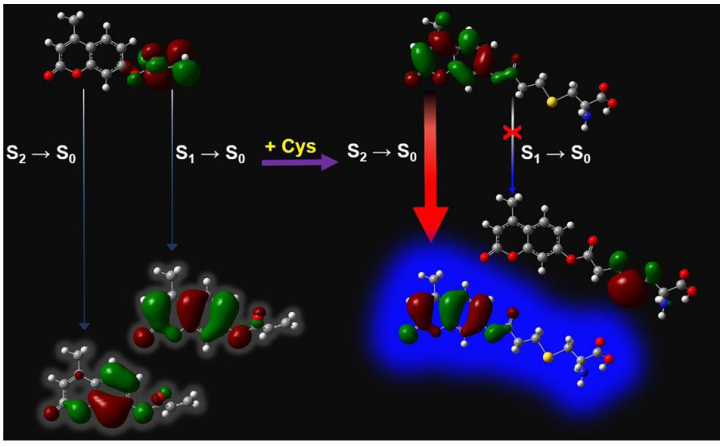

Figure 9. Sensor **5** for detection of bithiols based on coumarin derivative.[43]

Caterina Bernini and co-authors investigated the excited state geometries and emission energies of 11 organic D-π-A dyes, with using the CAM-B3LYP, MPW1K, ωB97X-D, LC-BLYP, LC-ωPBE, and M06-HF functionals, in combination with the cc-pVDZ, 6-31+G(d,p), and 6-311+G(2d,p) basis sets. Polarizable Continuum Model was also performed in both LR and SS formalisms. The LR-PCM/TD-DFT results showed that accurate emission energies were obtained only when solvent effects and a range separated hybrid functional was used. The maximum mean absolute error of the vertical emission energy was 0.2 eV. The accuracy was further improved using the SS-PCM formalism.[56] According to this approach, some publications have successfully applied to investigate on the absorption and fluorescence spectra of compounds, as evidenced by a quite good agreement between theoretical calculations and experimental results.[51-55] However, calculation on optimized geometry of excited states is not simple. This requires an extremely strong configuration of computer system rather than calculations on optimized geometry of ground state, especially for large compounds, complexes and in the environment of solvents. Therefore, up to now, the calculations on excited state optimized geometry are still very rarely published, and mainly used for small and simple compounds.[51-55]

In addition, theoretical investigations on excitation processes are also applied to study the mechanisms of some other processes, such as the excited state intramolecular proton transfer (ESIPT),[56] twisted intramolecular charge transfer (TICT)[57]...

Yang Li and Tian-Shu Chu used DFT and TD-DFT methods to study the excitation processes of fluorescent compound **6** (Figure 10). The calculated results on the optimized geometry and energy of the ground state and excited states show that there is an ESIPT process. Accordingly, compound **6** exists as an enol in its ground state. In the excited state, it converts to compound **7** in the keto form through an ESIPT process, resulting in a shift in fluorescence emission to the long wavelength region.[56]

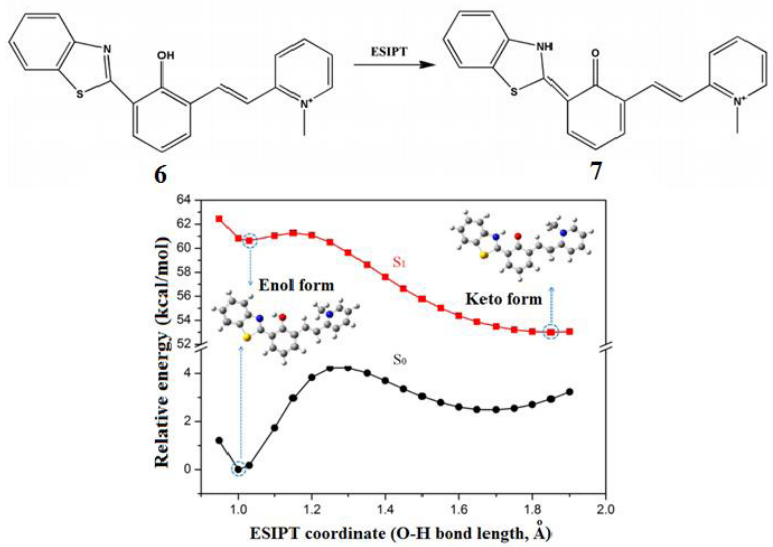

Figure 10. Theoretical investigation of an ESIPT case in fluorescent compound **6**.[56]

When utilizing DFT and TD-DFT methods to study the fluorescence properties of 4-N, N-dimethylamino cinnamaldehyde (**8**), Surajit Ghosh and co-authors reported that, after being excited, compound **8** undergone the twisted intermolecular transformation to reach a minimum on the potential energy surface (PES), accompanied by twisted intramolecular charge transfer (TICT), resulting in a transition from locally excited (LE) state to TICT excited state

https://doi.org/10.52111/qnjs.2022.16502

(Figure 11). Due to the intramolecular charge transfer, the polarization of the TICT state was higher than that of the LE state. As a result, the TICT state was more stable than the LE state in solvents of greater polarity. This led to a red shift in fluorescence emission and absorption, from weaker polar solvents to stronger polar solvents.[57]

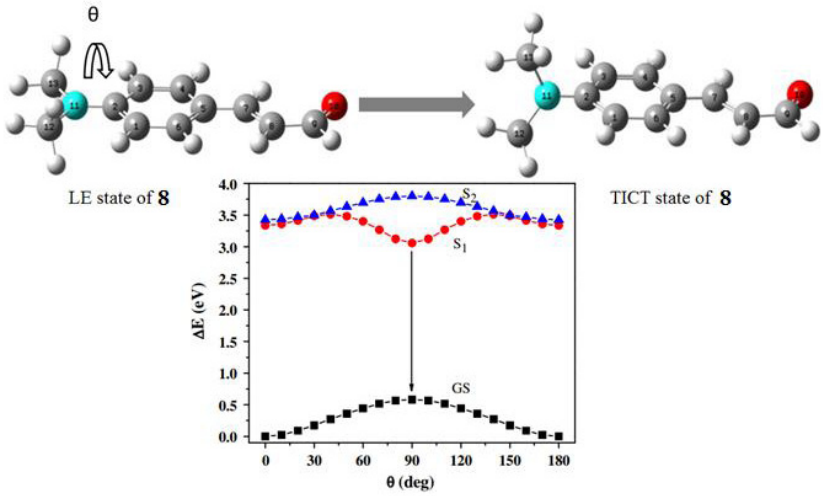

Figure 11. Theoretical investigation of an TICT case in fluorescent compound **8**.[57]

Mai Van Bay and co-authors introduced fluorescent sensor **9** for detection of Hg(II) ions (Figure 12).[43] The DFT calculation results show that **9** molecule is composed of three moieties, in which ethylenediamine as a spacer is the bridge between rhodamine and dimethylamino-cinnamaldehyde (DACA). Rhodamine moiety in **9** exists in the spirolactam ring form and is not a fluorescent compound. Although the configuration of the DACA moiety in **9** is unchanged from the free state of DACA fluorophore, **9** is a non-fluorescent compound. This has been clarified when studying excitation states. TD-DFT calculation results show that after being excited, the molecule **9** undergoes intramolecular twisting, accompanied by the process of the twisted intermediate charge transfer (TICT). As a result, there is a transition from the locally excited (LE) state to the TICT excited state. Consequently, the $S_1 \rightarrow S_0$ de-excitation occurs at TICT state. Unfortunately, the strong charge transfer in the TICT state leads to a complete difference in the localization of electron density, resulting in the lack of overlapping between HOMO and LUMO. The $S_1 \rightarrow S_0$ transition at TICT state is strongly forbidden. These may be the reasons why RLED does not fluoresce.[43]

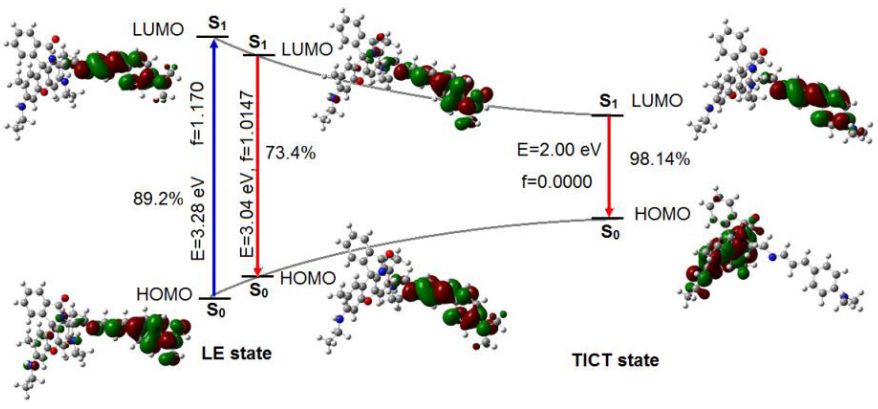

Figure 12. TD-DFT calculations used to explain the fluorescence properties of **9**.[43]

c) Study of the structure, property and nature of interactions in compounds, absorption and fluorescence characteristics of compounds based on the natural bond orbital (NBO) analysis

When studying fluorescent sensors, a fairly common application of computational chemistry is the use of NBO analysis to investigate the structure, property and nature of interactions in compounds. The calculation results obtained from NBO analysis are mainly second-order interaction energy and charges of atoms in molecules. The second-order interaction in NBO analysis is the interaction between the NBO donor and NBO acceptor. The greater second-order interaction energy leads to the stronger interaction, the more stable bond, and the greater degree of conjugation in the system. Therefore, NBO analysis is often used to investigate the degree of conjugation of the π electron system, thereby explaining the fluorescence properties, as well as comparing the durability of compounds based on the value of the second-order interaction energy.[63-65]

When studying a fluorescent sensor for detection of Fe(III) based on 4-(2-hydroxybenzylideneamino) benzoic acid (**10**), Gurpreet Singh and co-authors computed NBO analysis to study the fluorescence properties of compounds. The calculation results showed that there existed a π electron conjugation system in the molecule of sensor **10**. That caused sensor **10** to be fluorescent (Figure 13).[63]

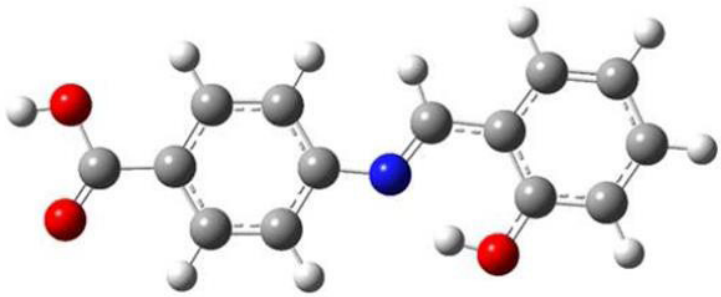

10

Figure 13. Fluorescent sensor **10** for detection of Fe(III).[63]

When studying fluorescent sensor **11** used for detection of Cu(II) and Hg(II) (Figure 14), Yong Xia and co-authors conducted NBO analysis to investigate on the interactions in complexes between sensor **11** with metal ions including Cu(II), Hg(II), Zn(II), Cd(II), and Pb(II). The calculation results showed that the complexes were stabilized mainly by donor-acceptor interactions from lone pair (LP) of the O and N atoms to the empty LP* or RY* (Rydberg) orbitals of the central metal ions. In this case, the interactions from the LP of the N atoms to the LP* or the RY* of the metal ions were much stronger than the interactions from the LP of the O atoms. The calculation results also showed that these interactions in Hg(II) complex were stronger than those in Cu(II) complex, and even stronger than in other complexes. As a result, the most stability was Hg(II) complex, followed by the Cu(II) complex, and then the other complexes. These results were completely consistent with the calculation results in which the Gibbs free energy of complexation reaction of **11** with Hg(II), Cu(II), Zn(II), Cd(II), and Pb(II) was -433.3, 386.9, 333.6, 276.7, and 236.6 kcal.mol^{-1}, respectively. These results led to the prediction that Hg(II) may react to displace Cu(II) from the complex between Cu(II) and sensor **11**. Therefore, sensor **11** could also be used to detect Hg(II).[64]

https://doi.org/10.52111/qnjs.2022.16502

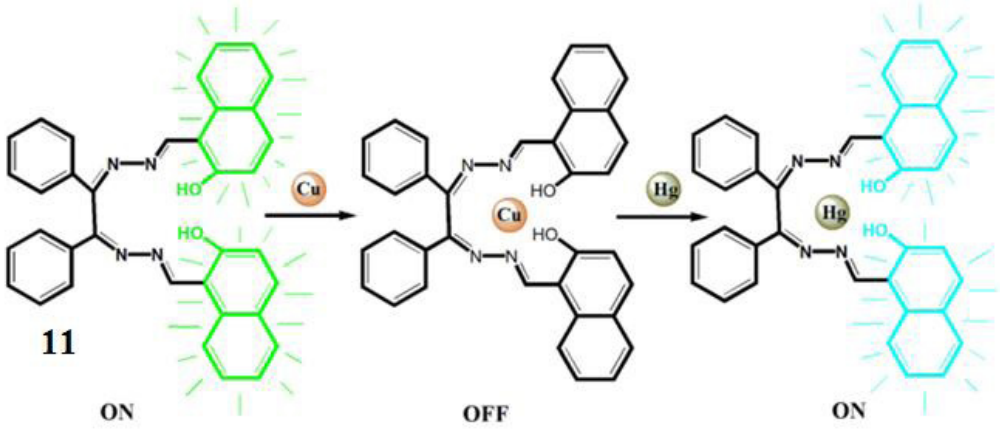

Figure 14. Fluorescent sensor **11** for detection of Cu(II) and Hg(II).[64]

A fluorescent sensor (**12**) based on benzothiazolium hemicyanine derivative for Hg(II) detection was synthesized and studied by Doan Thanh Nhan and co-authors (Figure 15).[41] Free sensor **12** exhibited a red emission at 585 nm. Hg(II) coordinated to ligand **12** with a stoichiometry of 1:1 and led to the fluorescence quenching. The detection limits of the colorimetric and fluorescent method are 15.3 and 11.8 ppb, respectively. The optimized molecular structures, absorption and fluorescence characteristics of the sensor L and its complex with mercury ions were carried out using the calculations at the B3LYP/LanL2DZ level of theory, combined with Atoms In Molecules and Natural Bond Orbitals analyses. The NBO analysis results showed that the complex was stabilized mainly by donor-acceptor interactions from lone pair (LP) of the O and S atoms to the empty LP* orbitals of the central mercury atom. The formation of these interactions led to a significant transfer of electron density from ligands to the metal ions, and broke the π-electron conjugated system in the **12** ligands. This was an important factor leading to fluorescence quenching and color change in the complex.

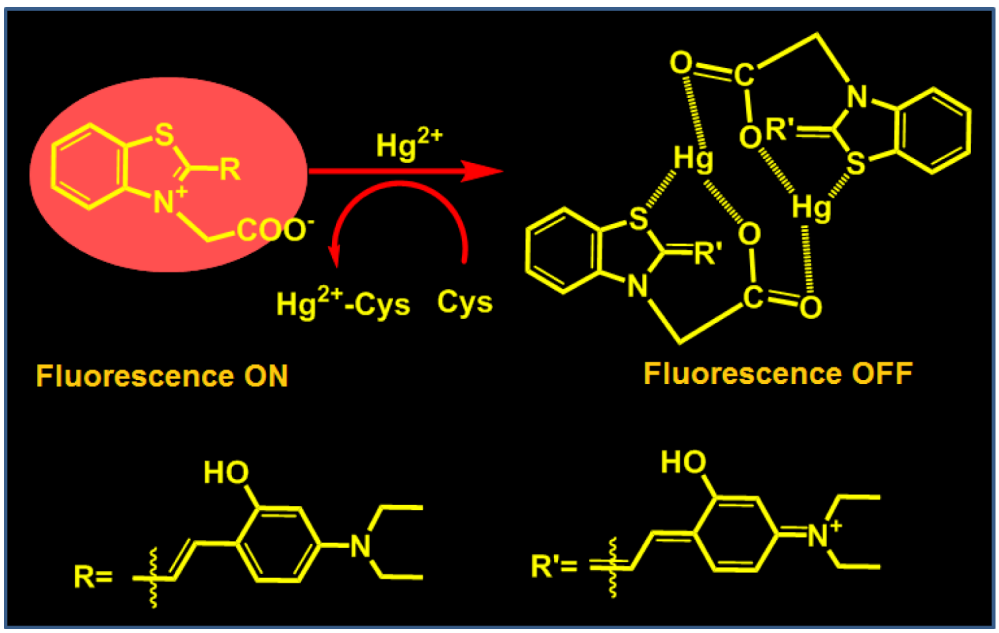

Figure 15. Fluorescent sensor **12** for detection of Hg(II) based on benzothiazolium hemicyanine derivative.[41]

d) Determine values of energy and constants for reactions based on the optimized geometries and the single point energies of the compounds

Sairam S Mallajosyula and co-authors used computational chemistry to study the mechanism of action of a 1,3-dithiole-2-thione-based fluorescent sensor (**13**) (Figure 16). The optimized geometric structures of sensor **13** and its complexes with metals and water were carried out using the DFT method and the B3LYP/LanL2DZ level of theory. From these structures, the authors calculated the formation energy of complexes and determined the pathway of complex exchange reaction between $As(H_2O)_3$ and ligand P (sensor **13**). The calculation results also showed that the formation of AsP_3 complex was more thermodynamically favorable than that of HgP_4 complex, with more negative formation energy of -174.19 kcal.mol^{-1}. Since then, sensor **13** was predicted to be more selective detection of As(III), compared with Hg(II).[65]

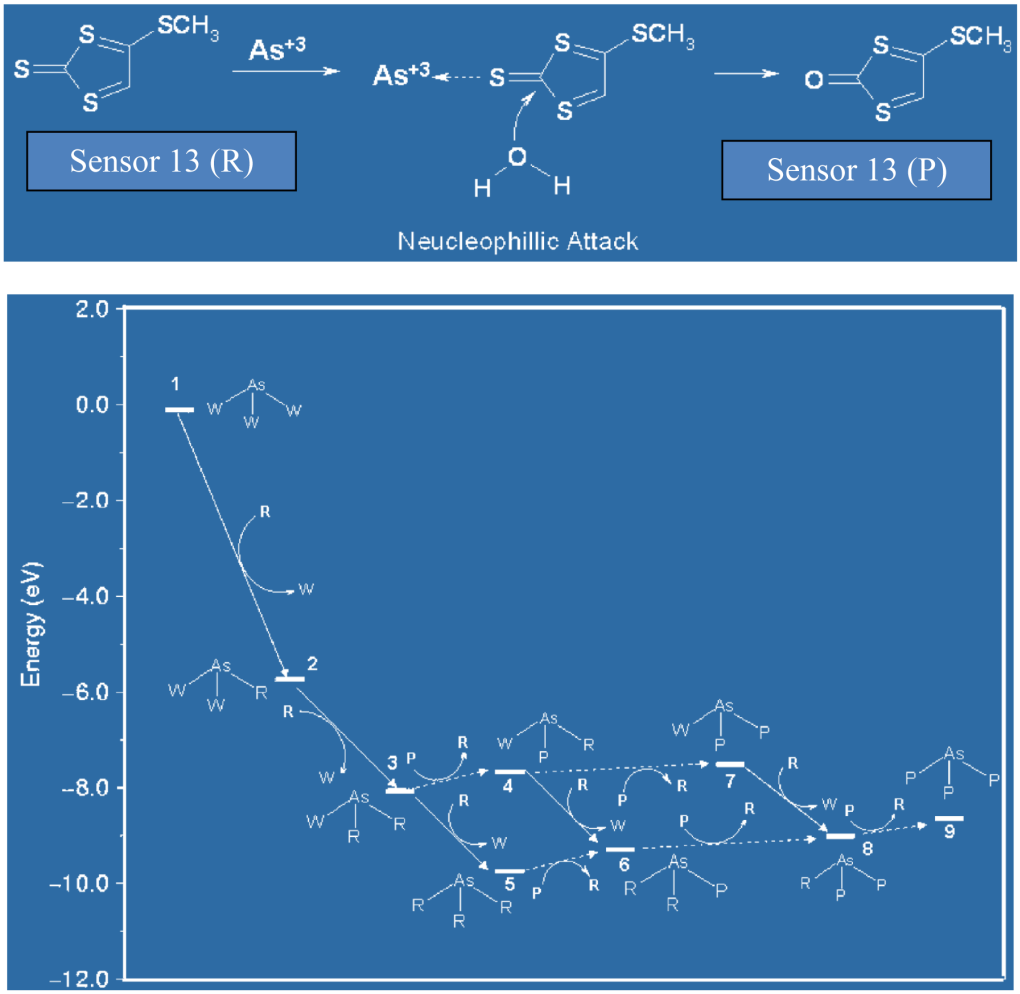

Figure 16. Theoretical investigation on mechanism of action of fluorescent sensor **13** (W: H_2O, R: reactant, P: product).[65]

To investigate the possibility of using the complex between **14** and Cu(II) as a fluorescent chemosensor for detection of biothiols (Figure 17a), Nguyen Khoa Hien and co-authors used the theoretical calculations of the stability constant of complex.[58] Accordingly, the theoretical stability constant of the complex was theoretically calculated based on the solvation model and the Gibbs free energy of ligand-exchange reactions, obtained from the thermodynamic cycle (Figure 17a). As a result, the calculated complexation equilibrium constant of 14-Cu(II) was 10^7.[16]

https://doi.org/10.52111/qnjs.2022.16502

This value of complexation equilibrium constant of Cu(II) ions with **14**, was much smaller than of Cu(II) ions with biothiols. These results led to an expectation that the complex of **14** with Cu(II) ions could be used as a fluorescent sensor for detection of biothiols based on the complex exchange reactions. The obtained results were in good agreement with the experimental data. The **14**-Cu(II) complex could be used as a fluorescent sensor for detecting biothiols in the presence of non-thiols containing amino acids, with a detection limit for cysteine of 0.3 μM.[58]

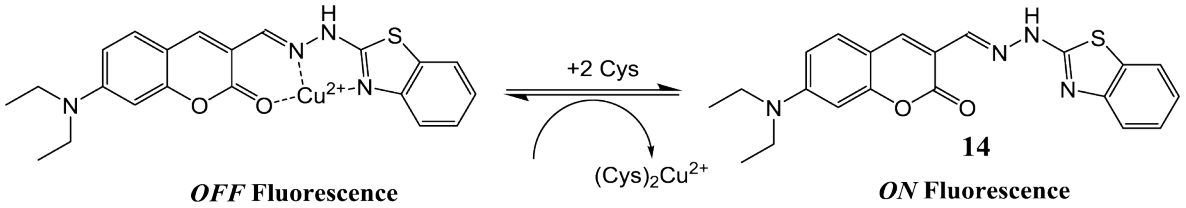

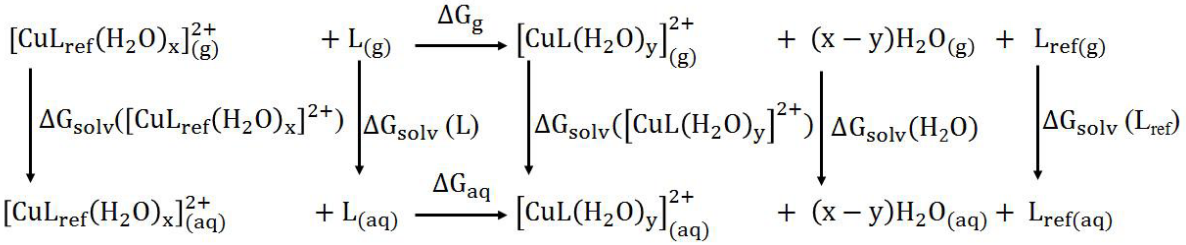

Figure 17. (a) Illustrative diagram of the reaction between the **14**-Cu(II) complex and Cys; (b) Thermodynamic cycle for the calculation of Gibbs free energy of ligand-exchange reaction in aqueous solution, ΔGaq.[58]

3. CONCLUSIONS

This review introduced the recently published quantum chemical computing applications in the development of PET-based fluorescent sensors. It was involved in the study of the structure, absorption, and fluorescence characteristics of compounds based on the calculations of the ground and excited states; the study of the structure, property, and nature of interactions in compounds, absorption and fluorescence characteristics of compounds based on the NBO analysis; and determination of energies and constants for reactions based on the optimized geometries and the single point energies of the compounds.

The results showed that quantum chemical calculations have been successfully used in the design and development of new fluorescence sensors, predicting as well as explaining the absorption and fluorescence properties of compounds. The calculated results are more significant when combined with experimental studies. This combination is to increase the likelihood of success, reduce the volume of experimental study, and create the scientific basis to adjust and recommend appropriate calculation methods for next studies.

REFERENCES

1. E. G. Lewars. *Computational chemistry. Introduction to the theory and applications of molecular and quantum mechanics*, Third edition, Springer, 2016.
2. P. O. J. Scherer. *Computational physics. Simulation of classical and quantum systems*, Third edition, Graduate Texts in Physics, Springer, 2017.
3. R. Wunschiers. *Computational Biology,* First edition, Springer-Verlag, New York, LLC, 2004.
4. S. Shankar, T. Dunning, R. Muller, G. H. Chen (Editors). *Computational materials, chemistry, and biochemistry: From bold initiatives to the last mile. In honor of William A. Goddard's contributions to science and engineering*, Springer Series in Materials Science, Springer, 2020.

5. Nguyen Minh Tam, Minh Quan Pham, Huy Truong Nguyen, Nam Dao Hong, Nguyen Khoa Hien, Duong Tuan Quang, Huong Thi Thu Phung and Son Tung Ngo. Potential inhibitors for SARS-CoV-2 Mpro from marine compounds, *RSC Advances*, **2021**, *11*, 22206-22213.

6. L. Gorb, V. Kuz'min, E. Muratov (Editors). *Application of Computational Techniques in Pharmacy and Medicine (Challenges and Advances in Computational Chemistry and Physics 17)*, Springer, 2014.

7. M. F. Acevedo. *Simulation of ecological and environmental models*, CRC PRESS, 2017.

8. N. Kerru, L. Gummidi, S. V. H. S. Bhaskaruni, S. N. Maddila, P. Singh and S. B. Jonnalagadda. A comparison between observed and DFT calculations on structure of 5-(4-chlorophenyl)-2-amino-1,3,4-thiadiazole, *Scientific Reports*, **2019**, *9*(1), 19280.

9. S. Mirdoraghi, F. Piri and M. Vahedpour. A computational study on multiple formaldehyde complexes and their possible chemical reactions as well as the catalytic effect in the gas phase, *SN Applied Sciences,* **2020**, *2*, 623.

10. C. A. Grambow, L. Pattanaik and W. H. Green. Reactants, products, and transition states of elementary chemical reactions based on quantum chemistry, *Scientific Data*, **2020**, *7*, 137.

11. S. Liu, Y. Wu, C. Zhou, J. Wu and Y. Zhang. Study on the CO formation mechanism during coal ambient temperature oxidation, *Energies*, **2020**, *13*(10), 2587.

12. R. Hussain, M. Saeed, M. Y. Mehboob, S. U. Khan, M. U. Khan, M. Adnan, M. Ahmed, J. Iqbal and K. Ayub. Density functional theory study of palladium cluster adsorption on a graphene support, *RSC Advances*, **2020**, *10*(35), 20595-20607.

13. A. Dutta, P. Mondal. Density functional approach toward the adsorption of molecular hydrogen as well as the formation of metal hydride on bare and activated Carbon-supported rhodium clusters, *Journal of Physical Chemistry C,* **2018**, *122*(29), 16925–16939.

14. V. Chauhan, A. C. Reber and S. N. Khanna. Strong lowering of ionization energy of metallic clusters by organic ligands without changing shell filling, *Nature Communications*, **2018**, *9*, 2357.

15. Duy Quang Dao, Truong Dinh Hieu, Thong Le Minh Pham, Dinh Tuan, Pham Cam Nam, I. B. Obot. DFT study of the interactions between thiophene-based corrosion inhibitors and an Fe_4 cluster. *Journal of Molecular Modeling*, **2017**, *23*(9), 260.

16. H. L. Abdulrahman, A. Uzairu & S. Uba. Computer modeling of some anti-breast cancer compounds, *Structure Chemistry*, **2021**, *32*, 679–687.

17. S. Rampogu, D. Ravinder, S. C. Pawar, and K. W. Lee. Natural compound modulates the cervical cancer microenvironment-A pharmacophore guided molecular modelling approaches, *Journal of Clinical Medicine*, **2018**, *7*(12), 551.

18. K. Klimenko. *Computer-aided drug design of broad-spectrum antiviral compounds*, Université de Strasbourg, 2017.

19. Z. Jin, X. Du, Y. Xu et al. Structure of Mpro from SARS-CoV-2 and discovery of its inhibitors, *Nature*, **2020**, *582*, 289–293.

20. Mai Van Bay, Pham Cam Nam, Duong Tuan Quang, Adam Mechler, Nguyen Khoa Hien, Nguyen Thi Hoa, and Quan Van Vo. Theoretical study on the antioxidant activity of natural depsidones, *ACS Omega*, **2020**, *5*(14), 7895–7902.

21. Son Tung Ngo, Ngoc Quynh Anh Pham, Ly Thi Le, Duc-Hung Pham, and Van V. Vu. Computational determination of potential inhibitors of SARS CoV-2 main protease, *Journal of Chemical Information and Modeling*, **2020**, *60*(12), 5771-5780.

22. M. Hariono, D. B. E. Wijaya, T. Chandra, N. Frederick, A. B. Putri, E. Herawati, L.i A. Warastika, M. Permatasari, A. D. A. Putri, and S. Ardyantoro. A decade of Indonesian atmosphere in computer-aided drug design, *Journal of Chemical Information and Modeling*, **2021**, (DOI: 10.1021/acs.jcim.1c00607).

https://doi.org/10.52111/qnjs.2022.16502

23. Bui Thi Phuong Thuy, Tran Thi Ai My, Nguyen Thi Thanh Hai, Le Trung Hieu, Tran Thai Hoa, Huynh Thi Phuong Loan, Nguyen Thanh Triet, Tran Thi Van Anh, Phan Tu Quy, Pham Van Tat, Nguyen Van Hue, Duong Tuan Quang. Investigation into SARS-CoV-2 resistance of compounds in garlic essential oil, *ACS Omega*, **2020**, *5*(14), 8312-8320.

24. D. Gopal, S. Skariyachan. Recent Perspectives on COVID-19 and computer-aided virtual screening of natural compounds for the development of therapeutic agents towards SARS-CoV-2, *In: Methods in Pharmacology and Toxicology*, Springer, New York, 2020.

25. A. P. D. Silva, T. S. Moody and G. D. Wright. A fluorescent chemodosimeter based on rhodamine derivative for detection of Hg(II) ions studied by using the density functional theory, *Analyst*, **2009**, *134*, 2385–2393.

26. H. Zhu, J. Fan, J. Wang, H. Mu, and X. J. Peng. An "Enhanced PET" - based fluorescent probe with ultrasensitivity for imaging basal and elesclomol-induced HClO in cancer cells, *Journal of the American Chemical Society*, **2014**, *136*(37), 12820–12823.

27. M. Y. Chae and A. W. Czarnik. Fluorometric chemodosimetry. Mercury(II) and silver(I) indication in water via enhanced fluorescence signaling, *Journal of the American Chemical Society*, **1992**, *114*(24), 9704-9705.

28. Duong Tuan Quang and Jong Seung Kim. Fluoro- and chromogenic chemodosimeters for heavy metal ion detection in solution and biospecimens, *Chemical Reviews*, **2010**, *110*(10), 6280-6310.

29. M. H. Lee, T. V. Giap, S. H. Kim, Y. H. Lee, C. Kang, J. S. Kim. A novel strategy to selectively detect Fe(iii) in aqueous media driven by hydrolysis of a rhodamine 6GSchiff base, *Chemical Communications*, **2010**, *46*, 1407-1409.

30. H. S. Jung, J. H. Han, Y. Habata, C. Kang and J. S. Kim. An iminocoumarin–Cu(ii) ensemble-based chemodosimeter toward thiols, *Chemical Communications*, **2011**, *47*, 5142–5144.

31. M. Kumar, N. Kumar, V. Bhalla, H. Singh, P. R. Sharma, and T. Kaur. Naphthalimide appended rhodamine derivative: Through bond energy transfer for sensing of Hg2+ Ions, *Organic Letter*, **2011**, *13(6)*, 1422-1425.

32. B. Valeur. *Molecular fluorescence*: *Principles and applications,* Wiley-VCH: Weinheim – New York – Chichester – Brisbane – Singapore – Toronto, 2001.

33. Y. Yang, Q. Zhao, W. Feng, and F. Li. Luminescent chemodosimeters for bioimaging. *Chemical Reviews*, **2013**, *113*, 192-270.

34. G. A. Hudson, L. Cheng, J. Yu, Y. Yan, D. J. Dyer, M. E. McCarroll, and L. Wang. Computational studies on response and binding selectivity of fluorescence sensors, *Journal of Physical Chemistry B*, **2010**, *114*(2), 870-876.

35. T. Keawwangchai, N. Morakot, B. Wanno. Fluorescent sensors based on BODIPY derivatives for aluminium ion recognition: an experimental and theoretical study, *Journal of Molecular Modeling,* **2013**, *19*, 1435-1444.

36. F. Han, L. Chi, X. Liang, S. Ji, S. Liu, F. Zhou, Y. Wu, K. Han, J. Zhao, T. D. James. 3,6-disubstituted carbazole-based bisboronic acids with unusual fluorescence transduction as enantioselective fluorescent chemosensors for tartaric acid, *Journal of Organic Chemistry*, **2009**, *74*, 1333–1336.

37. X. Zhang, L. Chi, S. Ji, Y. Wu, P. Song, K. Han, H. Guo, T. D. James, J. Zhao. Rational design of d-PeT Phenylethynylated-Carbazole monoboronic acid fluorescent sensors for the selective detection of α-Hydroxyl Carboxylic acids and monosaccharides, *Journal of the American Chemical Society*, **2009**, *131*, 17452-17463.

38. S. Ji, J. Yang, Q. Yang, S. Liu, M. Chen, J. Zhao. Tuning the intramolecular charge transfer of alkynylpyrenes: Effect on photophysical properties and its application in design of OFF–ON fluorescent thiol probes, *Journal of Organic Chemistry*, **2009**, *74*, 4855-4865.

39. Nguyen Khoa Hien, Phan Tu Quy, Nguyen Tien Trung, Vo Vien, Dang Van Khanh, Nguyen Thi

Ai Nhung and Duong Tuan Quang. A dansyl-diethylenetriamine-thiourea conjugate as a fluorescent chemodosimete for Hg2+ ions in water media, *Chemistry Letters*, **2014**, *43*, 1034-1036.

40. Nguyen Khoa Hien, Nguyen Chi Bao, Nguyen Thi Ai Nhung, Nguyen Tien Trung, Pham Cam Nam, Tran Duong, Jong Seung Kim, and Duong Tuan Quang. A highly sensitive fluorescent chemosensor for simultaneous determination of Ag(I), Hg(II), and Cu(II) ions: Design, synthesis, characterization and application, *Dyes and Pigments*, **2015**, *116*, 89-96.

41. Doan Thanh Nhan, Nguyen Chi Bao, Nguyen Thi Ai Nhung, Dinh Quy Huong, Vo Vien, Nguyen Tien Trung, Nguyen Duc Cuong, Nguyen Khoa Hien and Duong Tuan Quang. A Benzothiazolium-derived colorimetric and fluorescent chemosensor for detection of Hg2+ ions, *Chemistry Letters*, **2017**, *46*(1), 135-138.

42. Nguyen Khoa Hien, Doan Thanh Nhan, Won Young Kim, Mai Van Bay, Pham Cam Nam, Dang Ung Van, In-Taek Lim, Jong Seung Kim, Duong Tuan Quang. Exceptional case of Kasha's rule: Emission from higher-lying singlet electron excited states into ground states in coumarin-based biothiol sensing, *Dyes and Pigments*, **2018**, *152*, 118-126.

43. Mai Van Bay, Nguyen Khoa Hien, Subin Son, Nguyen Duy Trinh, Nguyen Tien Trung, Pham Cam Nam, Jong Seung Kim, and Duong Tuan Quang. Hg2+-promoted spirolactam hydrolysis reaction: a design strategy for the highly selective sensing of Hg2+ over other metal ions in aqueous media, *Sensors*, **2019**, *19*(1), 128.

44. S. Sumiya, T. Sugii, Y. Shiraishi, T. Hirai. A benzoxadiazole–thiourea conjugate as a fluorescent chemodosimeter for Hg(II) in aqueous media, *Journal of Photochemistry Photobiology A: Chemistry,* **2011**, *219*(1), 154-158.

45. T. Keawwangchai, B. Wanno, N. Morakot, S. Keawwangchai. Optical chemosensors for Cu(II) ion based on BODIPY derivatives: an experimental and theoretical study, *Journal of Molecular Modeling*, **2013**, *19*(10), 4239-4249.

46. V. Ruangpornvisuti. A DFT study of molecular structures and tautomerizations of 2-benzoylpyridine semicarbazone and picolinaldehyde N-oxide thiosemicarbazone and their complexations with Ni(II), Cu(II), and Zn(II), *Structural Chemistry*, **2007**, *18*(6), 977-984.

47. H. F. Wang, S. P. Wu. Highly selective fluorescent sensors for mercury(II) ions and their applications in living cell imaging, *Tetrahedron*, **2013**, *69*(8), 1965-1969.

48. I. Ljubić and A. Sabljić. CASSCF/CASPT2 and TD-DFT study of valence and rydberg electronic transitions in fluorene, carbazole, dibenzofuran, and dibenzothiophene, *Journal of Physical Chemistry A*, **2011**, *115*(18), 4840-4850.

49. D. Jacquemin, A. Planchat, C. Adamo, and B. Mennucci. TD-DFT assessment of functionals for optical 0–0 transitions in solvated dyes, *Journal of Chemical Theory and Computation*, **2012**, *8*(7), 2359-2372.

50. C. A. Denis. The calculations of excited-state properties with time-dependent density functional theory, *Chemical Society Reviews*, **2013**, *42*, 845-856.

51. R. Carrasquilla and O. N. Bueno. Time dependent density functional study of the absorption and emission spectra of 1,3-benzoxazole and three substituted benzoxazoles, *Optica Pura y Aplicada*, **2012**, *45*(3), 287-297.

52. C. Bernini, L. Zani, M. Calamante, G. Reginato, A. Mordini, M. Taddei, R. Basosi, and A. Sinicropi. Excited state geometries and vertical emission energies of solvated dyes for DSSC: A PCM/TD-DFT benchmark study, *Journal of Chemical Theory and Computation*, **2014**, *10(9)*, 3925-3933.

53. R. Chidthong, S. Hannongbua, A. J.A. Aquino, P. Wolschann, H. Lischka. Excited state properties, fluorescence energies, and lifetime of a poly(fluorene-pyridine) copolymer, based on TD-DFT investigation, *Journal of Computational Chemistry*, **2007**, *28*, 1735-1742.

54. R. Chidthong, S. Hannongbua. Excited state properties, fluorescence energies, and lifetimes

of a poly(fluorene-phenylene), based on TD-DFT investigation, *Journal of Computational Chemistry*, **2010**, *31*, 1450-1457.

55. M. Savarese, A. Aliberti, I. De Santo, E. Battista, F. Causa, P. A. Netti, and N. Rega. Fluorescence lifetimes and quantum yields of rhodamine derivatives: New insights from theory and experiment, *Journal of Physical Chemistry A*, **2012**, *116*, 7491-7497.

56. Y. Li and T.-S. Chu. DFT/TDDFT study on the sensing mechanism of a fluorescent probe for hydrogen sulfide: Excited state intramolecular proton transfer coupled twisted intramolecular charge transfer, *Journal of Physical Chemistry A*, **2017**, *121*, 5245-5256.

57. S. Ghosh, K.V.S Girish and S. Ghosh. Evaluation of intramolecular charge transfer state of 4-N, N-dimethylamino cinnamaldehyde using time-dependent density functional theory, *Journal of Chemical Sciences*, **2013**, *125*(4), 933-938.

58. Nguyen Khoa Hien, Mai Van Bay, Phan Diem Tran, Nguyen Tan Khanh, Nguyen Dinh Luyen, Quan V. Vo, Dang Ung Van, Pham Cam Nam and Duong Tuan Quang. A coumarin derivative-Cu2+ complex-based fluorescent chemosensor for detection of biothiols, *RSC Advances*, **2020**, *10, 60*, 36265-36274.

59. P.-F. Loos, A. Scemama, and D. Jacquemin. The quest for highly accurate excitation energies: a computational perspective, *Journal of Physical Chemistry Letters*, **2020**, *11*, 2374-2383.

60. R. E. Stratmann, G. E. Scuseria, M. J. Frisch. An efficient implementation of time-dependent density-functional theory for the calculation of excitation energies of large molecules, *Journal of Chemical Physics*, **1998**, *109*(19), 8218-8224.

61. C. Hu, O. Sugino, K. Watanabe. Performance of Tamm-Dancoff approximation on nonadiabatic couplings by time-dependent density functional theory, *Journal of Chemical Physics*, **2014**, *140*(5), 054106.

62. Mai Van Bay, Nguyen Khoa Hien, Phan Thi Diem Tran, Nguyen Tran Kim Tuyen, Doan Thi Yen Oanh, Pham Cam Nam, Duong Tuan Quang. TD-DFT benchmark for UV-Vis spectra of coumarin derivatives, *Vietnam Journal of Chemistry*, **2021**, *59*(2), 203-210.

63. G. Singh, J. Sindhu, Manisha, V. Kumar, V. Sharma, S. K. Sharma, S. K. Mehta, M. H. Mahnashi, A. Umar and R. Kataria. Development of an off-on selective fluorescent sensor for the detection of Fe3+ ions based on Schiff base and its Hirshfeld surface and DFT studies, *Journal of Molecular Liquids*, **2019**, *296*, 111814.

64. Y. Xia, Z. Qi, Y. Sun, D. Cao, H. Ling, F. Yang, X. Ji. Theoretical investigation of a "turn-on" fluorescent sensor induced by complexation of mercury(II) ion**,** *Journal of Molecular Modeling*, **2014**, *20*, 2243.

65. S. S. Mallajosyula, H. Usha, A. Datta and S. K. Pati. Molecular modelling of a chemodosimeter for the selective detection of As(III) ion in water, *Journal of Chemical Sciences*, **2008**, *120*(6), 627-635.

https://doi.org/10.52111/qnjs.2022.16501

TẠP CHÍ KHOA HỌC
TRƯỜNG ĐẠI HỌC QUY NHƠN

Định tuyến động cho video streaming VBR thích nghi HTTP dựa trên mạng điều khiển bằng phần mềm

Phạm Hồng Thịnh*, Hồ Văn Phi

Khoa Kỹ thuật và Công nghệ, Trường Đại học Quy Nhơn, Việt Nam

Ngày nhận bài: 01/06/2022; Ngày nhận đăng: 25/07/2022; Ngày xuất bản: 28/10/2022

TÓM TẮT

Gần đây, truyền tải thích ứng HTTP (HAS) được xem là một trong những kỹ thuật quan trọng nhất trong ngành công nghiệp truyền phát thông tin, nó cho phép truyền tải nội dung đa phương tiện một cách hiệu quả qua internet. Ngoài ra, mạng điều khiển bằng phần mềm (SDN) đã nhận được sự quan tâm đáng kể dựa trên những tác động của nó đối với sự phát triển của dịch vụ Internet qua các lớp mạng. Trong công trình này, chúng tôi đã giới thiệu một phương pháp thích nghi chất lượng mới của video có tốc độ bit biến đổi (VBR), kết hợp kỹ thuật HAS với sự phân bổ đường dẫn động trong mạng SDN. Việc đánh giá thí nghiệm được thực hiện dựa trên các kịch bản khác nhau, chứng minh rằng giải pháp đề xuất tốt hơn phương pháp best-effort truyền thống cả về tốc độ bit lẫn độ mượt mà của luồng video.

Từ khóa: *Truyền tải thích ứng, Định tuyến động, HTTP, SDN.*

QUY NHON UNIVERSITY
JOURNAL OF SCIENCE

Dynamic routing for HTTP Adaptive VBR Video Streaming based on software defined networking

Pham Hong Thinh*, Ho Van Phi

Faculty of Engineering and Technology, Quy Nhon University, Vietnam

Received: 01/06/2022; Accepted: 25/07/2022; Published: 28/10/2022

ABSTRACT

Recently, HTTP Adaptive Streaming (HAS) has been considered as one of the most important technique in media streaming industry that allows multimedia content to be transmitted efficiently over the internet. In addition, Software-Defined Networking (SDN) has received significant attention based on its impacts on the development of Internet service across layers. In this work, we introduce a novel quality adaptation method of variable bitrate (VBR) that incoporates the HAS and dynamic path allocation in SDN networks. Experimental evaluation performed on different scenarios demonstrates that the proposed solution outperforms the traditional best-effort method on both overall bitrate and smothness of the stream.

Keywords: *Adaptive Streaming, Dynamic routing, HTTP, SDN.*

1. INTRODUCTION

In the recent years, video streaming over HTTP has occupied as a main video traffic source over the Internet, which account for roughly 82% of the total network traffic by 2022. Currently, adaptation methods on HTTP video streaming can be categorized into the buffer-based and throughput-based methods.[1-4] In our previous study,[5] we presented an adaptive video streaming approach over HTTP, but it only focuses on constant bitrate (CBR) videos in which segment bitrates are constant throughout the video. In this paper, in addition to the network bandwidth fluctuation, we need to take into account the bitrate fluctuation of variable bitrate (VBR) videos during playback time. In the state of the art, the methods have succeeded in bitrate adaptation for VBR videos,[3,4] which provides the best effort to acquire better Quality of Experience (QoE) in all contexts. However, the above HTTP-based adaptation methods only regard the client's behavior without concerning the transporting medium's characteristics such as the forwarding policy of the traditional switch network.

On the other hand, OpenFlow/Software Defined Networking (OF/SDN) has been quickly studied and implemented as one of the most important infrastructure for the future of network technology.[6] The authors of previous studies,[7,8] had pioneered in the area of Quality of Service (QoS) routing for scalable video coding video streaming over OF/SDN networks; nonetheless, they did not consider the adaptation problem at the client.

Furthermore, recent studies[9,10] have proposed SDN-based dynamic resource allocation and management architecture for HAS applications. However, only general adaptation

*Corresponding author.
Email: phamhongthinh@qnu.edu.vn

https://doi.org/10.52111/qnjs.2022.16503

mechanisms for CBR video streaming are considered in these studies.

In this paper, we present the HTTP-based bitrate adaptation combined with SDN-based dynamic routing mechanism to improve VBR video quality. Comparison of state-of-the-art studies with the proposed method is shown in Table 1.

Table 1. Comparison of related works with the proposed solution

Solution	Approach	Bitrate Adaptation	Adaptation Routing
[1 – 4]	HTTP	Yes	Conventional
[7 – 8]	SDN	No	QoS routing
[9 – 10]	Hybrid	Generally	Generally
Proposed	Hybrid	Specifically	Flexible rerouting

2. PROPOSED SOLUTIONS

2.1. SDN-assisted path selection optimization

As depicted in Figure 1, in our proposed controller architecture, we uniquely design a variety of functional modules as follows:

Topology Manager: Discovering the network topology.

Devices Manager: Supervising hosts connected to the forwarders.

Traffic Manager: Collecting statistical data from the forwarders.

Route Manager: Running routing algorithms to obtain desired network path, and installing flow rules onto the forwarders.

Messages Observer: Handling messages from application services.

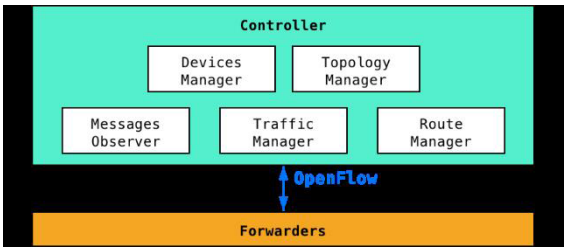

Figure 1. Proposed controller and interface

The controller communicates with the forwarders through an OpenFlow channel. The controller is implemented with two distinct mechanisms for reallocating the path in the SDN controller plane: Periodical Routing and Adaptive Routing. The idea of our routing mechanisms is to find out some paths with the least congestion or the sufficient bandwidth to accommodate requirements in increasing of bitrate adaptation. Definitely, a path with greater flow capacity is capable of delivering video segments of higher bitrate.

In Periodical Routing, the finest path is cyclically selected at a fixed interval as shown in the *Switching Stage* block and the *Steady Stage* block of Figure 2. After obtaining all paths' bandwidth, the controller keeps the least congested path for a short period until the procedure repeats. The total time for a procedure T is determined as:

$$T = (n + \alpha)t \quad (1)$$

with n being the number of paths, α is the steady parameter and t is the switching period.

In contrast, Adaptive Routing is only activated when there is a demand from the streaming service to SDN controller (Figure 2). There could be a monitoring process, which continuously inspect the currently installed path. Whenever the path's throughput do not meet the minimum requirement level BW^{th}, the controller intermediately find a new path to the controller without waiting for a routing request. After detecting a path with improved delivering capability, the controller installs new flow rules so that the video packet can travel along that path. All of the rerouting procedures are appeared transparent to the client.

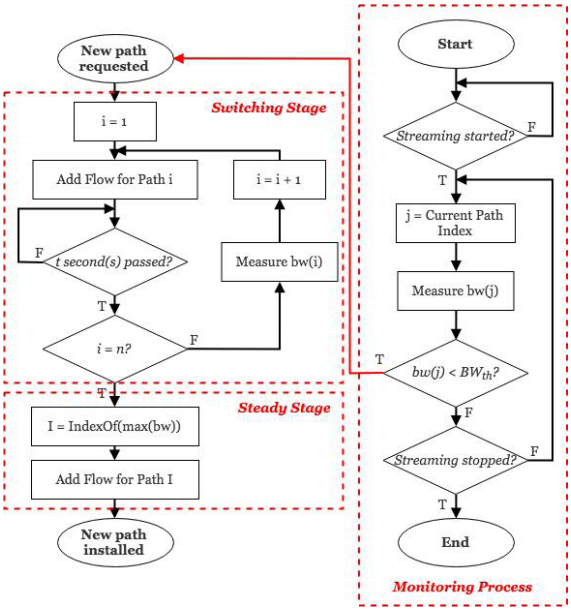

Figure 2. The Flowchart of optimum path selection

2.2. Variations of throughput and VBR bitrate

VBR video bitrate usually fluctuates significantly at some scene changes. An example of the bitrates a VBR video at different quality levels is shown in Figure 3. This property of VBR video makes the delivering the high video quality to clients a real challenge.

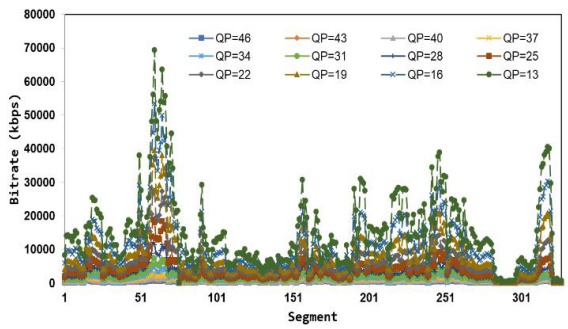

Figure 3. Bitrates of the video

To deal with the above issue, we introduce a *deviation* parameter $\boldsymbol{\delta}$, which was defined as in existing research:[11]

$$\delta = \frac{T_i}{R_i} - 1 \qquad (2)$$

where $\boldsymbol{T_i}$ is the throughput and $\boldsymbol{R_i}$ is the segment bitrate.

Specifically, we adopt the simple method presented in [2] to measure the estimated throughput.

$$T_i^e = (1-\mu)T_{i-1} \qquad (3)$$

where μ is the safety margin in the range of [0, 1].

The optimal bitrate for segment $i+1$ can be defined as:

$$R_{i+1}^{opt} = max\{R_i^{avg} | R_i^{avg} < T_i^e\} \qquad (4)$$

2.3. VBR adaptation algorithm

Using the flexible threshold, the segment buffer is splitted into four ranges ($B_{max} > B_{high} > B_{th} > B_{low} > 0$). Each range is corresponding to one of the cases: *switch-up, stable, switch-down* and *assisted switch-down*. Specifically, our method are shown in Algorithm 1.

Algorithm 1: VBR Adaptation Algorithm
Input: $R_i^{avg}, R_i^{opt}, T_i, R_i, B_i, \delta$
Output: I_{i+1}

```
//Switch-up case
if B_i ≥ B_high then
   if δ > δ_0 and R_i^avg < R_{i+1}^opt then
      I_{i+1} = I_i + 1;
   end if
end if
//Stable case
else if B_i ∈ [B_th, B_high) then
   I_{i+1} = I_i;
end if
//Switch-down case
else if B_i ∈ [B_low, B_th) then
   if δ < −δ_0 and (R_i^avg > R_{i+1}^opt or R_i > R_i^avg)
      I_{i+1} = I_i − 1;
   else
      I_{i+1} = I_i;
   end if
end if
//Assisted switch-down case
else if B_i < B_low then
   Request for a new path;
   for every representation v
      if R_v^avg == max{R_v^avg | R_v^avg < R_{i+1}^opt}
         I_{i+1} = v;
      end if
   end for
end if
```

The first case is the switch-up case in which the decision engine sends a signal to increase the video quality. However, the client only request a higher bitrate when a secure deviation value ($\delta > \delta_0$) is confirmed, and the average bitrate of the current representation still is not exceed the optimal bitrate ($R_i^{avg} < R_{i+1}^{opt}$).

https://doi.org/10.52111/qnjs.2022.16503

For the *switch-down* case ($B_{low} \le B_i < B_{th}$), the buffer threshold B_{th} is determined as follows:

$$B_{th} = B_{high} - \frac{1}{1+e^{-\delta}}(B_{high} - B_{low}) \quad (5)$$

Similar to the switch-up case, when a severely negative deviation value is detected ($\delta < -\delta_0$), and the current version is still higher than the optimal value ($R_i^{avg} > R_{i+1}^{opt}$); or the current scene is intensive i.e. consumes significant network resource ($R_i > R_i^{avg}$); the client reduce the quality level in the next segment.

We activate the *stable* case when the current buffer level is in [B_{th}, B_{high}). The range is considered to be safe, thus the client do not change the segment representation in the next request.

The last case, *assisted switch-down*, is indicated by the condition $B_i < B_{low}$. The decision engine will downgrade the video quality to an adequate bitrate while the controller proposes a new path with improved delivering capability as discussed in Section 2.1.

3. PERFORMANCE EVALUATION

3.1. Experiment setup

The test-bed setup in this paper is illustrated as Figure 4. The test video is a short animation movie named Elephants Dream, which is VBR-encoded at 12 versions with different quantization parameters (QPs). In the experiments, we set the QP values to be (13, 16, 19, 22, 25, 28, 31, 34, 37, 40, 43, 46). Each version is divided into two-second segments.

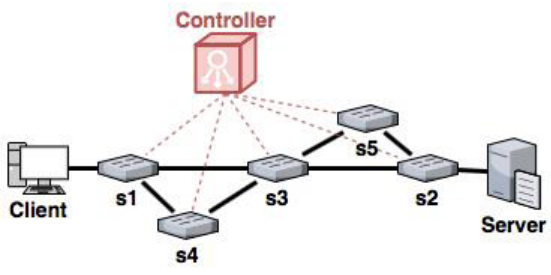

Figure 4. Experimental network topology.

For our proposed solution, the adaptation logic is adopted with the following parameters: B_{low} = 15*s*, B_{high} = 25*s*, B_{max} = 100*s* and δ_0 = 0.5. For simulation, we use real captured bandwidth when streaming online videos are sent through a Wi-Fi network as in Figure 5. The average latency is around 100ms, while the packet loss rate varies from 0 to 5%. The parameters in the equation (1) are fixed: n = 4, α = 1, t = [2*s*, 4*s*, 6*s*]. The threshold bandwidth of the monitoring process BW^{th} = 1.000kbps. In a Non-SDN network [2-5], data packets travel along the path such that minimizes the number of hops, i.e. through switch s2-s3-s1, as illustrated in Figure 4.

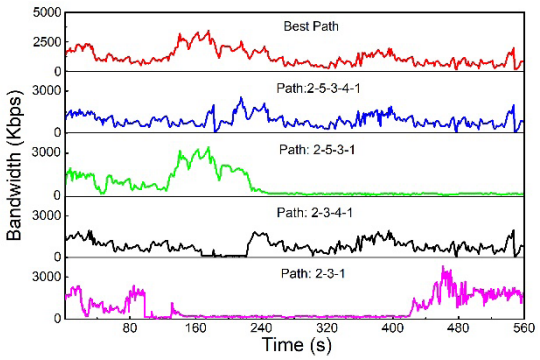

Figure 5. Experimental bandwidths

3.2. Experimental results and discussion

Results of all scenarios are shown in Figure 6, Figure 7 and Figure 8. Results for VBR adaptive video streaming over HTTP protocol without SDN are shown in Figure 6a. And the same results in different cases periodical routing with SDN which are given in Figure 6b, 6c, 6d. Resulting of the adaptive routing with and without monitoring process are shown in Figure 7a, 7b. Finally, comparative results of the quality assessment parameters are shown in Figure 8a, 8b. In order to evaluate more accurately for the above solutions, we can look at Table 2.

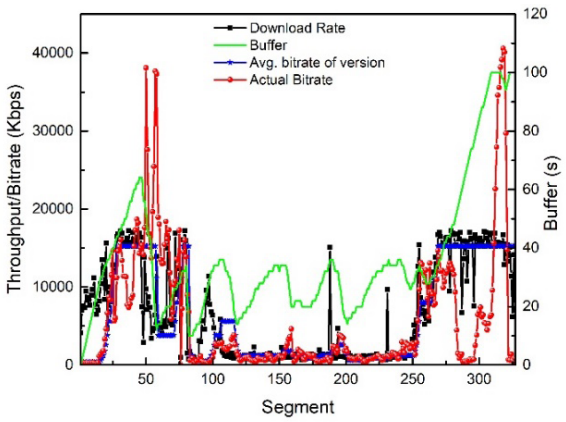

(a) Non-SDN

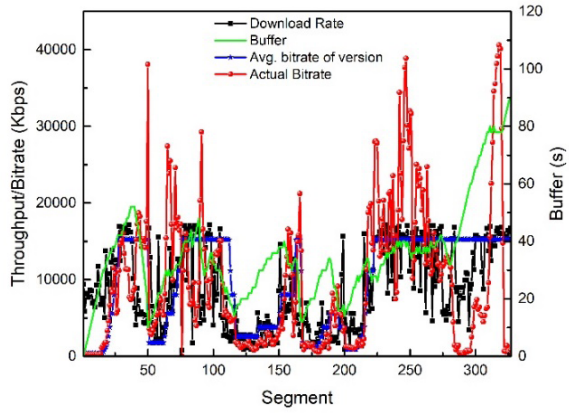

(b) t = 2s

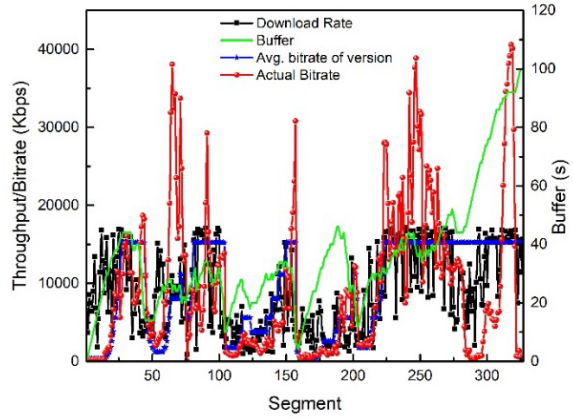

(c) t = 4s

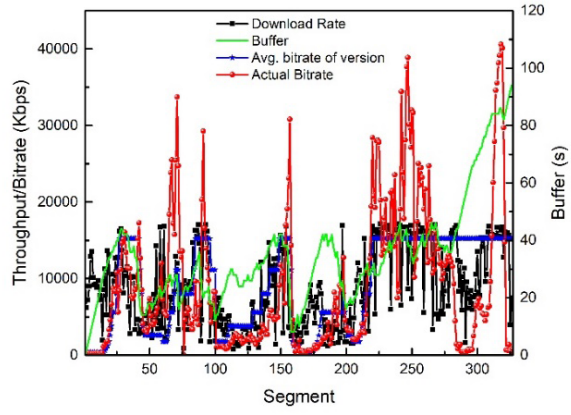

(d) t = 6s

Figure 6. Result of Non-SDN case (a) and Results of Periodical Routing with SDN case (b, c, d).

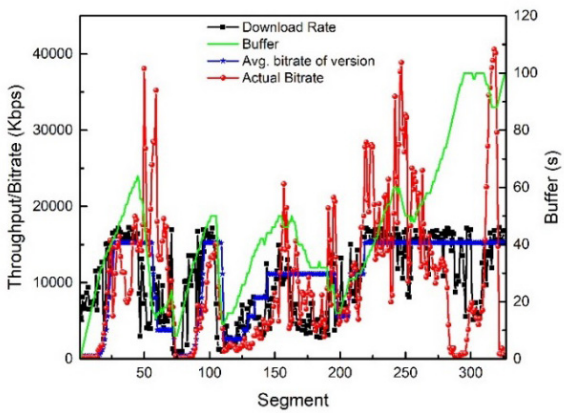

(a)

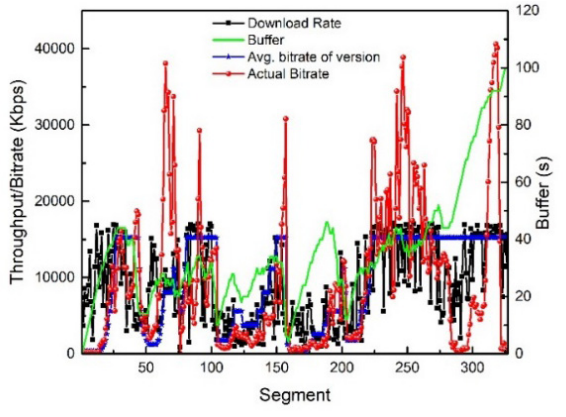

(b)

Figure 7. Results of Adaptive Routing without (a) and with (b) monitoring.

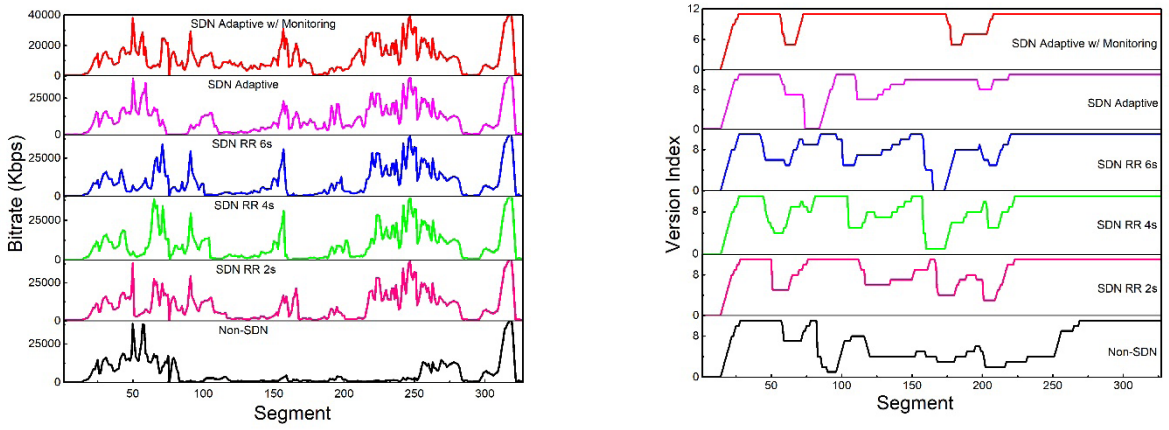

(a) (b)

Figure 8. Comparison of actual (a) and average (b) bitrate results.

Table 2. Statistics of different methods.

Statistics	Non-SDN	SDN-based Periodical Routing			SDN-based Adaptive Routing	
		t = 2s	t = 4s	t = 6s	Without Monitoring	With Monitoring
Average bitrate (kbps)	5767	9535	9250	8975	10425	11445
Proportion of version ≥ 8.000kbps (%)	35,8	61,5	58,4	57,8	72,8	81,0
Average buffer (s)	37	35	36	35	45	53
Proportion of buffer < 15s (%)	7,3	5,8	9,2	7,3	5,8	3,4
Number of version switch-downs	14	9	14	16	9	6
Controller Workload (%)	N/A	74,47	72,06	67,46	62,95	66,96

As shown in Table 2, the proposed methods can improve some QoE parameters for users. For the Periodical Routing case, the overall video quality is improved by exploiting the data transport capability of all the paths rather than of a single path as in Non-SDN networks.

Nonetheless, a higher switching period *t* results in a slight drop in the average bitrate. This method demands intensive computing capacity from the controller.

The method of Adaptive Routing with Monitoring delivers the paramount average bitrate of 11.445kbps, nearly twice the Non-SDN case (5.767kbps). In addition, the average buffer, the percentage of average bitrate is higher than 8.000kbps (sufficient for encoding Full HD videos) and the percentage of low buffer status are all exceptional. Its six version switch-downs also record the undermost number among all, providing a smoother video quality. To achieve such a performance, the controller has to operate more laboriously than that without path monitoring (66,96% compared to 62,95%).

In other words, the Adaptive Routing with Monitoring method is the most efficient method; the controller utilization is taken into account, the Adaptive Routing without Monitoring still provides acceptable performance in the video perceiving experience.

4. CONCLUSION

In this paper, we have presented a novel adaptive streaming method of VBR videos over HTTP

incoporating with the dynamic network path allocation over SDN. An extensive experiments has been conducted to study the performance of our algorithm with and without the aid of SDN. The experiments have showed that the proposed solution outperforms existing Non-SDN methods with up to 200% video bitrate improvement.

To develop this architecture in the future, we could broaden the network topology and add heterogeneous types of clients which share the same network resources. The optimized model should consider the client properties to provide traffic balance, stability and fairness among all devices.

Acknowledgment. *This research is conducted within the framework of science and technology projects at institutional level of Quy Nhon University under the project code T2022.761.17.*

REFERENCES

1. T. C. Truong, D. Q. Ho, J. W. Kang, A. T. Pham. Adaptive streaming of audiovisual content using MPEG DASH, *IEEE Transactions Consumer Electronics*, **2012**, *58*(1), 78–85.
2. T. C. Truong, H. T. Le, H. X. Nguyen, A. T. Pham, J. W. Kang, and Y. M. Ro. Adaptive video streaming over HTTP with dynamic resource estimation, *Journal of Communication and Networks*, **2013**, *15*(6), 635–644.
3. T. C. Truong, H. T. Le, A. T. Pham, and Y. M. Ro. An evaluation of bitrate adaptation methods for HTTP live streaming, *IEEE Journal on Selected Areas in Communications*, **2014**, *32*(4), 693–705.
4. T. Vu, H. T. Le, D. V. Nguyen, N. N. Pham, and T. C. Truong. Future buffer based adaptation for VBR video streaming over HTTP, *2015 IEEE 17th International Workshop on Multimedia Signal Processing (MMSP)*, **2015**, 1-5.
5. T. H. Pham, A. D. Nguyen, T. Nguyen, H. T. Truong, and N. N. Pham. Adaptation method for streaming of CBR video over HTTP based on software defined networking, *2017 International Conference on Advanced Technologies for Communications*, **2017**, *1*, 16–20,
6. N. McKeown et al., OpenFlow: Enabling innovation in campus networks, *ACM SIGCOMM Computer Communnication Review*, **2008,** *38*(2), 69-74.
7. H. E. Egilmez, S. Civanlar, and A. M. Tekalp. An optimization framework for QoS-enabled adaptive video streaming over openflow networks, *IEEE Transactions on Multimedia.*, **2013**, *15*(3), 710–715.
8. H. E. Egilmez and A. M. Tekalp. Distributed QoS architectures for multimedia streaming over software defined networks, *IEEE Transactions on Multimedia*, **2014**, *16*(6), 1597–1609.
9. A. Bentaleb, A. C. Begen, R. Zimmermann, and S. Harous. SDNHAS: An SDN-enabled architecture to optimize QoE in HTTP adaptive streaming, *IEEE Transactions on Multimedia*, **2017**, *19*(10), 2136–2151.
10. LIOTOU, Eirini, et al. QoE-SDN APP: A rate-guided QoE-aware SDN-APP for HTTP adaptive video streaming, *IEEE Journal on Selected Areas in Communications*, **2018**, *36*(3), 598-615.
11. H. N. Nguyen, T. Vu, H. T. Le, N. N. Pham, and T. C. Truong. Smooth quality adaptation method for VBR video streaming over HTTP, *2015 International Conference on Computing, Management and Telecommunications ComManTel 2015*, **2016**, 184–188.

TẠP CHÍ KHOA HỌC
TRƯỜNG ĐẠI HỌC QUY NHƠN

Bất đẳng thức kiểu Morrey cho các hàm có giá trị trung bình bằng 0

Nguyễn Văn Thành*, Nguyễn Hữu Thuần, Nguyễn Đặng Thanh Giang, Đỗ Phương Oanh, Nguyễn Thị Hà Tiên, Đoàn Khánh Duy

Khoa Toán và Thống kê, Trường Đại học Quy Nhơn, Việt Nam

Ngày nhận bài: 15/06/2022; Ngày nhận đăng: 01/09/2022; Ngày xuất bản: 28/10/2022

TÓM TẮT

Trong bài báo này, chúng tôi nghiên cứu một bất đẳng thức kiểu Morrey cho các hàm Sobolev có giá trị trung bình bằng 0. Hằng số được dẫn ra ở trong bài báo này là tốt hơn so với hằng số hiện có trong một số tài liệu. Sau đó, chúng tôi nghiên cứu sâu hơn về một ứng dụng của bất đẳng thức kiểu Morrey này đối với sự hội tụ yếu của dãy nghiệm của phương trình p-Laplace với điều kiện biên Neumann khi $p \to \infty$.

Từ khóa: *Không gian Sobolev, phương trình p-Laplace, bất đẳng thức kiểu Morrey.*

**Tác giả liên hệ chính.*
Email: nguyenvanthanh@qnu.edu.vn

https://doi.org/10.52111/qnjs.2022.16504

QUY NHON UNIVERSITY
JOURNAL OF SCIENCE

A note on Morrey-type inequality for functions of mean value zero

Van Thanh Nguyen*, Huu Thuan Nguyen, Dang Thanh Giang Nguyen
Phuong Oanh Do, Thi Ha Tien Nguyen, Khanh Duy Doan

Department of Mathematics and Statistics, Quy Nhon University, Vietnam

Received: 15/06/2022; Accepted: 01/09/2022; Published: 28/10/2022

ABSTRACT

In the present article, we study a Morrey-type inequality for Sobolev functions of mean value zero. The constant in our paper is smaller than the existing one in the literature. Then we study further an application of the Morrey-type inequality for the weak convergence of solutions to p-Laplace equations with a Neumann boundary condition as $p \to \infty$.

Key words: *Sobolev spaces, p-Laplace equations, Morrey-type inequality.*

1. INTRODUCTION

Let Ω be a bounded, smooth domain of $\mathbb{R}^n$. This paper is concerned with a Morrey-type inequality for Sobolev functions of mean value zero in Sobolev space $W^{1,p}(\Omega)$. As usual, Sobolev spaces consist of L^p functions whose weak derivatives belong to Lebesgue spaces L^p. These spaces provide one of the most useful settings for the analysis of partial differential equations. It is known that Sobolev spaces equipped with the norm

$$\|u\|_{W^{1,p}(\Omega)} = \|u\|_p + \|\nabla u\|_p$$

are Banach spaces, where $\|F\|_p := \left(\int_\Omega |F|^p \mathrm{d}x\right)^{1/p}$. For more details on Lebesgue and Sobolev spaces, we refer to the books.[1–4]

The well-known Morrey inequality in $\mathbb{R}^n$ (see, for example,[1,3,5,6]) states that if $p > n$ then for all $v \in W^{1,p}(\mathbb{R}^n)$ and all $x, y \in \mathbb{R}^n$

$$|v(x) - v(y)| \le \overline{C}_{p,n}|x-y|^{1-n/p}\left(\int_{\mathbb{R}^n} |\nabla v|^p \mathrm{d}x\right)^{\frac{1}{p}}, \tag{1}$$

where $\overline{C}_{p,n}$ is a positive constant depending only on p and n.

Now, let d_Ω denote the distance function to the boundary $\partial\Omega$, that is

$$d_\Omega(x) := \inf_{y\in\partial\Omega} |x-y| \ , \ x \in \overline{\Omega}.$$

Taking an arbitrary $y \in \partial\Omega$ in (1) one arrives at the following pointwise inequality, for all $(x, v) \in \overline{\Omega} \times W_0^{1,p}(\Omega)$,

$$|v(x)| \le \overline{C}_{p,n}\left(d_\Omega(x)\right)^{1-n/p} \|\nabla v\|_p, \tag{2}$$

where $\|\cdot\|_p$ stands for the standard norm of $L^p(\Omega)$. Passing to the maximum value in the left-hand side of (2) we arrive at the well-known Morrey-Sobolev inequality

$$\|v\|_\infty \le \overline{C}_{p,n,\Omega}\|\nabla v\|_p, \ \forall v \in W_0^{1,p}(\Omega), \tag{3}$$

where the constant $\overline{C}_{p,n,\Omega}$ depends only on p, n and Ω. The above inequality is devoted to Sobolev functions vanishing on the boundary and useful for studying partial differential equations involving a Dirichlet boundary condition. The counterpart for the Morrey-Sobolev inequality (3) for Sobolev functions of mean value zero can be written as

$$\|u\|_\infty \le C_{p,n,\Omega}\|\nabla u\|_p, \tag{4}$$

for all Sobolev function $u \in W^{1,p}(\Omega)$ of mean value zero, that is, it satisfies $\int\limits_\Omega u\mathrm{d}x = 0$.

In[7], the authors make use of this inequality (for a smooth and convex domain Ω) in studying limits as $p \to \infty$ of solutions to p-Laplace equations coupled with a Neumann boundary condition.

Such a constant $C_{p,n,\Omega}$ has been implicitly mentioned in[6] and explicitly given in[8] Lemma B.1.16

*Corresponding author.
Email: nguyenvanthanh@qnu.edu.vn

https://doi.org/10.52111/qnjs.2022.16504

(see also[9]). Finding a smaller constant for the Morrey-type inequality (4) is an interesting issue.

In this short paper, we provide a better estimate for the Morrey-type inequality (4) compared with the constant given in[8] Lemma B.1.16. Furthermore, its application in studying the weak convergence of solutions to p-Laplace equations with a Neumann boundary condition as $p \to \infty$ is also considered in detail.

The article is organized as follows. In section 2, we give a new constant C of the Morrey-type inequality (4) for Sobolev functions of mean value zero. Then, in section 3, we derive the key bound of the gradients of solutions to p-Laplace equations coupled with a Neumann boundary condition. As a consequence, we obtain the weak convergence of solutions in Sobolev spaces as $p \to \infty$.

2. MORREY-TYPE INEQUALITY FOR SOBOLEV FUNCTIONS OF MEAN VALUE ZERO

Theorem 1. *Let Ω be a Lipschitz and convex domain of $\mathbb{R}^n$ and $p > n$. Then every Sobolev function $u \in W^{1,p}(\Omega)$ of mean value zero, i.e. $\int_\Omega u\mathrm{d}x = 0$, obeys the following inequality*

$$\|u\|_{L^\infty} \leq \frac{d^{n+1-n/p}}{|\Omega|\,(n+1-n/p)}\omega_n^{1-1/p}\left(\frac{p-1}{p-n}\right)^{1-1/p}\|\nabla u\|_{L^p}, \tag{5}$$

where $\omega_n = \frac{2\pi^{n/2}}{\Gamma(n/2)}$ is the surface area of the unit sphere in $\mathbb{R}^n$, Γ is the gamma function, $|\Omega|$ is Lebesgue measure of Ω and $d = \mathrm{diam}(\Omega)$ is the diameter of Ω.

Proof. Set

$$C(d,n,p) := \frac{d^{n+1-n/p}}{n+1-n/p}\omega_n^{1-1/p}\left(\frac{p-1}{p-n}\right)^{1-1/p}.$$

We divide the proof into three steps.

Step 1. Fix any $x \in \mathbb{R}^n$. Let us prove that for any $\mathbb{R}^n$-valued measurable function $W \in L^\infty(\mathbb{R}^n;\mathbb{R}^n)$, we have for all $p > n$

$$\int\limits_{B(0,d)}\int\limits_0^1 |W(x+tz)||z|\mathrm{d}t\mathrm{d}z \leq C(d,n,p)\|W\|_{L^p(B(x,d))}, \tag{6}$$

where $B(y,d)$ is the Euclidean ball of radius d and center y in $\mathbb{R}^n$. To this aim, we make use of the change of variables in polar coordinates by the bijection $\Phi : B(0,d)\setminus\{0\} \longrightarrow (0,d]\times\partial B(0,1)$ defined as $\Phi(z) := (r,z') = \left(|z|, \frac{z}{|z|}\right)$. More precisely, one has

$$\int\limits_{B(0,d)} g(z)\mathrm{d}z = \int\limits_0^d r^{n-1}\int\limits_{\partial B(0,1)} g(rz')\mathrm{d}S(z')\mathrm{d}r. \tag{7}$$

Now applying (7) with $g(z) := \int\limits_0^1 |W(x+tz)||z|\mathrm{d}t$ on $B(0,d)$ for the second line below, and $g(z) := |W(x+z)||z|^{1-n}$ on $B(0,r)$ for the fifth, we arrive the following estimate

$$\begin{aligned}
&\int\limits_{B(0,d)}\int\limits_0^1 |W(x+tz)||z|\mathrm{d}t\mathrm{d}z\\
&= \int\limits_0^d r^{n-1}\int\limits_{\partial B(0,1)}\int\limits_0^1 |W(x+trz')|r\mathrm{d}t\mathrm{d}S(z')\mathrm{d}r\\
&= \int\limits_0^d r^{n-1}\int\limits_{\partial B(0,1)}\int\limits_0^r |W(x+\tau z')|\mathrm{d}\tau\mathrm{d}S(z')\mathrm{d}r \text{ (set } \tau = rt)\\
&= \int\limits_0^d r^{n-1}\int\limits_0^r \tau^{n-1}\int\limits_{\partial B(0,1)} |W(x+\tau z')|\tau^{1-n}\mathrm{d}S(z')\mathrm{d}\tau\mathrm{d}r\\
&= \int\limits_0^d r^{n-1}\int\limits_{B(0,r)} |W(x+z)||z|^{1-n}\mathrm{d}z\mathrm{d}r\\
&\leq \int\limits_0^d r^{n-1}\left(\int\limits_{B(0,r)} |W(x+z)|^p\mathrm{d}z\right)^{1/p}\left(\int\limits_{B(0,r)} |z|^{q(1-n)}\mathrm{d}z\right)^{1/q}\mathrm{d}r.
\end{aligned} \tag{8}$$

Here, for the last line, we used Hölder's inequality with $q = \frac{p}{p-1}$.

By $r \leq d$, observe that

$$\left(\int\limits_{B(0,r)} |W(x+z)|^p\mathrm{d}z\right)^{1/p} \leq \|W\|_{L^p(B(x,d))}.$$

On the other hand, using again (7) with $g(z) = |z|^{q(1-n)}$ we can compute explicitly

$$\begin{aligned}
\int\limits_{B(0,r)} |z|^{q(1-n)}\mathrm{d}z &= \int\limits_0^r \tau^{n-1}\int\limits_{\partial B(0,1)} \tau^{q(1-n)}\mathrm{d}S(z')\mathrm{d}\tau\\
&= \omega_n\int\limits_0^r \tau^{\frac{1-n}{p-1}}\mathrm{d}\tau\\
&= \frac{\omega_n}{\frac{1-n}{p-1}+1}r^{\frac{1-n}{p-1}+1} = \omega_n\frac{p-1}{p-n}r^{\frac{p-n}{p-1}}.
\end{aligned}$$

https://doi.org/10.52111/qnjs.2022.16504

It follows that

$$\begin{aligned}
&\int\limits_{B(0,d)}\int\limits_0^1 |W(x+tz)||z|\mathrm{d}t\mathrm{d}z\\
&\le \|W\|_{L^p(B(x,d))}\left(\omega_n\frac{p-1}{p-n}\right)^{1/q}\int\limits_0^d r^{n-1}\left(r^{\frac{p-n}{p-1}}\right)^{1/q}\mathrm{d}r\\
&= \|W\|_{L^p(B(x,d))}\left(\omega_n\frac{p-1}{p-n}\right)^{1/q}\int\limits_0^d r^{n-n/p}\mathrm{d}r\\
&= \|W\|_{L^p(B(x,d))}\left(\omega_n\frac{p-1}{p-n}\right)^{1-1/p}\frac{d^{n+1-n/p}}{n+1-n/p}.
\end{aligned}$$

Step 2. We are now in a position to show the assertion of Theorem 1 for the case of smooth function u. In this case, set

$$W(x) := \begin{cases}\nabla u(x) & \text{if } x\in\Omega\\ 0 & \text{if } x\in\mathbb{R}^n\setminus\Omega.\end{cases}$$

Since $\int_\Omega u(y)\mathrm{d}y = 0$, we get for any $x\in\Omega$

$$\begin{aligned}
u(x) &= \frac{1}{|\Omega|}\int_\Omega (u(x)-u(y))\,\mathrm{d}y\\
&= \frac{1}{|\Omega|}\int_\Omega\int_0^1 \langle\nabla u(x+t(y-x)),x-y\rangle\mathrm{d}t\mathrm{d}y\\
&\le \frac{1}{|\Omega|}\int_\Omega\int_0^1 |\nabla u(x+t(y-x))||x-y|\mathrm{d}t\mathrm{d}y\\
&\le \frac{1}{|\Omega|}\int\limits_{B(x,d)}\int\limits_0^1 |W(x+t(y-x))||x-y|\mathrm{d}t\mathrm{d}y\\
&= \frac{1}{|\Omega|}\int_{B(0,d)}\int_0^1 |W(x+tz)||z|\mathrm{d}t\mathrm{d}z.
\end{aligned}$$

Following Step 1, we obtain

$$\begin{aligned}
|u(x)| &\le \frac{C(d,n,p)}{|\Omega|}\|W\|_{L^p(B(x,d))}\\
&= \frac{C(d,n,p)}{|\Omega|}\|\nabla u\|_{L^p(\Omega)},
\end{aligned}$$

which completes the proof for smooth functions.

Step 3. For the general case, we make use a smooth approximation. Fix any $u\in W^{1,p}(\Omega)$ satisfying $\int_\Omega u\mathrm{d}x = 0$. Then there exists a sequence of smooth functions u_ε of mean value zero such that u_ε converges to u strongly in $L^m(\Omega)$ $(1\le m<\infty)$ and u_ε converges to u strongly in $W^{1,p}(\Omega)$ as $\varepsilon\to 0$. Passing to the limit as $\varepsilon\to 0$, from the inequality

$$\begin{aligned}
\|u_\varepsilon\|_{L^m(\Omega)} &\le |\Omega|^{\frac{1}{m}}\|u_\varepsilon\|_{L^\infty(\Omega)}\\
&\le |\Omega|^{\frac{1}{m}}\frac{C(d,n,p)}{|\Omega|}\|\nabla u_\varepsilon\|_{L^p(\Omega)}
\end{aligned}$$

we obtain

$$\|u\|_{L^m(\Omega)} \le |\Omega|^{\frac{1}{m}}\frac{C(d,n,p)}{|\Omega|}\|\nabla u\|_{L^p(\Omega)}.$$

Letting $m\to\infty$ we arrive to

$$\|u\|_{L^\infty(\Omega)} \le \frac{C(d,n,p)}{|\Omega|}\|\nabla u\|_{L^p(\Omega)},$$

which completes the proof. □

Remark 2. The above Morrey-type inequality is inspired by the estimate (B.1.3) of[8] p. 556 for smooth functions of mean value zero. However, it is worth noting that the inequality given in Theorem 1 is a little bit sharper than the one in[8] p. 556, where the constant is explicitly stated by

$$C = \frac{d^{n+1-n/p}}{|\Omega|n}\omega_n^{1-1/p}\left(\frac{p-1}{p-n}\right)^{1-1/p}.$$

3. APPLICATIONS

Give a Lipschitz and convex domain Ω of $\mathbb{R}^n$, we consider limits as $p\to\infty$ of solutions u_p to the p-Laplace problems coupled with a Neumann boundary condition

$$\begin{cases}-\operatorname{div}\left(|\nabla u(x)|^{p-2}\nabla u(x)\right) = f(x) & \text{in } \Omega\\ |\nabla u(x)|^{p-2}\dfrac{\partial u}{\partial\eta} = 0 & \text{on } \partial\Omega.\end{cases} \tag{9}$$

For a fixed $p>n$, the equation (9) has unique solution u_p of mean value zero, that is $\int_\Omega u_p\mathrm{d}x = 0$. This is a standard result in the field of calculus of variations and partial differential equations. In fact, consider the variational problem

$$\min_{u\in S_p}\left\{\int_\Omega \frac{|\nabla u|^p}{p}\,dx - \int_\Omega uf\,dx\right\}, \tag{10}$$

where $S_p := \left\{u\in W^{1,p}(\Omega) : \int_\Omega u\mathrm{d}x = 0\right\}$. The cost functional in (10) is lower semi-continuous, coercive and strictly convex on the non-empty convex set S_p. Therefore, there exists a unique minimizer u_p to (10), which is also a weak solution of problem (9), that is, it verifies

$$\int_\Omega |\nabla u_p|^{p-2}\nabla u_p.\nabla\phi\mathrm{d}x = \int_\Omega f\phi\mathrm{d}x,\ \forall\phi\in C^\infty(\overline{\Omega}). \tag{11}$$

In this section, we are interested in studying the behavior of solutions u_p as $p\to\infty$. More precisely, we will show that the sequence $\{u_p\}$ converges weakly in Sobolev spaces to a 1-Lipschitz function u_∞ as $p\to\infty$.

3.1. Bound of the gradients

Our aim is to prove that the L^p-norm of the gradients ∇u_p is bounded independently of all $p\ge n+1$.

Lemma 3. *Let u_p be a unique solution to (9) with $\int_\Omega u_p\mathrm{d}x = 0$. Then there exists a positive constant C independent of $p\ge n+1$ such that*

$$\|\nabla u_p\|_{L^p(\Omega)} \le C^{\frac{1}{p-1}} \text{ for all } p\ge n+1. \tag{12}$$

https://doi.org/10.52111/qnjs.2022.16504

Proof. As a consequence of Theorem 1, there exists a positive constant C_Ω independent of $p \geq n+1$ such that

$$\|u\|_{L^\infty(\Omega)} \leq C_\Omega \|\nabla u\|_{L^p(\Omega)} \tag{13}$$

for all $p \geq n+1$ and all Sobolev functions $u \in W^{1,p}(\Omega)$ of mean value zero, i.e., $\int_\Omega u\mathrm{d}x = 0$. In particular, applying for $u = u_p$ we get

$$\|u_p\|_{L^\infty(\Omega)} \leq C_\Omega \|\nabla u_p\|_{L^p(\Omega)}, \text{ for all } p \geq n+1. \tag{14}$$

On the other hand, using (11) with $\phi = u_p$, Hölder's inequality and (14), we obtain

$$\begin{aligned}\int_\Omega |\nabla u_p|^p \,\mathrm{d}x = \int_\Omega f u_p \,\mathrm{d}x &\leq \|f\|_{L^1(\Omega)} \|u_p\|_{L^\infty(\Omega)} \\ &\leq C_\Omega \|f\|_{L^1(\Omega)} \|\nabla u_p\|_{L^p(\Omega)}.\end{aligned}$$

It follows that

$$\|\nabla u_p\|_{L^p(\Omega)} \leq C^{\frac{1}{p-1}} \text{ for all } \ p \geq n+1,$$

with $C := C_\Omega \|f\|_{L^1(\Omega)}$ being independent of all $p \geq n+1$. □

3.2. Weak convergence

As a consequence of the previous bound of the gradients, we obtain uniform convergence of u_p and weak convergence of the gradients ∇u_p.

Proposition 4. *Let u_p be a unique solution to (9) with $\int_\Omega u_p \mathrm{d}x = 0$. Then, up to a subsequence, u_p converges uniformly on $\overline{\Omega}$ to a limit function $u_\infty \in W^{1,\infty}(\Omega)$ and $\nabla u_p \rightharpoonup \nabla u_\infty$ weakly in $L^m(\Omega)$ as $p \to \infty$ for any $1 \leq m < \infty$. Moreover, the limit function u_∞ is 1-Lipschitz, that is,*

$$|\nabla u_\infty(x)| \leq 1 \text{ for a.e. in } \Omega.$$

Proof. Fix any $m > n$. Let $p^* = \dfrac{p}{m}$. Using Hölder's inequality with p^* and q^* satisfying $\dfrac{1}{p^*} + \dfrac{1}{q^*} = 1$ and Lemma 3, we obtain

$$\begin{aligned}\|\nabla u_p\|_{L^m(\Omega)} &\left(\int_\Omega |\nabla u_p|^m \mathrm{d}x\right)^{\frac{1}{m}} \\ &\leq \left(\int_\Omega |\nabla u_p|^{mp^*} \mathrm{d}x\right)^{\frac{1}{mp^*}} \left(\int_\Omega \mathrm{d}x\right)^{\frac{1}{mq^*}} \\ &= \|\nabla u_p\|_{L^p(\Omega)} |\Omega|^{\frac{1}{m}-\frac{1}{p}} \\ &\leq |\Omega|^{\frac{1}{m}-\frac{1}{p}} C^{\frac{1}{p-1}}\end{aligned} \tag{15}$$

for all $p \geq \max\{n+1, m\}$, where C is a constant independent of p from Lemma 3. Observe that $|\Omega|^{\frac{1}{m}-\frac{1}{p}} C^{\frac{1}{p-1}} \to |\Omega|^{\frac{1}{m}}$ as $p \to \infty$. Hence, the sequence of gradients ∇u_p is bounded in $L^m(\Omega)$ and so is $\{u_p\}$ in $W^{1,m}(\Omega)$ (u_p is of mean value zero). Therefore, up to a subsequence, u_p converges uniformly on $\overline{\Omega}$ to a limit function u_∞ and $\nabla u_p \rightharpoonup \nabla u_\infty$ weakly in $L^m(\Omega)$ as $p \to \infty$. Obviously, the weak convergence of ∇u_p also holds true in $L^m(\Omega)$ for any $1 \leq m \leq n$. Finally, taking the limit as $p \to \infty$ in (15), we arrive to

$$\|\nabla u_\infty\|_{L^m(\Omega)} \leq |\Omega|^{\frac{1}{m}}. \tag{16}$$

Letting $m \to \infty$ we obtain $\|\nabla u_\infty\|_{L^\infty(\Omega)} \leq 1$, which completes the proof. □

REFERENCES

1. R. A. Adams and J.F. Fournier. *Sobolev spaces*, 2nd edition, Elsevier, Amsterdam, 2012.
2. H. Brezis. *Functional analysis, Sobolev spaces and partial differential equations*, Springer, New York, 2010.
3. G. Leoni. *A First Course in Sobolev Spaces*, 2nd edition, American Mathematical Society, Providence-Rhode Island, 2017.
4. W. Rudin. *Real and Complex Analysis*, 3rd edition, McGraw-Hill International Edition, Singapore, 1987.
5. G. Ercole and G. A. Pereira. An optimal pointwise Morrey-Sobolev inequality, *Journal of Mathematical Analysis and Applications*, **2020**, *489*, Art. 124143.
6. L. C. Evans. *Partial Differential Equations*, 2nd edition, American Mathematical Society, Providence-Rhode Island, 2010.
7. J. Mazon, J. Rossi, and J. Toledo. Mass transport problems obtained as limits of p-Laplacian type problems with spatial dependence, *Advances in Nonlinear Analysis*, **2014**, *3*(3), 133–140.
8. D. McDuff and D. Salamon. *J-holomorphic Curves and Symplectic Topology*, 2nd edition, American Mathematical Society, Providence-Rhode Island, 2012.
9. J. Weber. *Introduction to Sobolev Spaces*, Lecture Notes, Unicamp, 2018.

https://doi.org/10.52111/qnjs.2022.16504

TẠP CHÍ KHOA HỌC
TRƯỜNG ĐẠI HỌC QUY NHƠN

Vật liệu huỳnh quang không pha tạp phát xạ ánh sáng toàn phổ ứng dụng trong đèn LED trắng

Võ Thị Phú[1], Tạ Thị Minh Luôn[1], Đào Xuân Việt[2], Đặng Thị Tố Nữ[1], Nguyễn Minh Thông[2], Nguyễn Thị Tùng Loan[1], Lê Thị Thảo Viễn[1,*]

[1]Khoa Khoa học Tự nhiên, Trường Đại học Quy Nhơn, Việt Nam
[2]Viện đào tạo quốc tế về Khoa học Vật liệu (ITims), Trường Đại học Bách Khoa Hà Nội (HUST), Việt Nam

Ngày nhận bài: 20/06/2022; Ngày nhận đăng: 26/08/2022; Ngày xuất bản: 28/10/2022

TÓM TẮT

Vật liệu huỳnh quang không pha tạp Zn_2SnO_4 – SnO_2 kích thước cỡ vài µm đã được chế tạo thành công bằng phương pháp phản ứng pha rắn và nung ở nhiệt độ 1100 °C trong bài báo này. Vật liệu huỳnh quang này phát ánh sáng trắng tương tự như phổ ánh sáng Mặt Trời với bước sóng phát xạ trong khoảng từ 400 nm – 800 nm. Phổ phát xạ của mẫu được phân tích hàm Gauss cho các cực đại phát xạ ở các bước sóng khoảng 450 nm, 515 nm, 580 nm, 680 nm và 740 nm. Bài báo cũng giải thích nguồn gốc của các đỉnh phát xạ dựa trên lý thuyết phát xạ của các sai hỏng. Bên cạnh đó, bài báo cũng đề xuất sơ đồ giải thích nguồn gốc của các đỉnh phát xạ. Cuối cùng, khả năng ứng dụng của vật liệu trong chế tạo đèn LED chiếu ánh sáng trắng cũng được nghiên cứu trong bài báo này. Bột huỳnh quang sau khi chế tạo được phủ lên chip LED n-UV (310 nm) cho kết quả đèn LED phát ánh sáng trắng với chỉ số hoàn màu (CRI) bằng 95. Kết quả nghiên cứu cho thấy, vật liệu huỳnh quang Zn_2SnO_4 – SnO_2 có tiềm năng ứng dụng trong chế tạo LED trắng với giá thành rẻ và phương pháp đơn giản.

Từ khóa: *SnO_2 - Zn_2SnO_4, vật liệu huỳnh quang Zn_2SnO_4, vật liệu huỳnh quang toàn phổ.*

**Tác giả liên hệ chính.*
Email: lethithaovien@qnu.edu.vn

QUY NHON UNIVERSITY
JOURNAL OF SCIENCE

Full visible spectra of non-doped phosphor for WLED application

Vo Thi Phu[1], Ta Thi Minh Luon[1], Dao Xuan Viet[2], Dang Thi To Nu[1], Nguyen Minh Thong[2] and Nguyen Thi Tung Loan[1], Le Thi Thao Vien[1,*]

[1]Faculty of Natural Sciences, Quy Nhon university, Vietnam
[2]International Training Institute for Materials Science (ITIMS), Hanoi University of Science and Technology (HUST), Vietnam

Received: 20/06/2022; Accepted: 26/08/2022; Published: 28/10/2022

ABSTRACT

The Zn_2SnO_4 – SnO_2 micro-composite has been successfully fabricated by the solid reaction technique followed by calcination at 1100 °C. The obtained powder gives a full visible range from 400 nm to 800 nm. The PL spectra were fitted into five Gaussian peaks in the blue to the far-red region centered about 450 nm, 515 nm, 580 nm, 680 nm, and 740 nm. The origin of these emissions was discussed in detail. The proposed diagram for explaining the PL mechanism has been given in this paper. Further, the prepared phosphors have been coated onto the n-UV LED chip, which shows white light with a high CRI of 95. The result approves that Zn_2SnO_4 – SnO_2 micro composite is potential applications in white light-emitting diodes by a cheap and straightforward method.

Keywords: *SnO_2 - Zn_2SnO_4 powders, photoluminescence of Zn_2SnO_4, full visible spectra.*

1. INTRODUCTION

Light-emitting devices such as LEDs, WLED, and other optoelectronic devices based on wide band gap (WBG) semiconductor oxide materials are demonstrating their high efficiency and usefulness in recent years because of their regular physical, thermal and chemical properties.[1,2] One primary specification used in WLED and the lighting industry is the Color Rendering Index (CRI); thus, improving CRI for WLED is a significant and challenging task. One method commonly used to create WLED with high CRI is combining a semiconductor chip (blue or UV) with phosphors. Zinc oxide and tin dioxide are two of the most popular candidates for phosphors compared with others due to their simple synthesis and stable behavior.[3] Recently, many scientists have tried combining the two oxides ZnO and SnO_2 as a composite or compound to create new properties that suit their applications. For instance, the coupling may slow down the recombination of electron-hole pairs or improve performance in photocatalytic experiments.[4] Zn_2SnO_4-SnO_2 composite and other phases based on ZnO and SnO_2 have been produced by various methods and applied for many purposes. Abdessalem et al. synthesized the ZnO-SnO_2 nanocomposites using the sol-gel method and application on photocatalytic.[3] Precipitation – decomposition method was used to prepare the ZnO-SnO_2 composite by V.kuzhalosai et al.[5] Also, Eu^{3+} and Ca^{2+} co-doped Zn_2SnO_4 were synthesized by the hydrothermal method, and its emission was in the red band as reported by Krishna Sagar *et al.* in 2018.[6] In the same method, S. Dinesh et al. produced zinc stannate

*Corresponding authors.
Email: lethithaovien@qnu.edu.vn

https://doi.org/10.52111/qnjs.2022.16505

(Zn_2SnO_4) and applied it in photocatalytic and antibacterial activity.[7] In addition, other shapes of Zn_2SnO_4, like nanobelts and nanorings, have been synthesized using thermal evaporation or simple chemical vapor deposition methods.[8,9] High energy milling method, electrospinning, and combustion method were also applied in the synthesis of ZnO-SnO_2 composite and Zn_2SnO_4.[10-12] Zn_2SnO_4 has a wide band gap (3.6 eV) with good potential for phosphor applications. However, only a small number of reports focus on the optical properties of these host materials.[13] Furthermore, the application of these phosphors on White LED has not been much regarded.

Normally, a phosphor consists of a host lattice and doping ions such as rare-earth ions. Specifically, Eu^{3+} and Ca^{2+} co-doped Zn_2SnO_4 was synthesized using a hydrothermal method and its emission was in the red band as reported by Krishna Sagar et al. in 2018.[12] In 2016, Dimitrievska et al. reported that Eu^{3+} doped Zn_2SnO_4, generated by a solid-state reaction method, showed several emission bands, including narrow bands of magnetic dipole emission at 595 nm and electric dipole emission at 615 nm.[13] However, phosphors based on rare-earth are not cheap and unsafe.

In this paper, the undoped phosphor SnO_2 - Zn_2SnO_4 has been successfully produced by a simple method – solid reaction. The PL spectra show a full visible range like the sunlight spectrum from 400 nm to 800 nm. When the prepared phosphor is coated onto the surface of an n-UV LED chip, the device shows warm white color with a CRI of 95. Other parameters related to the quality of WLED have been calculated. Further, the origin of PL emission and the proposed diagram for explaining the PL mechanism have been given in this research.

2. EXPERIMENTIAL

The sample synthesized by solid reaction in this work follows the below process:

i. Pure ZnO (99.99%, Sigma-Aldrich) and SnO_2 (99.99%, Sigma-Aldrich) powders were used as starting materials. The starting materials were weighed according to the stoichiometric weight ratio of 1:1 of ZnO: SnO_2 (5g ZnO and 5g SnO_2). After that, the mixture is grounded coarsely for 1 hour and further grounded by high-energy planetary ball milling (Restch PM400) at a speed of 200 rpm for 60 hours. The next step is putting the mixture into a furnace and annealing at 1100 °C.

ii. The powder was coated on to UV LED Chip.

iii. The parameters of WLED will be measured and compared with commercial products.

The prepared powders have been analyzed by X-ray diffraction (XRD) using CuKa radiation (Bruker D8 Advance) in the 2θ range of 100 – 800. The surface morphology and average size of particles are determined by ultra-high resolution scanning Electron Microscopy (SEM – Jeol JSM-7600F). In addition, the elemental analysis of the sample is studied by energy dispersive spectrometry (EDS) carried out on the Jeol JSM-7600F detector on the SEM over the range 0-20KeV. Horiba Jobin Yvon equipment was taken to investigate the luminescence characteristics at room temperature. Further, the i-DR S320A Desktop Dispensing system was used to cover the phosphor on to UV LED Chip, and the chromaticity coordinates of the phosphors were calculated by a LED testing system (Gamma Scientific).

3. RESULTS AND DISCUSSION

3.1. X-ray diffraction

Figure 1 illustrates X-ray diffraction (XRD) patterns of Zn_2SnO_4 – SnO_2 composites prepared by solid reaction and annealed at different temperatures: unanealing (a); 500 °C (b); 900 °C (c); 1000 °C (d); 1100 °C (e) and 1200 °C (f) for 2 hours in air. As shown in Figure 1, the XRD peaks of the sample annealed at 1100 °C show the highest intensity and sharpest summit. All the diffraction peaks are indexed to the cubic phase Zn_2SnO_4 (JCPDS card no. 00-024-1470, space group Fd-3m (227) and cell parameters a = b = c = 8.657 Å[14] (Figure 4a) and Tetragonal phase SnO_2 (JCPDS card no. 00-021-1250, space group

P42/mm (136) and cell constants a = b = 4.738 Å and c = 3.188 Å[15] (Figure 4b). Furthermore, as can be seen in Figure 1f, the peak (101) of the SnO_2 phase begins to separate into two peaks and form a new peak (311) of Zn_2SnO_4 at 900 °C. The same phenomenon happens at the (422) peak of Zn_2SnO_4 at 1200 °C. The formation of the second phase may cause a decrease in the photoluminescence intensity of the sample, so we chose the optimal temperature of 1100 °C in this work.

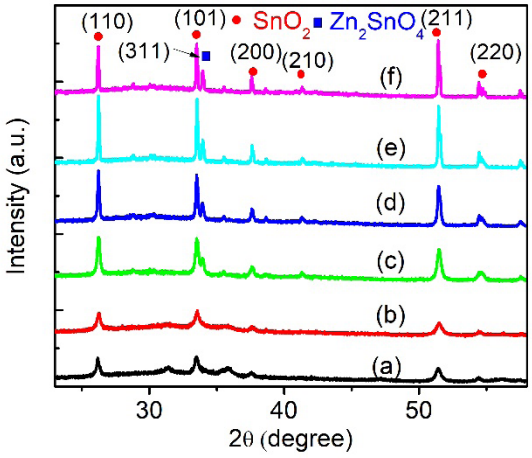

Figure 1. XRD patterns of SnO_2-Zn_2SnO_4 ample unnealed (a) and annealed at different temperature of 500 C (b); 900 °C (c); 1000 °C (d); 1100 °C (e) and 1200 °C (f).

3.2. Phosphor morphology

In order to determine phosphor morphology and size of the sample, a typical scanning electron microscope (SEM) has been carried out by ultra-high resolution scanning Electron Microscopy (SEM – Jeol JSM-7600F). Figure 2 illustrates a typical scanning electron microscope image of the prepared Zn_2SnO_4-SnO_2 at different annealing temperature un-calcinated (a); 500°C (b); 900 °C (c); 1000 °C; 1100 °C (d) and 1200 °C (f). Both particle shape and size are affected by changing calcination temperature dramatically. The powder particles of the unannealed sample (a) have an average size of about 10 nm with irregular spherical particles. When the annealing temperature increases to 1000 °C, the sample particle sizes are bigger and spherical morphology with particle bounds can be observed clearly. This result is well-matched with the XRD analysis mentioned above. The average particle size of the sample at 1100 °C is about 10 nm to 1µm, which is a suitable size for LED applications. However, under the high of temperature 1200 °C, a re-crystallization or particles cluster together to form massive or tiny particles.

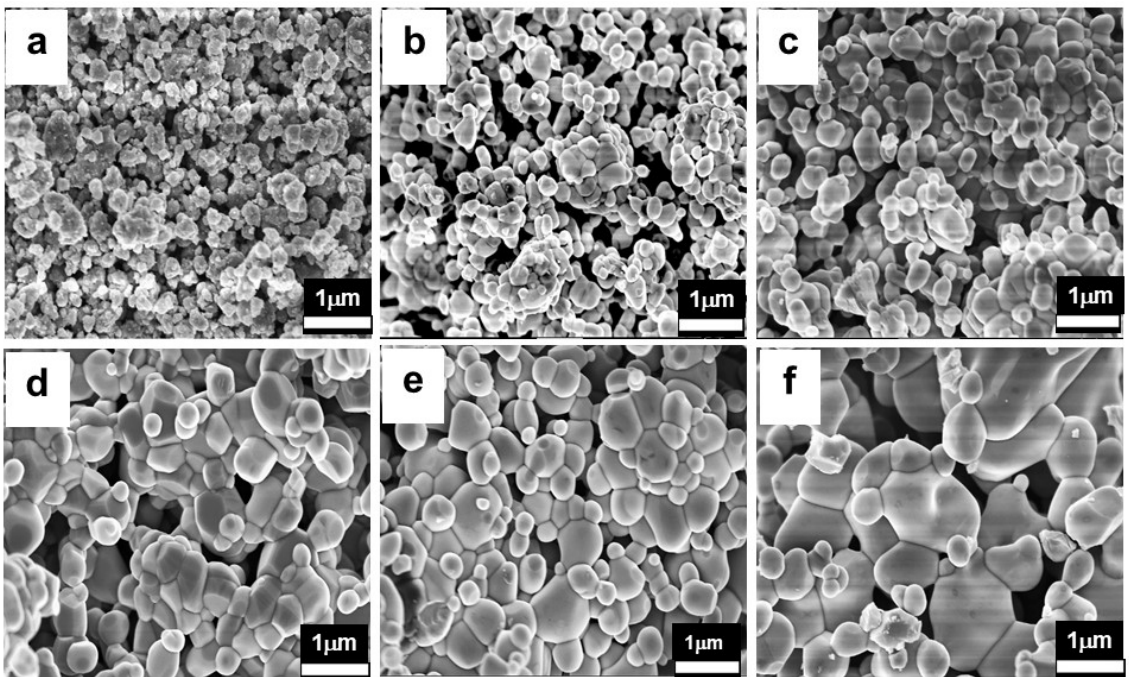

Figure 2. FESEM images of SnO_2 - Zn_2SnO_4 sample: unnealed (a) and annealed at different temperature of 500 °C (b); 900 °C (c); 1000 °C (d); 1100 °C (e) and 1200 °C (f).

https://doi.org/10.52111/qnjs.2022.16505

3.3. Optical properties

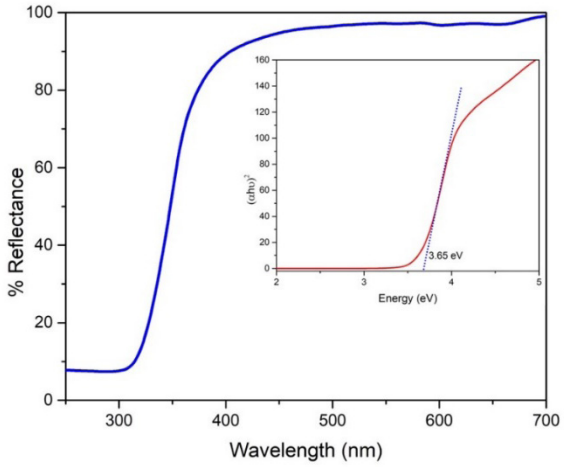

Figure 3. UV-Vis spectra of the sample Zn_2SnO_4 - SnO_2 at calcination temperature of 1100 °C.

The UV – vis spectroscopy was used to examine optical properties and estimate the band gap Eg of the prepared sample as shown in Figure 3. As seen from the Figure 3, there is a significant rise in strong light reflection around over 310 nm and the most substantial absorption at about 310 nm, which can be assigned to intrinsic band gap absorption. The K-M formula[16] has been used to estimate the optical absorption band gap of the prepared sample as shown in the inset of the Figure. The estimated value of the bandgap Eg is about 3.65 eV, which is slightly higher than the band gap value of bulk Zn_2SnO_4 (3.6 eV), but it is just under in comparison with the SnO_2 band gap (3.7 eV) reported by a previous report.[17] The two-band gaps may correspond to 3.6 eV of Zn_2SnO_4 and 3.7 eV of SnO_2 phosphor. Furthermore, based on the XRD estimated result, the two phases, Zn_2SnO_4 and SnO_2, are nearly identical.

Figure 4 illustrates the photoluminescence (PL) spectrum of the Zn_2SnO_4 – SnO_2 sample annealed with different temperature: un-calcinated (a); 500 °C (b); 900 °C (c); 1000 °C (d); 1100 °C (e) and 1200 °C (f). The spectra was recorded with the excitation wavelength 310 nm at room temperature by Nanolog - Horiba Jobin Yvon equipment. Overall, PL spectra of all samples anealed over 500 °C shows a broad visible band from 400 nm to 900 nm and nearly covers the full visible range blue – far-red emission. However, there are different intensities among them. It is observed that the PL intensity of the sample increases when the calcination temperature increases, and the highest intensity belongs to the sample with an annealing temperature of 1100 °C (the inset of Figure 4). This result is suitable with XRD and SEM results. In order to clear the origin of PL peaks emission, the broadband emission has been fitted by Gaussian function as given in Figure 4b, which indicates that the PL spectrum was fitted into five Gaussian peaks when the Gaussian was applied. Overall, there is no direct recombination process of a hole in the valence band to an electron in the conductor band because all five peaks' emission is smaller than the band gap of the prepared sample (3.65 eV). The first peak is in the blue region centered around 450 nm. Based on the calculated band gap of 3.65 eV, it is well-known from previous reports[6, 11, 18, 19] that the band gap of bulk SnO_2 and Zn_2SnO_4 are around 3.87eV and 3.6 eV, respectively. So the peak emission at 450 nm is not due to the band-to-band gap emission of neither SnO_2 nor Zn_2SnO_4 phosphor. According to a former investigation,[1, 7] the PL mechanisms have always been ascribed to other luminescent centers, such as oxygen vacancies and residual strain during the growth process. Hence, this work supports that the blue in the PL spectra can be attributed to oxygen vacancy defects in the SnO_2. The second band emission centered around 515 nm. This peak's origin was also discussed in Fu et al. research[20] and Baruah et al. report.[21] According to them, the similar broad green emission centered at 520 nm in Zn_2SnO_4 under Xenon lamp excitation was caused by oxygen vacancy in Zn_2SnO_4 during the growth process. Moreover, Smilja et al. said that the 546 nm emission in ZnO/SnO_2 spectra were that green emission implicates surface defects, as well as the defects just below the crystalline surface.[22] So we suggest that the emission centered at 515 nm observed in PL spectra relates to oxygen

vacancies in Zn_2SnO_4. Next, the third peak is in the yellow-orange region centered at 580 nm, which may attribute to SnO_2 defects such as Zn interstitials (Z_{ni}) or oxygen interstitials (O_i).[8] The two final peaks are red and far-red, centered at 680 nm and 740 nm, which have not been observed and discussed in previous reports. We suggest that they may relate to surface defects of the obtained sample,[23] but the exact type and number of defect states depend on the method and parameters changing in the process.

Regarding the origin of the red emission band, Fu et al.[20] approved that stoichiometry Zn/Sn played a role in this emission. Furthermore, the red emission centered at 630 nm in SnO_2 PL spectra reported by Smilja et al.[22] was considered related to deep–level defects within the gap of SnO_2, associated with oxygen vacancies and Sn interstitial formed during the synthesis procedure. The origin of this emission is still unclear and needs another measurement. Nevertheless, we agree with Chih-Hsien Cheng et al.[23] that the origin of the infrared 700 nm in his research is related to the transition states between neutral and ionized oxygen. In addition, from what is discussed above and what is shown in PL spectra, we propose a diagram to explain the PL mechanism as shown in Figure 5. We believe defects formed during the calcination process play as energy states within the band gap. Hole traps are states that exit just over the valance band and fill holes, whereas electron traps are formed just under the conductor band and fill with electrons. The PL mechanism can be proposed as the following explanation. First, electrons from the valance band absorb excited energy as large as band gap energy and move to the conductor band to become excited electrons. Because the electron traps are just under the conductor band, excited electrons are trapped in electron traps easily without light-emitting. After that, these electrons release to lower energy states and depend on the gap between the two states that emit blue, green, red, or infrared.[24]

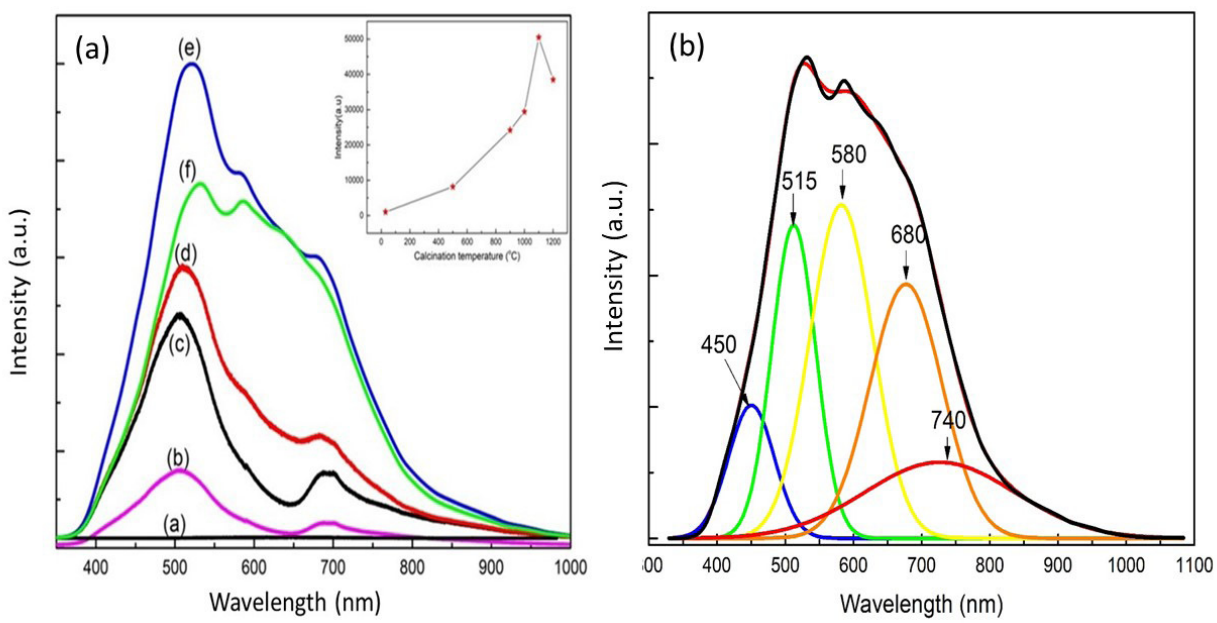

Figure 4. PL spectra of the Zn_2SnO_4 – SnO_2 phosphor annealed at different calcination temperatures (a) and PL of the sample annealed at 1100 °C fitted by Gaussian peak (b). The inset of the Figure a is the relative intensity of the Zn_2SnO_4 – SnO_2 phosphor annealed at different calcination temperatures.

https://doi.org/10.52111/qnjs.2022.16505

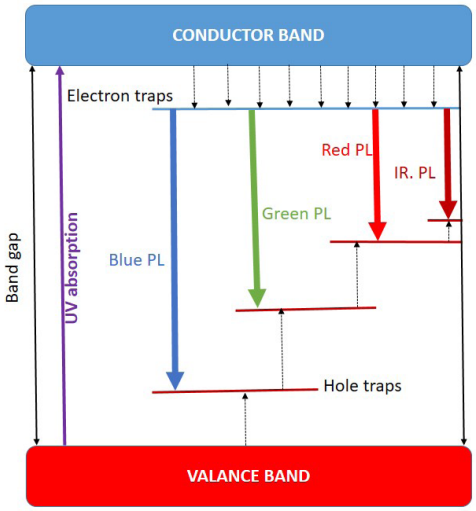

Figure 5. Proposed energy band diagram for expalination PL machanism of Zn_2SnO_4 – SnO_2 sample showing the defect states and the transitions between the states.

3.4. Electroluminescence properties of Zn_2SnO_4 – SnO_2 micro composite

In order to explore the potential application of Zn_2SnO_4 – SnO_2 powder annealed at 1100 °C, white emission LED is assembled by coating 5 mg of Zn_2SnO_4 – SnO_2 phosphor on an LED chip 310 nm by the i-DR S320A Desktop Dispensing system. The image of the white LED device underdrive current of 0.2004 A and a voltage of 8.029 V during the process, and its CIE chromaticity coordination is displayed in Figure 6. The Zn_2SnO_4 – SnO_2 powder annealed at 1100 °C was covered on. The device was then introduced into an integrating sphere system to calculate parameters related to the quality of WLED as shown in Table 1. Figure 6 demonstates that the CIE coordinates and CRI of White LED are (0.3755; 0.4173) and 95, respectively, which are very close to natural light. The colour temperature is 4273 K, which is energizing and most closely mimics natural daylight; it helps with tasks requiring focused attention, such as reading, computer work, carpentry, and drawing. These results demonstrate that Zn_2SnO_4 – SnO_2 micro composite phosphor shows a potential application in producing high both CRI and LER White LED.

Table 1. The WLED parameters (D_{uv}; Correlated colour temperature (CCT); Colour rendering index (CRI); Luminous efficacy of radiation (LER); R_9 and CIE coordinates(x,y)) of LED covered phosphor.

Sample	LED parameters						
	D_{uv}	CCT (K)	CRI	LER (lm/W)	R_9	x	y
Zn_2SnO_4 – SnO_2	0.0194	4273	95	85	94	0.3755	0.4173

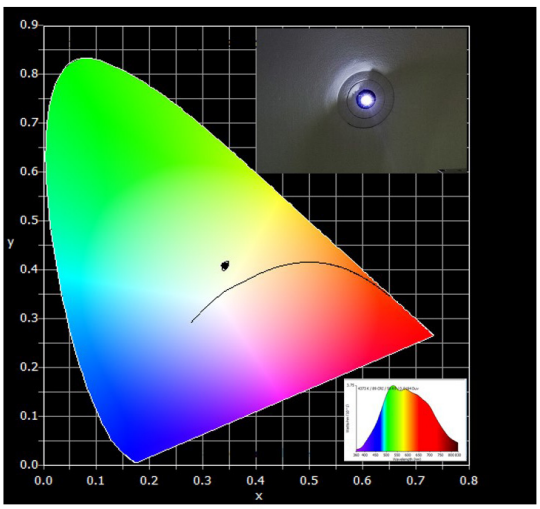

Figure 6. CIE 2015-10° xy color chromaticity coordinates of the spectral emission from UV LED chip coated by prepared phosphor. The insets is the electroluminescence spectrum and the image captured by a digital camera of the white-emitting LED.

4. CONCLUSION

The Zn_2SnO_4 – SnO_2 micro composite was produced successfully by solid-state reaction followed by calcination at 1100 °C in air. The crystalline structure of samples was mixed of the cubic phase Zn_2SnO_4 (JCPDS card no. 00-024-1470, space group Fd-3m (227) and cell parameters a = b = c= 8.657 Å) and Tetragonal phase SnO_2 (JCPDS card no. 00-021-1250, space group P42/mm (136) and cell constants a = b = 4.738 Å and c = 3.188 Å. PL spectra of all samples show a broad visible band from 400 to 900 nm, nearly covering the full visible range of blue–far–red emission with peaks at around 450, 515, 580, 680, and 740 nm. A PL mechanism diagram has been proposed to explain the emission's origin. The LED chip 310 was used to cover obtained phosphor, getting a white LED. The CIE coordinates and CRI of White LED are (0.3755:0.4173) and 95, respectively. These results demonstrate that Zn_2SnO_4 – SnO_2 micro composite phosphor is potentially applicable in producing high CRI White LED.

Acknowledgement. *This research is conducted within the framework of science and technology projects at institutional level of Quy Nhon University under the project code T2022.747.03.*

REFERENCES

1. Y. N. Ahn, K. D. Kim, G. Anoop, G. S. Kim & J. SooYoo1. Design of highly efficient phosphor converted white light-emitting diodes with color rendering indices (R_1 − R_{15}) ≥ 95 for artificial lighting, *Scientific Reports,* **2019,** *9,* 16848813.
2. J. Shi, J. Zhang, L. Yang, M. Qu, D. C. Qi. Wide bandgap oxide semiconductors: from materials physics to optoelectronic devices, *Advanced Materials*, **2021**, *33*, 2006230.
3. A. Hamrouni, N. Moussa, F. Parrino, A. D. Paola, A. Houas, and L. Palmisano. Sol-gel synthesis and photocatalytic activity of ZnO-SnO_2 nanocomposites, *Journal of Molecular Catalysis A: Chemical*, **2014**, *390,* 133–141.
4. K. A. Omar, B. I. Meena, and S. A. Muhammed. Study on the activity of ZnO-SnO_2 nanocomposite against bacteria and fungi, *Physicochemical Problems of Mineral Processing*, **2016**, *52*(2), 754–766.
5. V. Kuzhalosai, B. Subash, A. Senthilraja, P. Dhatshanamurthi, and M. Shanthi. Synthesis, characterization and photocatalytic properties of SnO_2-ZnO composite under UV-A light, *Spectrochimica Acta Part A: Molecular and Biomolecular Spectroscopy*, **2013**, *115*, 876–882.
6. K. Sagar, C. Kuttykrishnan, and J. B. Mohammed. Hydrothermal growth of Zn_2SnO_4: Eu , Ca for red emission, *Journal of Luminescence*, **2018**, *33*, 675-6804.
7. S. Dinesh, S. Barathan, V. K. Premkumar, G. Sivakumar, and N. Anandan. Hydrothermal synthesis of zinc stannate (Zn_2SnO_4) nanoparticles and its application towards photocatalytic and antibacterial activity, *Journal of Materials Science: Materials in Electronics*, **2016**, *27*(9), 9668–9675.
8. Q. R. Hu. Synthesis and photoluminescence of Zn_2SnO_4 nanowires, *Journal of Alloys and Compounds,* **2009**, *484*(1–2), 25–27.
9. Q. Li. Preparation of Zn_2SnO_4/SnO_2: Mn_2O_3 microbox composite materials with enhanced lithium-storage properties, *ChemElectroChem*, **2017**, *4*(6), 1334–1340.
10. L. Ma, S. Y. Ma, H. Kang, X. F. Shen, T. T. Wang, X. H. Jiang, Q. Chen. Preparation of Ag-doped ZnO-SnO_2 hollow nanofibers with an enhanced ethanol sensing performance by electrospinning, *Materials Letters*, **2017**, *209*, 188–192.
11. L. C. Nehru and C. Sanjeeviraja. Processing Research Controllable growth of Zn_2SnO_4 nanostructures by urea assisted microwave-assisted solution combustion process, *ChemElectroChem,* **2013**, *14*(5), 606–609.
12. L. Manzato, D. M. Trichês, S. Michielon de Souza, and M. Falcão de Oliveira. Synthesis of nanostructured SnO and SnO_2 by high-energy milling of Sn powder with stearic acid, *Journal of Materials Research*, **2013**, *29*(1), 84–89.

13. L. T. T. Vien, N. Tu, D. X. Viet, D. D. Anh, D. H. Nguyen and P. T. Huy, Mn^{2+}-doped Zn_2SnO_4 green phosphor for WLED applications, *Journal of Luminescence*, **2020**, *227*(117522), 1-9.

14. M. Asemi, M. Ghanaatshoar. Boosting the photovoltaic performance of Zn_2SnO_4-based dye-sensitized solar cells by Si doping into Zn_2SnO_4, *Journal of the Amercan ceramic society*, **2017**, *100*, 5584-5592.

15. Y. Gao, M. Hou, Z. Shao, C. Zhang, X. Qin and B. Yi. Highly effective oxygen reduction activity and durability of antimonydoped tin oxide modified PtPd/C electrocatalysts, *RSC Advances,* **2016**, *5*, 1-8.

16. J. Tauc. Optical properties and electronic structure of amorphous Ge and Si, *Materials Research Bulletin*, **1968**, *3*(1), 37–46.

17. T. Jia, J. Zhao, F. Fu, Z. Deng, W. Wang, Z. Fu, F. Meng. Synthesis, characterization, and photocatalytic activity of Zn-doped SnO_2/Zn_2SnO_4 coupled nanocomposites, *International Journal of Photoenergy*, **2014**, 1–7.

18. P. Wu. Correlation between photoluminescence and oxygen vacancies in In_2O_3, SnO_2 and ZnO metal oxide nanostructures, *Journal of Physics: Conference Series*, **2009**, *188*(1), 12054.

19. A. Gaber, M. A. Abdel- Rahim, A. Y. Abdel-Latief, and M. N. Abdel-Salam. Influence of calcination temperature on the structure and porosity of nanocrystalline SnO_2 synthesized by a conventional precipitation method, *International Journal of Electrochemical Science*, **2014**, *9*(1*)*, 81–95.

20. N. Duy, T. Luu, M. Quynh, L. V. Vu, and N. Ngoc. Phase transformation and photoluminescence of undoped and Eu^{3+} -doped zinc stannate (Zn_2SnO_4) nanocrystals synthesized by hydrothermal method, *Journal of Materials Science: Materials in Electronics*, **2018**, *110*(10), 109-120.

21. S. Yang and J. Zhang. Orange photoluminescence emission and multi-photon Raman scattering from microscale Zn_2SnO_4 tetrapods, *Chemical Physics Letters,* **2018**, *208*, 209-212.

22. S. Marković, A. Stanković, J. Dostanić, L. Veselinović, L. Mančić, S. D. Škapin, Dražič, I. Janković-Častvan, D. Uskoković. Simultaneous enhancement of natural sunlight- and artificial UV-driven photocatalytic activity of a mechanically activated ZnO/SnO_2 composite, *RSC Advances*, **2017**, *7*(68), 42725–42737.

23. C. H. Cheng, W. L. Hsu, C. J. Lin, Y. H. Pai, and G. R. Lin. Performance of highly transparent and stable zinc oxide co-doped thin-film by aluminum and ytterbium, *Journal of Display Technology,* **2014**, *10*(10), 786–792.

24. L.T.T. Vien, N. Tu, T. M. Trung, N. V. Du, D.H. Nguyen, D. X. Viet, N.V. Quang, D. Q. Trung, P. T. Huy. A new far-red emission from Zn_2SnO_4 powder synthesized by modified solid state reaction method, *Optical materials*, **2020**, *100*(109670), 1-9.

https://doi.org/10.52111/qnjs.2022.16501